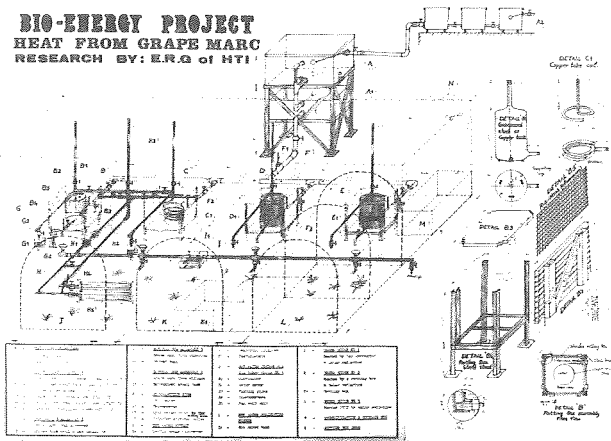




Review
 No. 10
 June 1981
 Nicosia

Editorial Committee:
A. Kaplanis Chief Editor
P. Vassiliou, Assistant chief Editor

BIO-ENERGY PROJECT
 HEAT FROM GRAPE MARC
 RESEARCH BY: E.R.G. of HTI

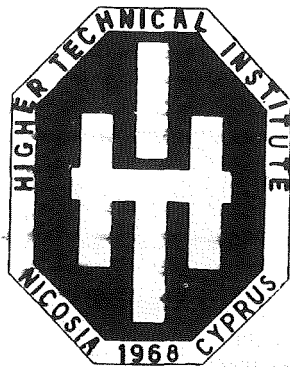


Cover drawing by Ch. Kalogirou

H.T.I. Review is published by the Public Information Office in cooperation with the Higher Technical Institute, Nicosia. It accepts articles which promote and further new developments and knowledge in technology, especially with reference to Industries of Cyprus. Requests for further copies of the magazine and for information concerning the published articles should be made to General Editor H.T.I. Review, Higher Technical Institute, P.O.Box 2423—Nicosia.

CONTENTS	
Page	
1	EDITORIAL
2	A GUIDE TO ENERGY SAVING By Constantinos Neocleous
4	CALIBRATION by C.K. Tavrou
5	BENTONITE AND ITS USES TO THE CIVIL ENGINEERING INDUSTRY By Dr. G. Constantinou and S. Kassinis
7	THE EFFECT ON THIN AND ELONGATED AGGREGATES ON THE STRENGTH OF CONCRETE By Miss Penelope Pai and Miss Ioanna Makri
9	PLASMA ARC MACHINING (PAM) By D. Roushas
11	LOW DEFINITION DIGITAL TELEVISION SYSTEM By Charalambos Theopemptou
14	STEEL FIBRE REINFORCED CONCRETE MATERIAL PROPERTIES AND STRUCTURAL BEHAVIOUR By Dr. H. Stavrides.
19	TOUGHNESS AND BRITTLE FAILURE OF METALS By G. Kadodrytes.
21	ELECTRONIC STRUCTURE AND POLARIZATION OF PHYSISORBED INERT ATOMS DUE TO THE SHORT RANGE INTERACTION WITH THE METAL SUBSTRATE By Dr. G. Oxinos
45	THREE-PHASE INDUCTION MACHINES UNDER CONDITION OF A SINGLE PHASE SUPPLY By G. Kladeftiras
49	DESIGN OF A VERTICAL AXIS AEROGENERATOR By M Pattichis
56	THE ORGANIZATION OF THE QUALITY CONTROL DEPARTMENT S. Vassiliou
61	ANALYSIS OF THE CYCLE OF THE SOLAR POWER STATION By Jerzy Kornad Nowakowski
63	H.T.I. CALENDAR OF EVENTS By Ms D. Charalambidou

The Higher Technical Institute (HTI) was established in 1968 as a Government of Cyprus project with assistance by the United Nations Special Fund (UNDP), the United Nations - Educational Scientific and Cultural Organisation (UNESCO), and the International Labour Office (ILO) Cyprus Government Executing Agency: The Ministry of Labour and Social Insurance.



Review

No. 10 June 1981 Nicosia

EDITORIAL

This is the tenth edition of the «H.T.I. Review», the annual publication of the Higher Technical Institute, which, as also mentioned in previous issues, serves as a means of promoting Technical and Scientific Publications for the Technical and Engineering Community of this country.

Most of the articles presented in this issue have been written by members of staff. Three Final year Students of the H.T.I. are also presenting articles based on their Diploma Projects.

In addition to the articles written by members of Staff and students of the H.T.I., we are glad to present the contributions of Professional Engineers and Scientists from other Government Departments, such as from the Director of the Geological Survey Department and Professional Engineers of the Ministry of Commerce and Industry, one of whom is an expatriate UNDP Adviser on heat pumps, Heating and Ventilation to the above Ministry.

The topics cover a variety of fields and we feel sure they will arouse the interest of the reader relevant to his field of specialisation.

We are pleased to have received articles on topics of current interest such as «Bentonite and its use to the Civil Engineering Industry», «Analysis of the cycle of the Solar Power Station», «Design of a Vertical Axis Aerogenerator», «A new Theory for studying the Electronic Structure of Physisorbed inert atoms on metals», «Steel Fibre Reinforced Concrete» and other topics of interest.

The editorial committee wishes to express its many thanks to all contributors for their worthwhile effort.

Editorial Committee.

A GUIDE TO ENERGY SAVING

by Constantinos Neocleous
Lecturer, H.T.I.

Energy saving is of utmost importance to all Cypriots, because of our country's heavy reliance on imported oil. Indeed in 1980 approximately 79 million Cyprus pounds were spent on oil imports which was roughly as much as the country's income from tourism for 1980.

Controlling the crude oil imports is of great importance because less Cypriot money will be channelled to the gulf. Furthermore, time will be gained until new exploitable, renewable and technoeconomically feasible sources of energy will be available.

In order to help control the wasteful use of energy, a list of practical measures is presented which can be useful to most if partly or fully followed. This compiled information has been obtained mostly from specialized publications of abroad.

1. THE HOUSE

1.1 When building a house:

- (a) Prefer a plan which is as square as possible. Since the heat loss or gain through a structure depends on the exposed surface area, a square plan will result in less energy losses than a rectangular.
- (b) Thermally insulate the external side walls and especially the roof.
- (c) Insulate all floors which are located above an unheated space.
- (d) Prefer double glazed windows than single glazed.
- (e) Wind-powered fans may be used on the roof, similar to those fitted on buses.
- (f) Paint the ceiling with a light colour.
- (g) Plant deciduous trees on the south of the house. They reduce summer solar heat gain and allow winter direct solar energy to heat

the house.

- (h) If you are planning to have a fireplace, install a damper to close it when the fireplace is not in use.
- (i) Never install equipment which are larger than necessary. (Boilers, radiators, air conditioners...)
- (j) Always buy the smaller suitable unit with the highest operating efficiency.

REMEMBER: *Effective insulation reduces the initial capital investment in machinery for heating and cooling and reduces their operating cost.*

1.2 For an existing house:

A. Insulation

- (a) Consider the use of insulation. Proper insulation can reduce the heating or cooling load by as much as 25%.
- (b) Use carpets as an aid to thermal insulation.
- (c) The heat loss from windows is 2 to 3 times more than that from an equal area of wall. Therefore the use of curtains at night is beneficial.
- (d) Check the gaps on the doors and windows, through which air can leak in or out. The gap must be as small as possible. By moving a lighted candle around the frame of a window and observing where the flame dances, the leaks can be spotted. Similarly by slipping a coin under a door and observing whether it goes through freely, is an indication on whether weatherstripping is required. In Cyprus many types of weatherstripping materials are available.

B. When central heating is available:

- (a) Close all unoccupied rooms.

- (b) Use the kitchen and bathroom ventilators only when necessary.
- (c) When the fireplace is not lighted, close the damper. Consider the possibility of using a glass framed cover to isolate its entrance.
- (d) Insulate all pipes and ducts which pass through unheated spaces.
- (e) If the central heating is on, while the fireplace is operating, it is very likely that heat is wasted unless all doors and ducts leading to the fireplace, are left slightly open.
- (f) Make sure that all windows adjacent to the thermostat are lightly closed.
- (g) Regularly clean the heat emitting units (radiators) from dust.
- (h) At night close all curtains.
- (i) Inspect and maintain the boiler at least once a year, as per the instructions of the supplier.

C. When air conditioning is available:

- (a) Insulate the air ducts.
- (b) Set the thermostat at 25°C
- (c) When initially starting the air-conditioner do not set the thermostat at a lower temperature than that required in the space.
- (d) Clean the filters regularly.
- (e) Never put lamps or TVs near the thermostat.

2. Domestic hot water boilers:

- (a) Make sure that the hot water storage tank is well insulated.
- (b) Use cold water for house cleaning, if possible.

- (c) Repair all leaking faucets.

3. Kitchen

- (a) Always boil water in a closed pan.
- (b) Always try to match the size of the pan to the size of the heating element.
- (c) If you are cooking with electricity, turn off the electric elements some minutes before the required time for cooking elapses.
- (d) Making toast in the oven is very expensive.
- (e) Use pressure cookers.
- (f) Never cook foodstuff right after you take them out of the freezer.

4. Refrigerator.

- (a) Never keep the door unnecessarily open.
- (b) Maintain a temperature of 3 to 4°C in the fresh food compartment and -15°C in the freezer.
- (c) Refrigerators that do not have automatic defrost are cheaper to operate than those that have.
- (d) Make sure the refrigerator door is airtight.
- (e) Never put hot food in the refrigerator. Let it cool in the air first.

5. Washing machine.

- (a) Always use the washing machine when it is fully loaded.
- (b) If weather and time permits, dry

the clothes outside in the fresh air.

6. Lighting

- (a) Put off all lighting in unoccupied rooms.
- (b) Prefer one large lamp than many small of the same total light intensity.
- (c) Use fluorescent lamps whenever possible. They are more economical than incandescent lamps.

7. Car

7.1 When you buy a car:

- (a) Conduct an exhaustive market research to compare the efficiency and specific fuel consumption of similar cars within the range of capacity you are interested.
- (b) When comparing two similar cars, the one that has lower weight, manual gearbox and smaller frontal area is likely to be the more efficient.

7.2 When you drive a car:

- (a) Share rides with others.
- (b) Some errands can be accomplished with a telephone call.
- (c) Drive smoothly.

Remember to drive in such a manner that the use of brakes is minimized.

A 1500cc car with four passengers wastes so much energy as it is needed to boil approximately two glasses of water.

- (d) Try to predict any changes in speed so that you can act accordingly in advance.
- (e) Do not overfill the fuel tank.
- (f) Plan the route of your trip in advance.
- (g) Do not overload the engine.
- (h) Do not hold the car by using simultaneously the clutch and the fuel pedal.
- (i) Eliminate any excess unnecessary weight from your car.

7.3 Car maintenance:

- (a) Check and adjust your car accordingly.
- (b) Maintain the air filter clean.
- (c) Check the air pressure in the tyres. There is an increase in fuel consumption of up to 2% for every psi below the one recommended by the car manufacturer.
- (d) Radial-ply tyres are more economical than cross-ply tyres.
- (e) Make sure the wheels and steering are well balanced.

8. In industry

- (a) Check that all machinery is functioning efficiently.
- (b) Check for steam and compressed air leaks, and remedy accordingly.
- (c) Make sure the air compressor does not operate at higher pressure than that which is actually required.

CALIBRATION

by C.K. Tavrou
Lecturer, H.T.I

Measuring instruments and measurement standards deteriorate in accuracy during use, and, to a lesser degree, during storage. To maintain accuracy requires a continuing system of calibration control. Taking as an example a pressure gauge or a voltmeter, when it is first bought it is naturally considered that it will give the correct readings when used. This is true only with the assumption that before the instrument was released by the manufacturers, it was tested. It is also fair to state that the instrument will not attain its accuracy throughout its operating life, mainly due to wear. On the other hand, the operating life of such an instrument is much longer than the time before starting to lose its accuracy. In order to trust the measurements of an instrument it is necessary to test its accuracy at certain intervals. This testing is what is called calibration of the instrument. The frequency of calibration depends on the nature of the instrument, its accuracy and expected reliability and is given by the manufacturer.

The question is what should be used as a basis to calibrate another instrument and how is it possible to be certain that the device to be used is accurate itself? Before proceeding to answer, it has to be said that the higher the accuracy of a device, the higher is the cost of construction and maintenance.

To enable the person on the shop floor calibrate his instruments often enough, without having to get into great expences, a system has been devised on an international basis where instruments of higher accuracy are taken as reference to calibrate other instruments with lower accuracy. For example, in length measurements, the standard unit is the metre and is defined by the International Standards Organization (ISO) as equal to $1,650,763.73$ wavelengths, in vacuum, of radiation corresponding to the transition between the levels $2P_{10}$ and $5d_5$ of the Krypton 86 atom at certain specified conditions. The definition clearly indicates the complexity of the instruments used to calibrate other instruments of lower accuracy. However, this is the International Pro-

TOTYPE Standard and it is absolute, in the sense that there are no other standards with which it can be compared. Following are the National Standards which are copies of and are calibrated with reference to the International Prototype standard. Then are the Reference Standards which are constructed by a different method to the primary and National Standards, so that they are cheaper, more easily used and less likely to be damaged by frequent use. These are calibrated according to the National Standards. Next in the hierarchy are the main laboratory's Working or Calibration Standards, used in calibration of standards in industry. These are in turn calibrated against the Reference Standards. Lastly there are the Industrial and Commercial Standards which are used to calibrate shop instruments in daily use, i.e. micrometers, vernier calipers, electrical multimeters. etc.

By this «ladder of accuracy» the equipment for calibrating shop floor instruments is cheap enough, durable enough and not so complicated, therefore, quick and inexpensive calibration of instruments is possible. The fact that there are so many expensive instruments and equipment before arriving down to the industrial standards, does not mean that the costs incorporated are very high. In fact, by using this system, a small number of higher and only one of highest accuracy standard is necessary to maintain accuracy at the required level and at reasonable costs.

Now that the above has been discussed, comes another question, to what extent are these facilities utilised?

In all the industrialised countries, the calibration of instruments is a must, either for safety reasons or production purposes. For example, in a factory where gas cylinders for domestic use are manufactured, they have to be tested on the pressure they can withstand when filled. Both in the final testing stage and later during filling the gas cylinder, the pressure gauges used must be giving the true values of pressure, otherwise human lives may be in

danger. For the case of production purposes, a good example is the manufacture of cars. The parts of a car are not all produced in the same area or necessarily at the same factory. All the parts though, will have to be assembled together at the final stage. If all the different manufacturers were not using instruments that measured and indicated the correct dimensions, it would have not been possible to assemble all the parts together.

In the non-industrialised countries, calibration is mostly done where safety is concerned only. In the manufacturing sector, the inconvenience and cost due to non-calibrated instruments, is not high enough to make the people concerned realise its value. In small machine shops it is just as important to use calibrated instruments as they too produce components for assembly work.

Cyprus comes under the non-industrialised countries. Until recently there were only very few and inadequate calibration facilities. Now, though, with the efforts of the government, there are more calibration facilities covering a wide field of the local industry. In particular, there are calibration facilities at the Higher Technical Institute, covering a large number of Mechanical and Electrical instruments. However, the availability of calibration equipment at some place, does not automatically mean that the products are made accurate and in compliance to the design specifications. The manufacturers have to firstly realise the necessity of calibration and utilise the facilities for their own instruments. Only then, would there be products which will comply with the design specifications.

In concluding this short introduction to Calibration, I believe that the manufacturers have to realise that in today's world, with today's technological progress, it is not enough to hope, think, or just believe that an instrument reads correctly, but it must be made certain that an instrument measures and indicates the correct value within acceptable limits.

BENTONITE AND ITS USES TO THE CIVIL ENGINEERING INDUSTRY

by Dr. G. Constantinou *Director Geological Survey Department* and S. Kassinis *Chemical Engineer Ministry of Commerce and Industry*

Bentonite is an earth material composed essentially of a smectite clay mineral (montmorillonite group) and whose physical properties depend on the smectite components (1).

Bentonites arise from volcanic rocks like basalt, diabase and volcanic ash. These materials were converted to bentonite under alkaline conditions and the level of conversion influences the properties of bentonite as well as the content and the kind of contaminant substances.

Although clays have been used from thousands of years, understanding of the molecular and atomic structure along with apparatus and instruments for measuring and observing the many clay minerals have only recently been made available and are continually being improved. As a result to that bentonite usage has changed considerably over the ages. The unusual properties of the mineral have been known for many centuries. Early references to Fullers earth (calcium bentonite) from the Greek play «The Frogs» published about 405 B.C. and in the old and New Testaments of the Bible. In these references the clay was mixed into a mud with water and was used to remove grease from natural wool and for cleaning soiled cloth, processes which later came to be known as «fulling».

The fulling process developed in the U.K. (initially spread by the Roman Empire through France to England) reached its peak during the middle ages. By the end of the 19th Century this use of the clay started to decline and others emerged.

First the absorption properties were used in carpet cleaning and for cleaning felt hats. Then the beaching of vegetable oil and paraffin was developed in the U.S.A. During the first world war the Germans progressed an acid «activated» bentonite for refining inedible fats to make them consumable.

Nowadays bentonite is produced and sold under strict specifications which includes standard procedures and equipment for quality control (II,III,IV). The main industrial uses of the swelling bentonites are as a drilling mud (26%) foundry sand band (23%) iron ore pelletization (21%) and for Civil Engineering purposes (V). In addition there are numerous other small uses which include pharmaceutical preparations, wine clarification, water purification, additives for cattle feed stuff and industrial floor cleaning agents, in ceramic and fertilizers, cosmetics and soaps etc. An important range of absorbents is produced by manufacturing the clays into granular form - among other uses granules are used as pet litter for which there is a growing market.

The bentonite uses are to be continuously spread and increase in the future due to the considerable research work which is in progress in many countries nowadays. E.g. the fulling. Recent studies (VI) in USA has shown the

bentonite to be an excellent conductive backfill in ground rod installations in problem soils, assuring effective means of obtaining and maintaining a low resistance to remote ground in electric substations.

Lowering each rod's resistance to remote ground when bentonite was used as Backfilling medium was found to be up to 36%.

Bentonite clays in general and particularly in Cyprus, keep large areas infertile; most landslides and many foundation problems for roads and other engineering structures are caused by them and this is very well known by all Civil and Construction Engineers. On the other hand bentonite has particular properties that can be exploited for a number of uses in the construction industry. Very particular is its behaviour with water depending on the type and its structure. The main uses of bentonite in the construction industry are outlined below.

Introduction

Although thixotropic slurries such as bentonite have been used for lining boreholes by the oil industry since 1929 the use of these slurries in constructional engineering only started in 1950.

Bentonite is used in foundation engineering for diaphragm wall construction, piling grouting and lubrication. It is also used in tunnelling operations.

Slurries containing between 4% and 8% of bentonite are used for grouting (that is making strata such as Sand and gravel impermeable, for example in the foundations for tunnels and dams) for diaphragm wall construction (providing non-mechanical well support for trenches, during piling and in other excavations) and as a lubricant in sinking caissons, bored piles and similar foundations.

In the U.K. about 0.05% bentonite is added to some grouting mixtures to act as a Lubricant. The addition of bentonite to the grout has three main purposes. It acts as a plasticizer and a lubricant which enables the grout to be pumped further, the addition of a small amount of bentonite can increase the volume of the grout considerably and it is a waterproofing agent.

One of the major new uses for bentonite in civil engineering is in plastic concrete. Bentonite is mixed with the cement or concrete and the resulting concrete has the consistency of a hard clay. The concrete is impermeable but is capable of moving with the ground. Ordinary concrete is more likely to crack under these conditions. Plastic concrete is used to built impermeable walls around reservoirs. It can also be used around chemical works to prevent toxic chemicals from spreading into the surrounding countryside.

Cement - Bentonite Grouts

Addition of bentonite to water-cement slurries greatly extends the range over which suspensions free from segregation by settlement may be obtained. The dry bentonite and cement powders may be mixed together and subsequently added to water, or a pre-gel of bentonite may be made and added to the cement slurry.

Conversion of the bentonite to its calcium-exchanged form undoubtedly occurs, through reaction which free line derived from the cement. The calcium bentonite is then flocculated by the excess of cations (mainly calcium) present in solution in the continuous phase. The flocs so formed are still gelatinous and prevent sedimentation of the relatively coarse cement particles. The primary role of the bentonite thus appears to be that of a suspending agent.

In general, limitations on the quantity of bentonite which can be incorporated in a mix are imposed by the following factors:-

1) Workability of the mix:

Increasing the concentration of bentonite leads to an increasing stiffness in the slurry eventually making it un-pumpable;

2) Final compressive strength:

Substantial additions of bentonite to cement slurry decreases the compressive strength of the cement;

3) Grout specific gravity:

Low specific gravity grouts showing a reduced tendency to migrate through the soil after placement are obtained by increasing the bentonite concentration in the mix;

4) Stability towards sedimentation:

The concentration of bentonite in the mix must be increased as its cement content is lowered if slurries resistant to settlement are to be obtained.

The composition of a mix for a given function can only be decided by taking these factors into account.

Considerable economies in cement consumption per unit volume of grout can be made, particularly when final strength is of secondary importance.

Soil Impermeation and Consolidation

The ability of bentonite suspensions to flow into soil pores, setting thixotropically to gels, may be turned to good account in soil impermeation. The low permeability of even weak gels, and the tenacity with which they are held in soil pores, renders them particularly attractive.

A wet classified sand 0.43mm average grain diameter, permeability 2.0×10^{-1} cm/sec., was injected with a fully hydrated 6% suspension bentonite. The permeability was re-determined 15h after injection, and was found to have dropped to 5.8×10^{-5} cm/sec. when measured as a pressure differential lower than that required to displace the gel from the pores in the sand.

The reversible thixotropy of the suspension allows

marked disturbance to the soil without changing the permeability. The known sensitivity of bentonite suspension to flocculation by polyvalent cations, which are often present in groundwater, suggests that there may be circumstances where the extent of impermeation may decrease with time. Precise information on this topic, and on the question of low tar loss of permeability can be offset by the use of peptizing agents, is lacking.

The chemical reactivity and cheapness of bentonite makes it worthy of continued consideration as a consolidating agent.

Stiff permanent gels which undergo little or no shrinkage in contact with groundwater can readily be formed by reaction with silicates.

A method has been developed using bentonite slurry which makes possible tunnelling through soft strata such as sand and gravel. A bentonite slurry is pumped into the tunnelface, which it stabilises by gelling, enabling the cutters to excavate the gravel and the bentonite gel. The bentonite is then separated and recirculated for future use. This method of tunnelling has only been tried since 1972/73.

Bentonite for reclamation purposes is showing major improvement in its use to seal ponds, reservoirs, industrial and sewage lagoons, and in granting permeable grounds. It is not unusual to see specifications for power plant waste water ponds that call for tens of thousands of tons for a single project. These other uses although considered minor in the past could easily exceed 800,000 St. by the year 2000 (VII).

Conclusion

Although little vegetation occurs in bentonitic lands and the agricultural value of these areas is rather low by applying a proper treatment to the raw material of Bentonite, a very valuable product can be produced with numerous Industrial Applications in modern Industry.

References

- I) R.E. GRIM, N. GUVEN, Bentonites, geology, mineralogy properties and uses, Elsevier Scientific Publishing Co. Amsterdam 1978.
- II) API Specifications for Oil-Well Drilling-Fluid Materials, 1974.
- III) OIL COMPANIES MATERIALS ASSOCIATION Spec. No. OFCP.4 Rev. Oct. 1973.
- IV) Steel Founders Society of America SFSA 13T-65 Ed. 1965.
- V) MINERAL COMMODITY SUMMARIES 1980 -U.S. DEPT. OF THE INTERIOR-BUREAU OF MINES
- VI) IEEE Transactions on Power Apparatus and Systems. Vol. PAS 99 No. 4 July/August 1982.
- VII) BENTONITE - UPDATE: PRODUCTION, RESERVES, QUALITY CONTROL AND TESTING/1978 AIME Annual Meeting Denver, Colorado.

THE EFFECT ON THIN AND ELONGATED AGGREGATES ON THE STRENGTH OF CONCRETE

Miss Penelope Pai & Miss Ioanna Makri
3rd year students Civil Engineering Department

An experimental study of the effect of thin and elongated aggregates on the strength of concrete was made, in part satisfaction of the final year diploma project.

The object and scope of the project was:

1. To determine the percentage of the thin and elongated pieces in the local aggregates.
2. To carry out all possible tests in the labs in order to determine the strength and the particle size distribution of local aggregates by sieving.
3. Keeping all other parameters constant and conforming to the British Standards, to design various concrete mixes with % of thin and elongated pieces in aggregates as the only variable.
4. To determine the strength of the concrete at 0%, 10%, 20%, 25%, 30%, 35%, 40%, 50% content of thin and elongated pieces in the aggregates.

The experimental work performed covered,

- (A) Testing of Aggregates (Coarse)
- (B) Testing of concrete.

A TESTING OF AGGREGATES (COARSE)

1. Particle size distribution was determined by sieving. Aggregate particles were found to lie within zones 1 and 2. (Zone 1: 1 1/2" - 3/16").
2. Shape tests were made on aggregates to determine the flakiness and Elongation Indices and also the percentage of thin and elongated pieces in the aggregates.

a. Flakiness index is the percentage of the weight of the flaky particles (particles of a thickness less than 0.6 of their nominal size) to the total weight of the sample. For the sample tested it was found to be 19.75%.

b. Elongation index is the percentage of the weight of the elongated particles (particles of length - greatest dimension - of more than 1.8 of their nominal size) to the total weight of the sample. For the sample tested it was found to be 25.85%.

c. Thin and elongated pieces are the particles which are either flaky or elongated. The percentage of these in the local aggregates used was found to be 40.89%.

3. The impact value of the aggregates was determined by the impact test and found to be equal to 14.54%. This gives a relative measure of the resistance of the aggregates to sudden shock or impact.

4. The crushing value of the aggregates was determined by the crushing test and found to be equal to 17.58%. This gives a relative measure of the resistance of the aggregates to crushing under a gradually applied compressive load.

5. The bulk density of the aggregates was found to be equal to 1355.6 Kg/m³.

6. The specific gravity of the aggregates was found to be equal to 2.69.

7. The water absorption by the aggregates is 1.92%.

B. Testing of concrete:

Keeping all other parameters constant and conforming to the British Standards various concrete mixes were designed with percentage of thin and elongated pieces in

aggregates as the only variable.

It should be noted that the separation of the aggregates into thin and elongated aggregates and clear aggregates was achieved by passing each piece through the B.S. gauges.

The proportion selected was 1:2:4 with water-cement ratio equal to 0.8.

Three cubes were made for each concrete mix. All cubes were compacted for the same time on the vibrating table.

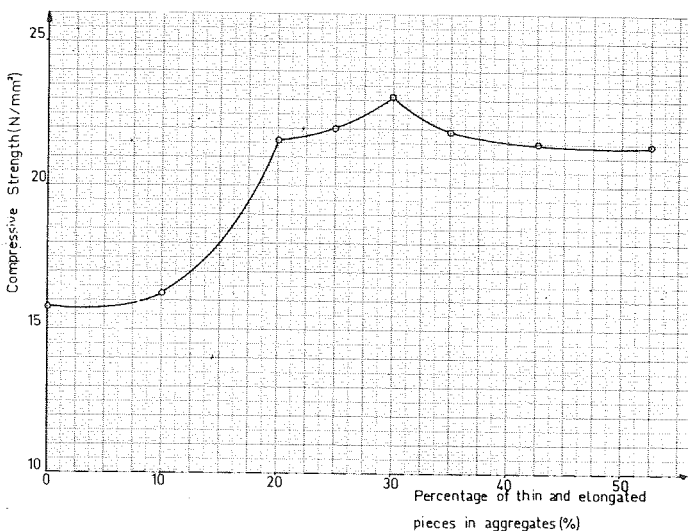
Cubes were cured in water for 28 days.

For each concrete mix the mean compressive strength was taken.

To determine the workability of each mix the slump test was made.

Results:

% of thin and elongated pieces in local aggregates	Compressive Strength (N/mm ²)	Slump (cm)
0	15.77	1.0
10	16.25	1.5
20	21.61	2.0
25	22.04	2.5
30	23.09	2.5
35	21.89	1.5
40	21.47	1.5
50	21.47	1.5



Conclusions:

A. Sieve analysis test gave a *well-graded* particle size distribution. Thus the various sizes of particles interlock together leaving the minimum volume of voids. It is workable, thus reducing labour in placing.

Zones 1 and 2 are the coarsest gradings. Thus the aggregates tested are comparatively workable and strong. They also absorb more water.

Flakiness and Elongation Indices were found to be 19.75% and 25.85% respectively which are acceptable by the B.S (the maximum value as 30%).

The percentage of thin and elongated particles in the aggregates was found to be equal to 40.89% which according to the results gives strength of about 23.09% N/mm².

The impact and crashing values of the aggregates were found equal to 14.54% and 17.58% respectively, which is according to the B.S (maximum value of 30% for both).

The silt and clay content in the aggregates is acceptable since it is lower than 1 percent by weight which is specified by B.S 882:1965.

Conclusions (Cont.):

B. The concrete mix used for making the cubes was 1:2:4. The water/cement ratio was 0.8. This seems to be high but can be justified by the following:

1. Crushed coarse aggregates were used with sharp edges and rough surfaces, needing a higher water/cement ratio for an acceptable degree of workability.

2. All materials were dry and as a result they were absorbing enough water for saturation. This absorbed water is not included in the net or effective mixing water.

3. Thin and elongated aggregates, lower the workability due to their sphericity. Thus a higher water/cement ratio is needed to obtain a workable concrete.

The slump values were found to lie between 1.0-2.5cm. According to theory such a concrete is good for heavy mass construction.

Observing the curve which relates the compressive strength of the concrete cubes with the percentage of thin and elongated particles a maximum compressive strength of 23.09N/mm² is obtained for a percentage of 30%.

Beyond the 30% region the compressive strength is gradually decreasing.

The rate of increase of the compressive strength between 0% and 30% is rather high. B.S. limit the permissible elongation and Flakiness index to 30%. (it should be noted that both flaky and elongated particles have the same effect on concrete).

The reduction of compressive strength was expected since thin and elongated aggregates are of reduced strength and also tend to be oriented in one plane with water and air-voids forming underneath.

The rate of decrease was rather low, because high bond stress exerted between thin and elongated particles and the concrete matrix results in high compressive strength.

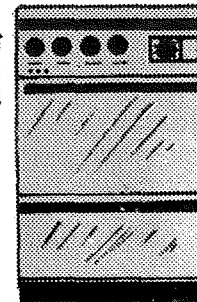
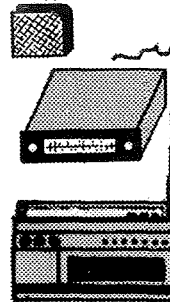
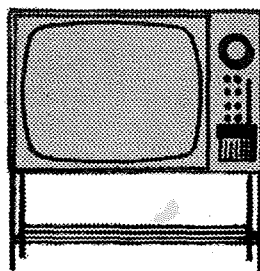
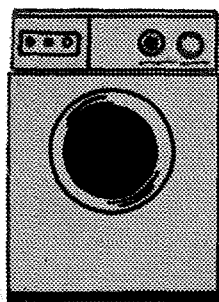
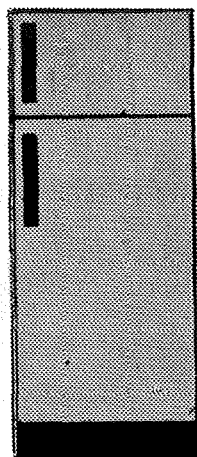


ΘΑ ΑΓΟΡΑΣΕΤΕ Ή ΘΑ ΔΙΟΡΘΩΣΕΤΕ
ψυγείο, πλυντήριο, τηλεόραση, κουζίνα, ραδιομαγνητόφωνο κλπ;

ελάτε σέ μας
ΠΟΛΥΣ ΜΑΛΛΟΥΠΑΣ ΚΩΣΤΑΣ-ΠΑΠΑΚΩΣΤΑΣ

ΛΕΩΦ. ΣΤΑΣΙΝΟΥ 29 · ΤΗΛ. 47344 · ΛΕΥΚΩΣΙΑ

για κάθε σας πρόβλημα
τηλεφωνήστε μας στο 47344
θα σας εξυπηρετήσουμε αμέσως
μέ τις πιο χαμηλές τιμές!



PLASMA ARC MACHINING (PAM)

by D. Roushas, Workshop Superintendent H.T.I.

Principle of the process

The PAM process utilises an ionised plasma for energy transfer. A plasma is defined as a gas which has been heated to a sufficiently high temperature to become partially or completely ionised. Constricting an electric arc in a plasma device has the effect of increasing the temperature of the ionised gas and at the same time concentrating the heat into a narrow, near-parallel gas stream moving at a very high velocity, which when impinged on a workpiece removes the material by melting and blowing away the molten material.

Arc plasma devices can be divided into two main categories. The first one where the arc is struck from the rear electrode of the torch to the workpiece (transferred arc) generally termed as 'plasma arc' and the second where the arc is operated within the torch itself and only ionised gas is emitted (non-transferred arc) generally termed as 'plasma jet'. The heat transfer rates attainable with plasma equipment are over 10 times that obtainable with an oxy-propane rocket flame.

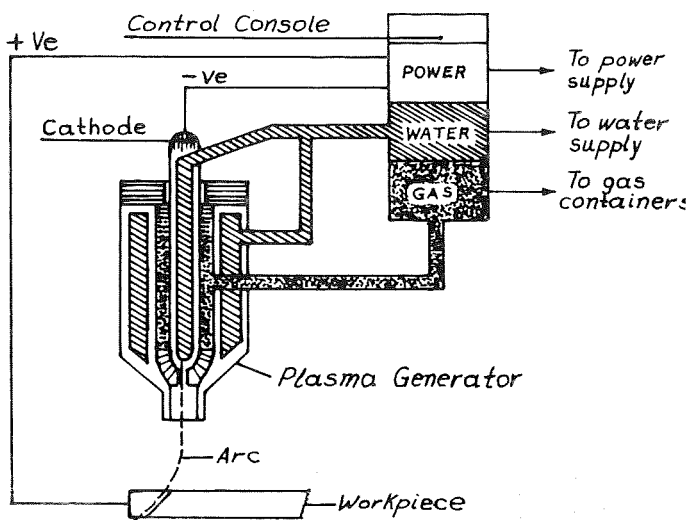
Variables associated with PAM operation can be divided into three categories:

- Those associated with the operation of the torch
- Those associated with the physical configuration of the set-up and
- Those associated with the environment in which the work is performed.

Equipment for PAM

Electrical power supply, plasma torch, supply of gas and cooling water, plasma generator, work handling devices and servomechanism for control and machine tool capable of withstanding high temperatures.

A typical layout of Plasma-Arc Machining process is shown below.



Layout of Typical Plasma-Arc Machining Equipment

Operating parameters

Power : 20 to 200 KW

Voltage : 50 to 200 V

Current : 200 to 2000 A

Plasma gas:

Argon and hydrogen (100-40 mixture)

Nitrogen and hydrogen (80-20 mixture)

Plasma intensity:

Maximum heat transfer rate 6.87 kJ/cm²/s (non-transferred arc)

24.53 kJ/cm²/s (transferred arc)

Maximum temperature: 16,650°C for non-transferred arc
33,300°C for transferred arc.

Workpiece material: Must be electrically conductive for transferred arc.

Non conductive materials can be machined for non-transferred arc.

Machining performance of PAM

(a) General characteristics

Performance of PAM depends on power, gas flow and characteristics of workpiece. Plasma cutting is quicker than oxy-fuel gas method.

Depth of heat affected zone depends on work material, thickness and cutting speed.

In cutting, the cuts are usually free from dross but they are not quite perpendicular to the face of the plate.

Torch stand-off distance is usually 0.5 to 1.5 cm from the workpiece. No physical contact between torch and workpiece and as such no tool wear and tool breakage problems.

Rapid chilling of the heat affected zone will lead to formation of fine cracks.

Additional safety provisions to protect radiant heat of the cutting zone, adequate ventilation are required.

(b) Material removal rate

(i) Estimated

The metal removal rate has been estimated based on an empirical formula. Specific power required to remove mild steel by PAM is given by

$$\frac{1}{15} \frac{\text{KWh}}{\text{in}^3} = 4,000 \text{ watts/in}^3/\text{min}$$

With a 10 KW power input to the process,

$$\text{Material removal rate} = \frac{10,000}{4,000} = 2.5 \text{ in}^3/\text{min} (40.97 \text{ cm}^3/\text{min})$$

In practice, normally plasma equipment for machining applications will have capacities higher than 10 KW. The material removal rates claimed in practice are slightly higher than the predicted values. For an optimised plasma operation, in practice up to 45 percent of the electrical power delivered to the torch is used to remove the metal from the workpiece. Of the remaining power, approximately 10 percent goes into the cooling water in the plasma generator and the rest is wasted in the hot gas and in heating up the workpiece. The maximum metal removal rate of 114.7 cm³/min has been reported with a 50 KW total power input. Assuming 45 percent of the power is used in metal removal, the material removal rate from the formula will be 92.2 cm³/min, which is lower than the actual value claimed.

However, in PAM the torch angle of plasma, the workpiece surface condition obtained and the gas flow rate are also important. The formula can be used for predicting the metal removal rates for initial estimation purposes.

(ii) Practical

The material removal rate is up to 10,000 cm³/hr. When operating at 50 KW power level, maximum practical depth of cut is 6mm to 9mm.

(c) Surface finish

The process leaves a very rough surface. Depth of heat affected layer - up to 3mm in turning small diameter workpieces, and up to 5mm in cutting stocks.

Advantages of the process

Principal advantages of PAM are that it is equally effective on any material regardless of hardness or refractory nature. It provides mechanical decoupling of the tool and the workpiece so that only simple support

structures are required. The process provides high metal removal rates up to 10,000 cm³/hr and the removal rates for high strength materials are comparable to that of conventional turning. It is possible to cut both ferrous and non-ferrous materials in thicknesses ranging from 0.6 cm to 15 cm. By holding the torch stationary over a metal plate it is possible to produce round holes, the diameters of which are limited by the size of nozzle orifice. The depth to which the holes can be drilled and the accuracy and repeatability achievable are limited.

Limitations of the process


With PAM, it is not possible to control the corner radii precisely and the surface finish obtained is very rough. Subsequent secondary operations will be required to obtain a desired surface finish and to remove the heat affected layers. Applications of the process are mainly restricted to cutting and rough turning of hard materials. The possible toxic effect of the fumes produced by the plasma, high voltages associated and the radiant heat of the cutting zone requires special safety provisions.

Typical applications of PAM

Cutting of stainless steel and refractory metals. Rough turning of bar stock of nickel alloys and «difficult to machine» materials. Pulley grooving and hole piercing. Cutting of metals resistant to oxy-fuel gas cutting such as magnesium, titanium and copper. Cutting light materials, such as textiles, where a sealed edge is produced.

References:

1. «Survey of ultrasonic, plasma and electron beam machining». Report No. 121, PERA, U.K. 1963
2. «Tool and Manufacturing Engineers Handbook». D.B. Dallas, Society of Manufacturing Engineers, Michigan U.S.A., 1976.



ΜΠΟΓΙΑΔΕΣ ΑΓΓΛΙΚΗΣ ΠΡΟΕΛΕΥΣΕΩΣ

☆☆ Άσυναγώνιστες σε τιμή ☆☆
☆☆ Άσούγκριτες σε ποιότητα ☆☆

- Μπογιάδες για κάθε χρήση, για κάθε σπίτι.
- Μπογιάδες που διαρκούν και διαρκούν.
- Πλούσια συλλογή χρωμάτων που ικανοποιά και τὸ ποιὸ δύσκολο γούστο.

Ἔσείς που ζητᾶτε τὸ καλύτερο ἐλάτε σ' ἐμᾶς

ΕΙΣΑΓΩΓΕΙΣ/ΔΙΑΝΟΜΕΙΣ

ΝΕΟ. ΙΑΚΩΒΟΥ

Κανάρη 11, Ἄγ. Ὁμολογηταί
Τηλ. 41664
Λ Ε Υ Κ Ω Σ Ι Α

LOW DEFINITION DIGITAL TELEVISION SYSTEM

Charalampos Theopemptou
Lecturer HTI

With a video recorder one can record a film of several hours, but what happens if you just want to record a single picture! with modern day technology one can of course get a freeze facility on the video recorders but at a price.

Described below is a system that gives this facility at a low price but at the expense of picture quality. Two controls are provided. The freeze control freezes the picture on the screen so that the operator can easily choose which picture to store. The store control can store the picture displayed frozen on the screen, on audio magnetic tape.

For ease of description the input signal is taken from a video Camera, but the system can also be adapted for broadcast transmission. The set up is shown below in Fig.1

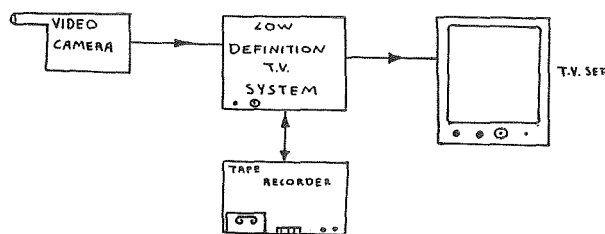


Fig. 1 System peripherals

Brief summary of operation:

The input signal to the system is the composite Video signal (i.e. the Video camera output). From this signal the synchronizing pulses are extracted and processed so that, a particular sequence and number of lines are chosen. The video content of these lines is converted into digital form and stored in digital memory I.C.'s.

By controlling the Read/Write sequence and continually changing the memory contents according to the input composite Video signal, a smoothly running low definition display is achieved. This has the same picture frequency as before i.e. 25 pictures per second although fewer lines are used.

With the use of a switch the memory contents are prevented from changing, with the result of a 'frozen' picture appearing on the T. V. screen. If that picture is selected for recording then the memory contents are read slowly, converted into serial form and recorded on Audio magnetic tape.

The television signal

The British Standard Television waveform is based on 625 lines and 50 Hz field frequency. That is, to constitute a complete picture a time «space» of 625 lines is needed, which are divided into 2 fields referred to as the Even and Odd fields.

The path followed by the electron beam at the receiver is shown in Fig. 2.

As it can be seen, the beam moves from left to right and on reaching the right hand side, it quickly returns to the left again, but instead of scanning out the immediate line underneath the one just traced, it moves to the next one.

A complete scanning of every other line of the picture, from top to bottom, is called a «field». On reaching the bottom of the screen, the beam moves back on top and scans out the lines left out in the previous field. This process is called «Interlaced scanning». The field that contains the first visible line is called the «Even» field. And the other one is called the «Odd» field. The two fields together constitute a picture. Now because each field appears 50 times a second, a complete picture is scanned with a frequency of 25 Hz (i.e. $1/50 + 1/50 = 1/25$ second or 25 Hz).

The employment of the Interlaced scanning principle, achieves a picture frequency of 25 Hz, which is sufficiently high for the Human eye to «average» the pictures and perceive them as a smooth sequence, without flicker.

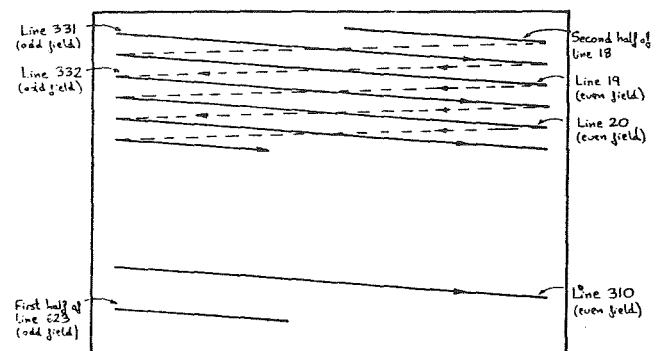


Fig. 2. Interlaced. Scanning Pattern (Raster)

It should be noted here, that although there is enough «space» time available for 625 lines, only 585 lines are visible. A «space» of 20 lines is taken up by each field, for synchronising purposes.

The complete video signal contains the following information:

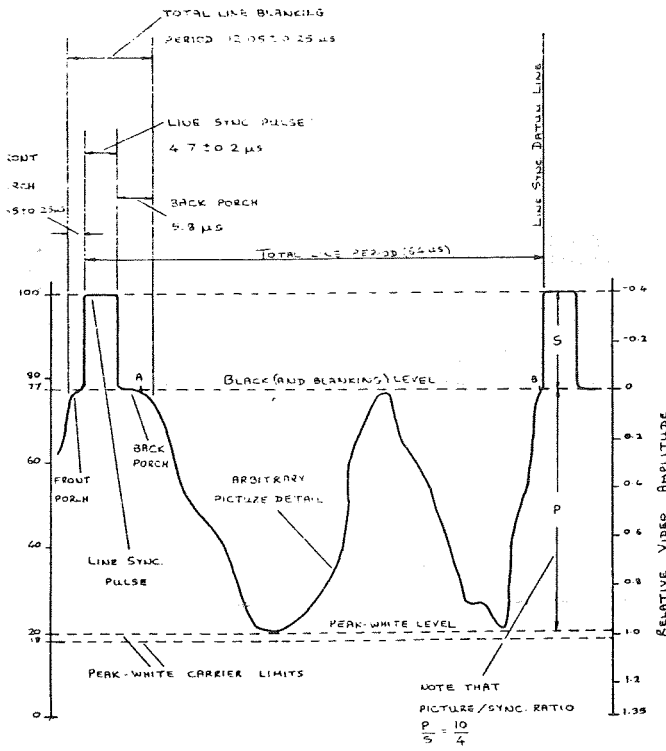
(a) Active line

As the beam moves from left to right, its intensity (i.e. brightness) is varied according to the picture content at that point on the screen. This brightness variation, is represented in the video signal by voltage variations. See Fig. 3.

(b) Synchronising Pulses (sync. pulses)

These are needed so as to maintain synchronisation, between the transmitter and the receiver. The sync. pulses therefore, contain information as to the exact point at which the beam should be at any instant to maintain intelligibility of the picture (See Fig. 4.).

These pulses therefore provide instructions to the receiver as to when to change lines, fields, etc.



N.B. (i) Sampling Starts at point A and stops just before point B.

(ii) Time between A and B corresponds to the duration of Logic '1' of the «Line Clock».

Fig. 3 One Video Line

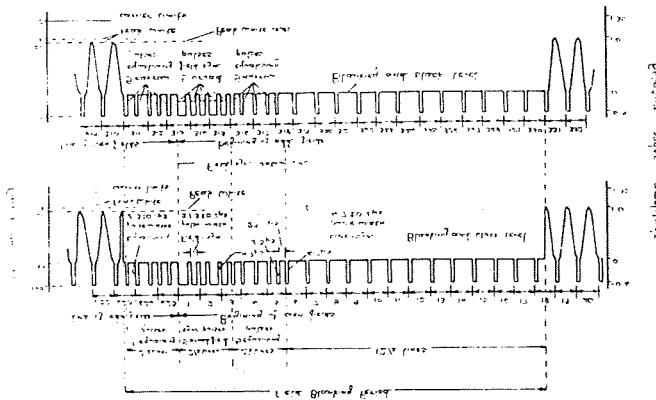


Fig. 4 Field Synchronising Waveforms of the British 625-Line Television Signal.

Low definition digital television standards

Because the main objective of the system is to store a complete picture at low cost, (approx. St£70) a set of Standards was needed from the beginning, on which the actual circuit design could be based.

Attempts to store T.V. pictures in high definition form, would be unjustifiably expensive for our purpose.

Resolution bits

For entertainment purposes in analogue T.V. systems an infinite number of variations of grey (i.e. brightness levels between black and white) is employed.

But as the signal is to be stored in digital form, an analogue to digital converter has to be used and that in turn implies that a definite number of grey levels had to be decided beforehand.

The number of grey levels is determined by the number of bits that the A/D converter is operating at. An n-bit output A/D converter, is said to give n-bit resolution and the number of grey levels is equal to 2^n .

The number of 16 grey levels was decided upon, this being a reasonable number for our purposes and requiring the use of a 4-bit A/D converter.

It should also be noted here that for a given number of samples taken, the fewer the number of resolution bits, the less storage capacity is needed.

An additional advantage of operating with 4-bits resolution, is that 4 is a binary number and all the available I.C. memory chips are arranged in stacks of either 1,4,8 ... bits making addressing a little easier and cheaper.

Number of sampled lines

Because of the limited number of bits that can be stored at a reasonable cost, we sample every 4th line of the Even field only, with a total number of 64 sampled lines (all from the Even field).

Since samples are obtained from 64 lines only then to display a complete picture, each sampled line is displayed 4 times in each field, resulting in a total of 8 identical lines being displayed one underneath the other.

Sampling rate

For equal horizontal and vertical resolution, for a given number of sampled lines, one can calculate mathematically the minimum sampling rate. For Engineering purposes though, it was decided that 64 samples per line should be taken at the frequency of 1.28 MHz. 1.28 MHz sampling rate is used because it is directly available from the sync. pulse generator. The need for 64 samples arises from the fact that as this is a binary number (2^6), it is easily handled by binary counters, but perhaps more important it simplified circuit design in the address generator circuits.

It is important to note here, that the A/D converter is set to operate during the active part of a video line because the sync. pulses do not contain any picture information. They are available from other parts of the circuit when they are needed for display purposes.

Fig. 3 shows the points where the first (point A) and the last (Point B) samples are taken.

Table of set standards

Because the need to refer back to these set standards will

probably arise a few times later on, a list of the standards is shown below with some additional information.

Field sampled = Even Field
 Total number of lines sampled = 64 lines
 First line sampled = 19th line
 Lines sampled = Every 4th line

Resolution bits = 4 bits (= 16 grey levels)
 Number of samples per line = 64 samples
 Sampling rate = 1.28 MHz

First line displayed from the:
 Even field = 19th line
 Odd field = 332nd line

Total number of lines displayed = 512 (= 256 + 256)
 Total number of blacked lines = 73 (= 36.5 + 36.5)

Circuit description

Let us now see the basic structure of the system. Fig. 5 shows the circuit block diagram and based on this, a brief description of each block is made below.

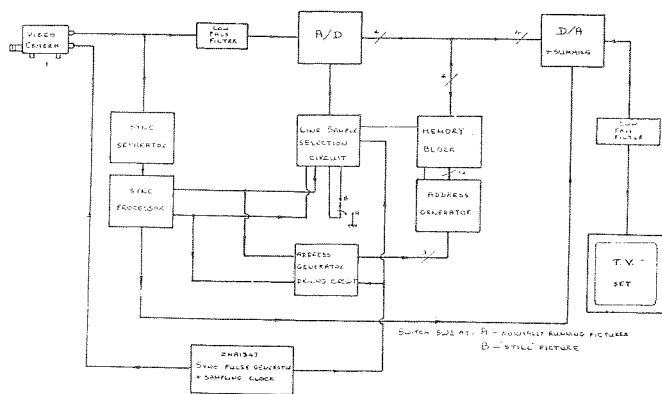


Fig. 5 Circuit Block Diagram

The Video camera used is supposed to be of the cheapest available for small studio use. These types of cameras need all the synchronising pulses provided externally and in our system these are supplied by the sync. pulse generator. This is a single I.C. specifically made for these purposes.

We follow what happens to the output signal of the Video camera.

As seen from the block diagram this is fed simultaneously to the low pass filter and the sync. separator. The latter as the name implies, separates out the synchronising pulses. The sync. processor outputs are the line clock and the «start» of line 1 signal».

The line clock has a period of 64 μ s which corresponds to the time needed by the CRT to scan a line and return to the left of the screen again. This output is needed because as we have to select out lines we have to have something to count lines on.

The start of line 1 signal as the name implies gives out a pulse at the beginning of line 1. We use that to start counting the lines.

The line sample selection circuit is there to tell us which lines to sample with the A/D converter. That is, when signalled that line 1 has started, it starts counting and sig-

nals the A/D converter which lines to sample, i.e. sample line 19, 23 27 etc. While instructing the A/D to sample the line sample selection circuit also sets the Read or write the memory block.

Lets say now that line 19 is present. Line 19 is one of the lines that we sample. Therefore a «Sample» instruction is sent by the line sample selection cct to the A/D converter, and at the same time sets the Read/Write line to write.

So the output of the A/D is sent simultaneously to the A/D converter to be displayed on the screen and to the memory block to be written in.

The address generator generates the addresses so that the samples are stored in the right position and sequence. The next line to be sampled is line 23. So when line 19 finishes the line sample selection circuit inhibits the A/D and sends a Read instruction to the memory. The address generator generates the right addresses so that the samples of line 19 just written in are now read out in the same sequence.

In that way line 19 is displayed on the screen in the position of line 19 and also at the position of lines 20, 21 and 22, See Fig. 2. Line 23 is also sampled and similarly displayed.

Between line 19 and 20 of the even field lies line 332, so the samples of line 19 are also displayed in the opposition of line 332, 333, 334 and 335. By doing that the effect on the screen is that we manage to display one line 8 times.

With the system running like that all the samples from one picture, are replaced by the next picture samples, in the memory. Now with the use of a switch we can inhibit the operation of the A/D converter so that the memory contents do not change according to the input signal. This will have the effect of a frozen picture as the same memory contents are simply read out continuously.

If we want to store the pictures on a magnetic tape we simply read out the memory contents slowly, convert them into serial form and record it on a normal cassette recorder, using Frequency Shift Keying (F.S.K.) modulation.

Applications

This system was originally developed as an aid to eye movement research but the same system as it is can offer other attractive applications.

Instead of connecting the system record output to a tape recorder it can be directly connected to the telephone network so that pictures can be sent over long distances. These might be a display on the oscilloscope, a patients X-Ray pictures or road traffic monitoring.

With a few minor modifications this system can be used to convert a normal oscilloscope into a digital oscilloscope with permanent storage facility on magnetic tape (Video Camera not needed here).

The system just described offers some interesting applications either in using it as it is or by modifying or even discarding parts of it. But imagine the possibilities offered by interfacing the above with a microprocessor.....

STEEL FIBRE REINFORCED CONCRETE MATERIAL PROPERTIES AND STRUCTURAL BEHAVIOUR

By Dr. H. Stavrides, Lecturer, HTI - Nicosia.

Dr. D. Theodorakopoulos, *Consultant Engineer Practising in Greece.*

Summary:-

Tests are reported on the material properties of high workability steel fibre concrete in a cement/fly ash based matrix where 30% by weight of the cement content is replaced by an equal amount of fly ash.

The effects of the size and type of aggregate, the type of aggregate, and the method of casting and compaction are reported.

Further, tests on the structural behaviour of steel fibre reinforced beams are reported with special emphasis given to the moment-rotation characteristics of such beams.

Introduction:-

One of the limitations of fibre reinforced concrete is its lack of adequate workability. The difficulties of placing and compacting fibre concrete, arise from the particle interference between the fibres and the coarse aggregates.

Tests (1,2,3) show that it is not only the fibre geometry and fibre volume that influence the rheological properties of the fresh fibre concrete but also the size, shape and volume fraction of the coarse aggregate. To ensure adequate compactability of the fresh fibre concrete and more importantly to achieve uniform fibre distribution without bundling of fibres it is therefore, necessary to control the relative fibre-aggregate volume in addition to the fibre and aggregate geometry. Conventional concrete mixes cannot therefore be used with steel fibre concrete.

Experience with steel-fibre concrete shows that if conventional procedures and equipment are used for handling and placing it, a higher proportion of finer material is then generally found necessary for fibre concrete than for plain concrete. In comparable plain and fibre concrete mixes about 40% more water content is required for the fibre mix with a 1% volume of fibres of aspect ratio 76. This would reduce the strength and elasticity properties of the fibre concrete and hence it is imperative to improve the workability properties of fibre concrete without necessarily increasing the free water added to the mix. This was achieved by replacing 30% by weight of the O.P.C. by fly ash in conjunction with the use of water reducing admixtures. The fly ash introduction at the rate of 30% did not impair the compressive strength or the elastic properties of the mix.

The main difference between concrete reinforced with short discontinuous fibres and conventional steel bars, is their orientation. That is, whereas reinforcing bars are aligned along the direction of stress the fibres usually have a three dimensional configuration. The test series involving the beams was designed to investigate the effect of fibre volume and fibre orientation on the beam deformation characteristics with particular emphasis given to the moment-rotation characteristics.

I. Material Properties

These tests reported form a small part of a much wider experimental programme the initial stage of which was to design a mix including the optimum fly ash content. This optimum fly ash content was established to be 30% replacement by weight of cement.

To establish the optimum fly ash content, several mixes with fly ash alone varying from 0 to 50% and replacing equal amounts of cement by weight were cast and their strength, elasticity and damping properties determined at various ages. From all these results, the mix with 30% fly ash content gave the optimum strength and elasticity properties. Indeed at six months the 30% fly ash mix had nearly the same flexural strength as the all cement mix; however, the reduction in compressive strength compared to the all cement mix was about 30%.

Effect of aggregate type and size

To study the effects of aggregate type and size on the properties of the fly ash fibre concrete, four different types of aggregates were used with their corresponding mixes in plain concrete without fibres. The details of the mixes are shown in Table 1. The water content for each mix was adjusted to give approximately similar workability properties, although the granite concrete mixes were consistently less workable. All the mixes had the same fibre volume of 1% of 0.5 x 38,1 mm straight round fibres.

The crushed gravel aggregate was used both in the graded form and as a single-size. The limestone and granite aggregates were used as single sizes. The lightweight aggregate was also single-sized with 10 mm maximum. All the test specimens were cast in steel moulds and compacted by table vibration. They were demoulded at 24 hours and subsequently cured under controlled conditions of temperature of $60 \pm 2^{\circ}\text{F}$. Only data concerning flexural and compressive strengths are reported here.

TABLE 1 Details of mixes used.

Mix	Type of aggregate	Mix proportions*	28 day strength		Slump mm		V.B. time secs	
			Flexu- ral N/mm ²	Compre- ssive N/mm ²	Fibre mix	Plain mix ***	F.m	P.m
D	10mm Gravel	1:1.8:2.25/0.42	7.25	44.30	90	175	4	1
F	20mm Gravel	1:1.8:2.25/0.40	5.93	42.20	100	180	3	1
G	20mm Gravel ***	1:1.8:2.25/0.40	5.50	40.00	110	185	3	1
H	10mm Limestone***	1:1.8:2.25/0.44	6.21	37.00	100	180	3	1
I	20mm Limestone***	1:1.8:2.25/0.40	5.37	41.15	130	210	2	0.5
J	20mm Granite***	1:1.8:2.25/0.40	7.00	48.10	40	80	8	4
K	25mm Granite***	1:1.8:2.25/0.40	6.50	44.20	45	90	8	4
L	38mm Granite***	1:1.8:2.25/0.40	5.20	42.30	50	100	7	3
M	10mm Lightweight(Lytag)	1:1.05:2.45/0.50	4.78	30.40	100	180	3	1

Notes: * All mixes include 30% p.f.a by weight of cement and 280 gm of water-reducer per 50kg of (cement+ p.f.a)

** The plain concrete mixes had exactly the same mix proportions as the fibre concrete mixes.

*** Single size grading

+ Fibre concrete strength
Fibres used: Cold drawn straight round steel fibres 0.5x38.1mm

Effect on flexural strength

The flexural strength results of the fibre concrete mixes are shown in Table 1. The results show that the larger the size of the aggregate, the lower the ultimate flexural strength. Table 1 also shows that the increase in flexural strength due to the presence of fibres is more pronounced in mixes with smaller maximum aggregate sizes. With the 20 mm granite mix, for example, the increase in flexural strength of the fibre concrete over the corresponding unreinforced mix was about 46%, whereas when the aggregate size was increased to 38 mm, the increase in strength was reduced to 30%.

However, aggregate geometry and surface texture also influence the effect of the fibre presence on flexural strength. With both 10 mm and 20 mm aggregates, the

rougher the aggregate surface and shape, the less efficient the fibres appeared to be in their role as crack arrestors although the 20 mm granite concrete gave better results than the crushed gravel or limestone concrete. Whereas in plain concrete the crushed aggregates lead to higher flexural strength, in fibre concrete more evenly shaped aggregates were generally found to render the fibres more effective.

Although limited, the results also showed some effect of aggregate grading on flexural strength. Whereas in plain concrete higher strengths could be achieved through gap grading, particularly for stiff mixes (4), the direct contact of aggregates achieved with gap grading appeared to limit the effectiveness of the fibres. In the tests reported here, the single size gradation gave marginal increases in flexural strength for the plain concrete mixes; however, the situation was reversed with the corresponding fibre concrete mixes. Single size aggregates in fibre concrete showed a distinct reduction in flexural strength, and it appears that in fibre concrete large single sized aggregates cannot produce a better performance than that obtained with continuous grading of aggregates.

Although all the fibre concrete mixes showed first cracking load distinct from the ultimate strength, the smaller maximum aggregate sizes and the smoother aggregates showed better postcracking behaviour. With larger aggregates the bond area is smaller and the bond failure at the aggregate-matrix interface becomes more critical (5). The fibre-aggregate interparticle friction appears to be more pronounced with irregularly shaped aggregates, and the fibres become distorted and their efficiency as long and straight crack arrestors, reduced. As a result, a large proportion of the fibres is reduced to act as mere solid inclusions than as effective crack arrestors. The smaller and smoother aggregates, give more scope to the fibres to embed themselves undistorted in the matrix, and hence act more efficiently in arresting propagation of cracks. The fibres are thus more efficiently oriented and more effectively embedded in the mortar matrix to continue to carry the load after the formation of the first crack.

Visual and microscopic examination of the fractured surfaces as well as x-ray examination of slices confirmed the above observations. Aggregate-matrix bond depends primarily on the surface texture of the aggregate, and has an important influence on the strength of concrete, particularly the flexural strength (5), however, size is also an important factor, especially in fibre concrete. With larger aggregate sizes, the fibres become less effective due to the aggregate-fibre interaction; when the aggregate size then reaches that of the fibre length, the propagation of flexural cracks is influenced more by the distribution of aggregate particles than by fibre distribution. X-ray studies have confirmed the aggregate-fibre interaction; the tests also showed that with aggregates larger than 20 mm, the cracks invariably propagated in a more erratic manner, indicating that with larger aggregates, it is the aggregate size which is the crucial factor in crack propagation and not the fibre distribution.

Effect on compressive strength

Compressive strength is influenced in the same way as flexural strength by the size and type of the aggregate, but to a much smaller scale. The effect on compressive

strength of the 1% fibre content in all the mixes used was practically negligible. All the fibre concrete mixes showed an increase in compressive strength over the corresponding plain concrete mixes, varying from 0 to 3% for the natural aggregates, and 7% for the lightweight concrete, with the exception of the 10mm limestone and the lightweight aggregate the average compressive strength at 28 days varied between 40 and 48 N/mm²; the lightweight concrete gave a strength of 30 N/mm². These tests show that with adequately workable mixes the presence of fibres need cause no reduction in compressive strength (1), and indeed give a modest increase.

Effect of method of casting

The orientation of the fibres relative to the stress trajectories is a major factor in their efficiency. When short discrete fibres are mixed in a concrete, the orientation tends to be largely random three-dimensional, at least just after the concrete has been mixed. The only stage during which some kind of redistribution and reorientation of the fibres can occur is during the casting-compacting stage. Under table vibration, steel fibres tend to align in planes at right angles to the direction of vibration (6). In this test series the effect of the method of casting, horizontal or vertical, in connection with two different methods of vibration, external and internal, has been studied. Although the problem has been studied for different types of aggregates, and different properties, only data concerning 10 mm crushed gravel and flexural strength and dynamic modulus are reported here.

The mix proportions used for the fly ash fibre concrete were the same as before with fibre volume varying from 0 to 1.25%. All the beams were demoulded at 24 hours and cured under constant temperature and humidity conditions for 27 days, and tested dry. Four types of beams were tested, namely,

Type A1 - beams cast horizontally and vibrated externally

Type A2 - beams cast vertically and vibrated externally

Type B1 - beams cast horizontally and vibrated internally

Type B2 - beams cast vertically and vibrated internally.

The influence of the method of casting and type of vibration on the flexural strength of fly ash fibre concrete for various fibre contents is shown in Fig. 1. The results show that when fibre concrete specimens are cast horizontally external vibration gives the optimum strength whereas if the specimens are cast vertically, internal vibration is more effective than external vibration. The results confirm that horizontal casting and external vibration are the most efficient method of casting and compacting fibre concrete and that fibre orientation occurs during the casting-compacting stage.

When fibre concrete is cast horizontally, the reduction in strength due to internal vibration is only marginal, the maximum being 5%. The effect of vertical casting on flexural strength is, however, substantial, the reduction in strength, compared to external vibration of horizontally cast beams, varying up to 32% under internal vibration and 35% under external vibration. Internal vibration consistently produced higher flexural strength with vertical

casting, the increase compared to external vibration varying from 3% to 8%. The results give strong evidence of fibre alignment in vertically cast sections under internal and external compaction methods.

It is interesting to note that the flexural strength of specimens with 0.5% and 0.75% fibre content, cast vertically, were even smaller than that of the plain concrete specimens cast horizontally and externally vibrated. The specimens with 1% fibre content cast vertically were only marginally stronger than the plain concrete specimens cast horizontally. The fact that the flexural strength of fibre concrete could be smaller than of plain concrete cast in a different way cannot be explained only in terms of favourable and unfavourable fibre alignment. The full explanation to this must lie in the creation of weak bond characteristics and imperfections (6,7), which not only weaken the fibre concrete but reduce the strength to such an extent that fibres no longer act as agents of increasing flexural strength.

It must also be added that the combination of the fibre length (38 mm) and the dimensions of the specimen (100 x 100 x 500 mm) may have contributed to the creation of such imperfections. It is probable that in a specimen of larger cross-sectional area, the effect of vertical casting may not be so severe.

Examination of fractured surfaces showed that fibre orientation and fibre distribution were clearly affected by the method of casting and the type of vibration. In a horizontally cast specimen, a large proportion of the fibres will be acting directly along the stress trajectories, whereas in vertically cast specimens, the fibres will be in a direction at right angles to the direction of stress, thus contributing very little to the flexural strength. At the initial stages of external vibration in the vertically cast specimens, fibres could be seen to rotate and occupy horizontal directions.

Effect on dynamic modulus

The influence of the method of casting and type of vibration on the dynamic modulus for various fibre contents is shown in Fig. 1. The results show two important conclusions-whatever be the method of casting-internal vibration consistently gave higher modulus than external vibration. Secondly, for a given type of vibration, horizontally cast sections gave consistently higher modulus than vertically cast specimens. However, the variations in the dynamic modulus due to casting or compaction were only marginal and within 5%. In general the reduction in dynamic modulus was larger in the externally vibrated beams.

Conclusions

The smaller and smoother the coarse aggregate, the higher the flexural strength and the better the post-cracking behaviour of the fibre concrete.

With large aggregate sizes, the fibres become less effective due to aggregate-fibre interaction and this interparticle friction becomes more pronounced with irregularly shaped aggregates. When the aggregate size reaches that of the fibre length, the propagation of flexural cracks is influenced more by the distribution of aggregate particles than by fibre distribution.

With adequately workable mixes, the presence of fibres causes no reduction in compressive strength.

Both the method of casting and the type of vibration affected the flexural strength and, to a lesser extent, the elastic properties of the fibre concrete.

When fibre concrete is cast horizontally, the reduction in strength due to internal vibration was less than 5%. The effect of vertical casting on flexural strength was more substantial, the reduction in strength, compared to externally vibrated horizontally cast sections, was 30-35% irrespective of the mode of vibration.

The results showed that vertical casting not only produced unfavourable fibre alignment but also created weak bond characteristics and internal imperfections.

The variations in the dynamic modulus due to variations in casting or compaction were only marginal and within 5%.

II Beam Tests

Altogether 10 beams were cast, seven with high yield steel of $f_y = 617 \text{ N/mm}^2$ and three with Tor steel of $f_y = 475 \text{ N/mm}^2$. All the tests were conducted on simple-span beams loaded at midspan with a concentrated load. Figs 2 and 3 show the instrumentation and reinforcement details of the test beams respectively.

The central load was transmitted through a 50mm plate. A calibrated load cell was used for the load transmission. Concrete compressive strains were measured by means of a 100 mm gauge length demec gauge. The demec strain gauge layout points interval was 12.5 mm.

Deflections were measured by means of dial gauges at five positions along the beam as shown in Fig.2. Rotations were measured by a clinometer. Strains on the tensile steel were measured by means of 10 mm gauge length electrical resistance strain gauges. Rotations and compressive concrete strains were measured on one side of the beam and assumed to be the same over the other (symmetrical) half of the beam. The same basic mix was used as for the previous tests with a W/C ratio of 0.45. The full details of all the beams are given in Table 2.

Figure 1 The effect of depth and length of test specimen on the flexural strength of fly ash fibre concrete.

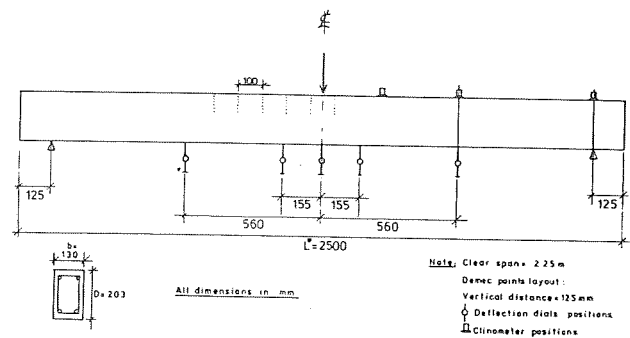
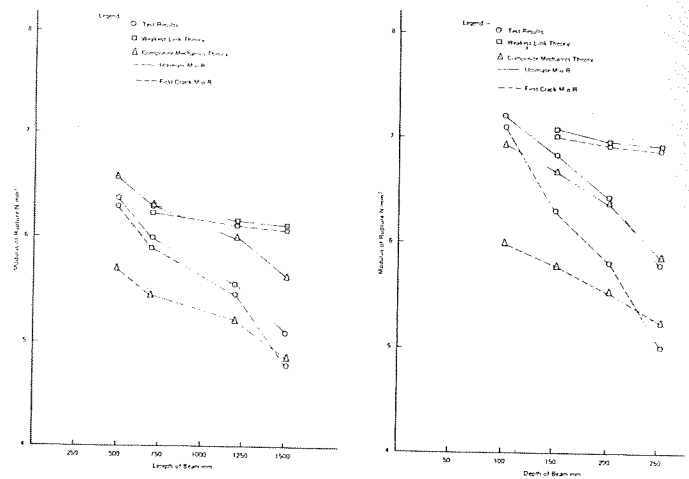


FIG 2 BEAM INSTRUMENTATION.

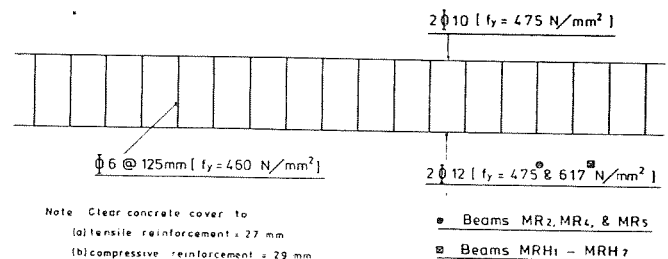


Fig 3 REINFORCEMENT DETAILS

BEAM	COMPRESSION ZONE					TENSILE ZONE					
	Fibre Volume V_f (%)	Fibre Type	Fibres $d_f \times l_f$ (mm x mm)	Fibre Distribution	Plasticizer	Cube Strength f_{cu} (N/mm^2)	Fibre Volume V_f (%)	Fibre Type	Fibres $d_f \times l_f$ (mm x mm)	Fibre Distribution	Plasticizer
MR1	0.0	-	-	-	Febflow 280 gm per 50 kg of c + pfa	37.5	0.0	-	-	-	Same as for compression zone
MR2	1.0	Crisped	0.5x5.0	3D	"	39.0	1.0	Straight	1 x 100	3D - 2D	"
MR3	1.0	"	"	"	"	39.0	0.0	-	-	-	"
MR4	1.0	"	"	"	"	39.0	1.0	Straight	1 x 100	2D - 1D	"
MR5	0.5	"	"	"	"	38.5	0.5	"	"	"	"
MR6	1.0	"	"	"	Polymer 27 by weight of water content	36.0	1.0	"	"	"	"
MR7	1.0	"	"	"	Polymer 102 by wt. of water content	35.0	1.0	"	"	"	"
MR2	1.0	"	"	"	Febflow 280 gm per 50 kg of c + pfa	39.0	1.0	"	"	3D - 2D	"
MR4	1.0	"	"	"	"	39.0	1.0	"	"	2D - 1D	"
MR5	0.5	"	"	"	"	38.5	0.5	"	"	2D - 1D	"

Notes: MR1 Beams - H.Y. steel for Tensile Reinforcement. MR Beams - Tor Steel for Tensile Reinforcement. c = cement.

Table 2. Beam Details.

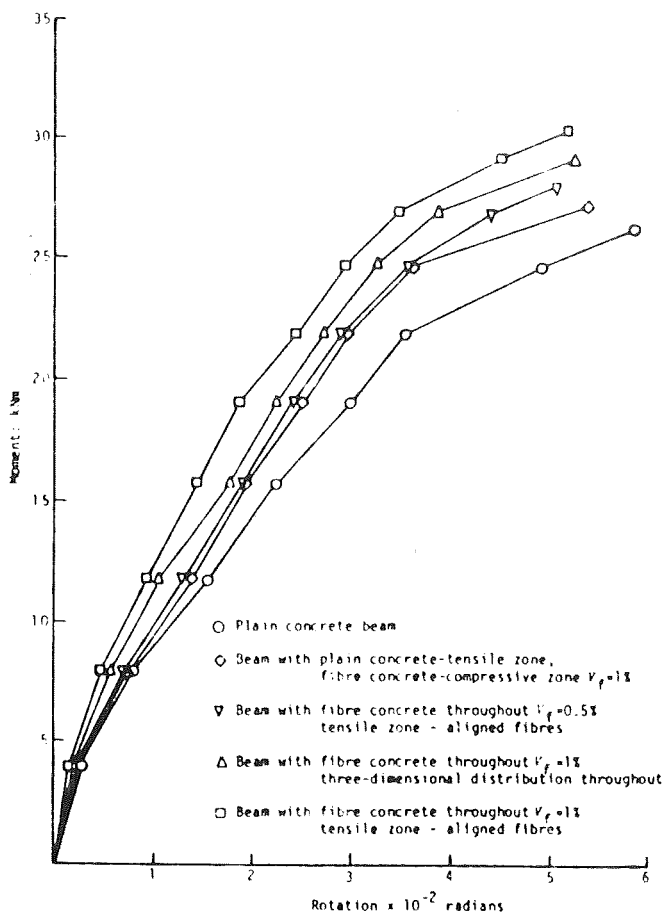


FIG. 4.

Main results and conclusions

The deformation characteristics of the beams with aligned fibres in the tensile zone were found to be superior to those of the plain concrete beam and the beam with the three dimensional distribution of fibres in the tensile zone.

Alignment of fibres in the tensile zone led to a reduction in rotations, deflexions and maximum concrete compressive strains. The increase in ultimate strength, compared with the plain concrete beam was 11% for the beam reinforced with 1% of non-aligned fibres, and 15% for the beam reinforced with 1% of aligned fibres. Fig. 4 shows

some typical results of the Moment-Rotation characteristics.

These results show that reinforcement with higher characteristic strength (even higher than 460 N/mm²) may be used efficiently and economically with a fibre tensile skin with all the advantages of less congestion and saving in steel. The increased cracking and deflection arising from the higher steel service stress will be controlled to within acceptable limits by the presence of fibres.

References

1. Swamy, R N and Mangat, P S, Influence of fibre geometry on the properties of steel fibre reinforced concrete. Cement and Concrete Research, Vol 4 and No.3, May 1974, pp 451-465.
2. Edgington, J, Hannant, D J and Williams, R J T, Steel fibre reinforced concrete. Current Paper CP69/74, Building Research Establishment, Department of the Environment, July 1974, p 17.
3. Swamy, R N and Mangat, P S Influence of fibre-aggregate interaction on some properties of steel fibre reinforced concrete. RILEM Materials and Structures, Vol 7, No 41, Sept-Oct 1974,
4. Remakrishnan, V, Contribution of gap-grading to the development of high strength concrete. Paper presented at the Canadian Capital Seminar, Ottawa, Canada, Oct 1973, p 14.
5. Swamy, R N, Aggregate-matrix interaction in concrete systems. Proc. Civil Engineering Materials Conference, University of Southampton, 1969, Wiley, Interscience, Part 1, 1971, pp 301-315.
6. Williamson, G R, Fibrous reinforcement for Portland cement. Technical Report No 2-40, US Army Engineer Division, Ohio river, Cincinnati, May 1965, p 29.
7. Hughes, B P and Ash, J E Water gain and its effects on concrete. Concrete, Vol 3, No 12, Dec 1969, pp 494-498.

Part of this paper was presented in the 5th Hellenic Symposium on reinforced concrete, held on the 7, 8 and 9th May 1981 in Nicosia.

TOUGHNESS AND BRITTLE FAILURE OF METALS

by G. Katodrytes
Lecturer, HTI

1. Introduction

FRACTURE is the separation, or fragmentation, of a solid body into two or more parts under the action of stress. The process of brittle fracture can be considered to be made up of two components, crack initiation and crack propagation.

Conventional engineering design is based on the avoidance of failure by general plastic collapse. The material property specified in design codes is the flow stress which is usually the yield stress or 0.2% proof stress. The DESIGN STRESS is determined by dividing the applied stress calculated to cause collapse by a SAFETY FACTOR. The role of the safety factor is to take into account any extra stresses imposed during erection, fabrication or service, which may raise the applied stress to the value required to cause plastic collapse and failure.

The safety factor really does not recognise the possibility of failure by brittle fracture. It was generally believed that the safety factor could «safeguard» against this type of low stress fracture by the use of higher figures of safety factor. This was proved not to be true, since total failure of components or structures have occurred in the presence of a material defect or crack at stresses well below the design stress.

The meaning of the terms «toughness» and «brittleness» as used for metals is really inter-related because when we talk about toughness of metals we mean the absence of brittleness. This article intends to deal mainly with brittle fracture of engineering materials which is the most important since it occurs without warning and usually produces disastrous consequences. Such fracture in metals is characterized by a rapid rate of crack propagation, with no gross deformation and very little microdeformation.

2. Toughness — notch toughness

TOUGHNESS is the capacity of a material to absorb energy by deforming plastically before fracture. A more generally accepted meaning of toughness is resistance to rapid crack propagation or the absence of brittleness. Toughness is influenced by the chemical composition and physical properties of the material. Alloying elements, gas content and impurities are the chemical factors affecting this property. The physical factors include hardness, microstructure, homogeneity, grain size, section size, rolling direction, hot and cold working temperatures and method of fabrication.

The consideration of toughness during design of a part will permit selection of materials with low probability of failure by fracture, and its consideration during failure analysis often is necessary to establish the conditions that led to fracture.

NOTCH-TOUGHNESS is usually evaluated by testing prescribed notched-bar specimens at known temperatures in a single-blow pendulum type impact machine. Results are reported in ft-lb of impact energy absorbed by the test specimen. The Charpy and Izod methods of notched-bar impact testing (according to BS. 131) are used for notch toughness determinations. Out of these two, the Charpy test was found to be the most reliable and reproducible.

Investigations on toughness have begun after the brittle failure of welded liberty ships and T-2 tankers during World War II. Some of these ships broke completely in two, while in other instances the fracture did not completely disable the ship. Most of the failures occurred during winter months when the ships were both in heavy seas and anchored at docks. From this it has become obvious that the ductile material mild steel can become brittle under certain conditions. During these investigations several other test methods have been developed (apart from the Izod and Charpy) such as the drop weight test, the explosion-

bulge test, the Navy (or Kahn) tear test and various slow bend tests including the Lehigh bend test.

Researchers showed that three basic factors contribute to a brittle-cleavage type of fracture.

These are

- (a) a triaxial state of stress
- (b) a low temperature
- and (c) a high strain rate or rapid rate of loading.

All three of these factors do not have to be present at the same time to produce brittle fracture. A triaxial state of stress, such as exists at a notch and a low temperature are responsible for most service failures of the brittle type. As far as the low temperature factor is concerned, researchers showed that there is a transition temperature below which a ductile material like mild steel at room temperature can become brittle.

The Izod and Charpy tests tell us almost nothing but they do probably have some values as rough comparative tests between different materials. The Izod and Charpy figures have no design value because geometrically similar notches do not produce the same results on large parts as they do on small Izod and Charpy test pieces. These tests are useful to the metallurgist in detecting differences due to casting, mechanical and heat treatment, not indicated by the tensile test. For material susceptible to notch-brittle fracture, they give a guide to the resistance against failure at a discontinuity or change in section and also indicate the resistance of a material to the «spread» of a crack after it has formed. Such notched - bar test results form no basis for approval or condemnation of a metal for services under conditions of notch fatigue.

3. Fracture toughness

The investigations of brittle fracture of World War II ship plates led to new methods for evaluation of notch toughness, mentioned earlier in this article. The toughness para-

meters measured by these tests, however, have the same limitations as the older notched-bar impact tests (Izod and Charpy) in that the parameters are not material constants. Instead, they are affected by the size and shape of the specimen and its notch. Thus, a new parameter was needed, one that was a material constant. Through application of the concepts of Fracture Mechanics, which are mentioned in the following section, a parameter called fracture toughness (K) was developed.

FRACTURE TOUGHNESS is the property which measures resistance to fast crack propagation in materials. A more detailed definition for plane strain fracture toughness (K_{IC}) is given in B.S.5447:1977. According to this standard, it is a property of a material indicative of the materials resistance to crack growth under conditions in which plastic deformation is limited.

It is the critical value of K (K_C) at which the first significant extension of the crack occurs under the influence of a rising force under conditions of high constraint to plastic deformation.

Values of K_C may be determined by testing specimens that are designed to produce mode I (opening mode) crack deformation according to B.S. 5447:1977 and in this case they are given the designation K_{IC} . When K_{IC} is considered in design and in material selection, the likelihood of choosing the correct material, of properly evaluating the potential danger of a flaw, and of preventing catastrophic fracture are improved. Component fracture can be predicted in terms of applied stress and probable flaw size by applying appropriate equations to real structures.

4. Fracture Mechanics

FRACTURE MECHANICS is the branch in engineering which deals with crack-defects in metals and brittle failure. The significance of crack-defects becomes evident from the fact that higher safety factors are used for castings than for wrought materials because of fear that the castings might contain more inherent defects, which could lead to fast crack propagation at or below the applied design stress. In other words these defects in the

material act as *stress concentrators*.

Fracture mechanics includes concepts which provide a quantitative framework for evaluating structural reliability in terms of applied stress, crack length, and stress intensity at the crack-tip. The linear-elastic fracture mechanics approach to fracture analysis includes three major assumptions:

1. Cracks and similar flaws are inherently present in parts or specimens.
2. A crack is a flat, internal free surface in a linear elastic-stress field.
3. The quantity of stored energy released from a cracking specimen or part during rapid crack propagation is a basic material property, independent of specimen or part size.

By considering what it has been said about castings at the beginning of this section and also due to the fact that cracks are often present in sizes below the limit of sensitivity of non-destructive inspection tests, the first assumption is true. The second assumption is introduced to allow a mathematical description of the stresses in the vicinity of the crack tip.

The third assumption states that rapid crack propagation is controlled solely by a material constant. This constant, which is called the critical stress-intensity factor, K_C , is that value of the stress-intensity factor, K , at which crack propagation becomes rapid.

The greater the value of K_C , the greater rapid propagation and greater the resistance of the material to brittle fracture. The critical stress intensity factor (K_C), which also is called the plane-stress fracture toughness is directly related to the energy required for rapid crack propagation (G_C) by the formula, $K_C^2 = E.G_C$, where E is the elastic modulus.

Fracture mechanics can be utilised in designing, and predicting service life of, pressure vessels and other engineering components in which subcritical flow growth, or time-dependent fractures such as those stemming from stress-corrosion cracking or fatigue are important.

5. Conclusions

Going through this article, one can appreciate the importance of brittle behaviour in metals and the consequent disastrous brittle failure. We are all aware of the fact that too many engineering failures still occur, not because of unknown phenomena, but because existing knowledge has not been fully utilised. In 1954 the failures of the Comet aircraft occurred, which were then attributed to fatigue. It was later found that these failures were due to fast unstable fractures starting from small cracks.

The roots of fracture mechanics can be traced back to the 1920's when A.A. Griffith developed his theory on crack propagation and then followed by Orowan and Irwin who modified the Griffith's relationship. Since then many other researchers were involved to the science of fracture mechanics by developing various concepts on which nowadays Fracture Mechanics is based.

Fracture mechanics has been used extensively over the last 20 years in high technology, such as rocket motor casings, aircraft design, military applications and nuclear vessels. It has been mis-used in some areas, and has not been used extensively in general engineering.

There is no doubt that fracture mechanics has much to offer in the field of prevention of brittle failure because it provides a basic new dimension to the understanding of behaviour of materials under stress, and ought to be a part of the education of every engineer who will be concerned with design, manufacture of materials for engineering components or structures.

References

1. Failure analysis and prevention, volume 10, Metals Handbook, American Society for Metals.
2. Worked examples in Fracture Mechanics, by J.F. Knott, D.Elliot, The Institution of Metallurgists.
3. Mechanical Metallurgy, by G.E. Dieter
4. B.S. 5447:1977
5. Mechanical Engineering News; February, 1981

ELECTRONIC STRUCTURE AND POLARIZATION OF PHYSISORBED INERT ATOMS DUE TO THE SHORT RANGE INTERACTION WITH THE METAL SUBSTRATE**

By Dr. G. Oxinos.
Lecturer, H.T.I.

**Presented in part at the Second European Conference on Surface Science, Cambridge, England, March 26-29, 1979 as paper P12.

ABSTRACT

We present a study of the electronic structure and polarization of physisorbed inert atoms (Ne, Ar and Kr) due to the short range interaction with the metal substrate. The potential inside the metal is replaced by a constant and the metal-vacuum interface is represented by a step barrier. The adsorbed atom is represented by a spherical potential of the muffin-tin type superimposed on the constant potential on the vacuum side of the metal-vacuum interface. The potential within the adatom sphere is replaced by that of the free inert atom as calculated by Schwarz¹⁵. We calculate the Local Density of States of the metal-adatom system, the induced dipole moment, and the binding energy of the adatom. The effect on the induced polarization of the geometry of the surface and of the crystal potential is treated on a semi-empirical basis. Our numerical results are in reasonably good agreement with the available experimental data.

1. INTRODUCTION

The problem of calculating the Local Density of States (LDS) in the region of atom adsorbed on the surface of a metal has attracted considerable attention in recent years.¹⁻⁶ Most of the existing theories¹⁻⁴ use in some form or other the concept of a «surface molecule». According to this concept the LDS in and around the adsorbed atom is determined by a small cluster of atoms, a «surface molecule», which contains besides the adsorbed atom a sufficient number of the neighbouring metal atoms. A Hamiltonian is then constructed using basis functions which are localized on the atoms of the «surface molecule». The manner in which the LDS is obtained from this Hamiltonian varies from one theory to another. Unfortunately the number of metal atoms that must be included in the «surface molecule» in order to obtain satisfactory results for real metal-adatom systems is not always small⁶. In order to deal with those cases where a small cluster of atoms **cannot** represent adequately the metal substrate, we have recently^{7,18} proposed alternative formulations of the problem which treat the metal substrate as a semi-infinite crystal. In ref. 7 we have described in general terms the electronic states of a model Hamiltonian representing a single impurity atom adsorbed on the surface of a semi-infinite crystal. The theory we presented provides a clear understanding of the origin and nature of the different electronic states that exist, or may exist, in a metal-adatom system and the means for calculating the corresponding wave functions. In ref. 18 we have presented an alternative formulation of the problem using Green's functions. This formalism, which avoids the explicit evaluation of the wave functions of the individual electronic states of the metal-adatom system, has the advantage of being computationally more efficient. We demonstrated the Green's function method by applying it to study the electronic structure of atoms adsorbed on metals using the simplest possible model of a metal-adatom system. For this model we presented numerical results for the LDS in the region of the adatom, when the valence state in the atom is an s-state, a p-state or a d-state. We also examined the case of an adatom with adjacent in energy s- and p-states, similarly s- and d-states. We found that the interaction of these states through the metal is considerable, and may be of critical importance in the interpretation of available experimental data²².

In the present paper we present a study of the electronic structure and polarization of physisorbed inert atoms (Ne, Ar and Kr) due to the short range interaction with the metal substrate. The adsorption of inert atoms on metals has been studied experimentally by Mignolet⁸, by Ehrlich and Hudda⁹, and by Gomer¹⁰. Mignolet measured the contact potential of Xe adsorbed on a variety of clean metal surfaces and found a high reduction in the work function Φ for some of these metals and especially for tungsten. His results are summarized in Table 1. Ehrlich and Hudda⁹ and Gomer¹⁰ investigated the adsorption of the inert atoms on tungsten and also found high reductions in Φ . More recently Engel and Gomer¹¹ measured the reduction in Φ following the adsorption of Ar, Kr, and Xe on single crystal planes of tungsten. Their results are shown in Table 2 for the case of Ar and Kr. The binding energy of the adatoms has also been measured^{9,11}. The experimental results are summarized in Table 3.

It is usually assumed that the inert atoms are bound to the surface by a van der Waal's interaction

$$\omega = -C/Z_a^3 \quad (1)$$

where Z_a is the distance from the surface. There are a number of theories^{12,13} concerned with the evaluation of C in (1), which are reasonably valid for sufficiently large values of Z_a . However, the validity of these theories for small values of Z_a , when the electronic clouds of the metal and the adatom begin to overlap, is extremely doubtful. Even if one can obtain reasonable values for the binding energies on the basis of (1), and this is not always the case¹¹, a van der Waal's interaction **cannot** explain the observed polarization of the adsorbed atoms. Different mechanisms have been postulated by different authors to explain the observed polarization. Ehrlich and Hudda⁹ suggested that the atoms are polarized by the surface field, but as Gomer^{10,11} pointed out the small extension of this field relative to the size of the adsorbed atoms makes this explanation rather unlikely. The latter author proposed an alternative mechanism^{10,11} on the basis of Mulliken's idea of a no-bond charge transfer complex¹⁴, but, so far, no quantitative theory has been formulated based on this idea.

In this paper we investigate the interaction of an inert atom with a metal substrate using a model Hamiltonian for the metal-adatom system which allows us to obtain the electronic states of the combined system without any significant approximations except for those involved in the construction of the model potential.

TABLE 1
Reduction of work function due to Xe adsorption⁸

Metal	Ti	Cr	Fe	Ni	Zn	Se	W	Hg
$\Delta\phi$ (eV)	0.84	0.90	0.66	0.85	0.21	0.096	1.14	0.23

TABLE 2

The observed reduction in the work function $\Delta\phi$ of tungsten at monolayer coverage, and adsorbate induced dipole moments at zero coverage estimated from experiment¹¹. Calculated values of dipole moments according to the present theory.

Neon^(a)

$\Delta\phi$ (experimental) = 0.15 eV

$\Delta\phi$ (theory) = 0.19 (0.15)eV

Argon^(b)

Plane	$\Delta\phi$ (eV)	(1) μ (debye)	(2) μ (debye)	μ theory (debye)
(110)	0.85	0.29	0.29	0.183
(100)	0.46	0.31	0.49	0.215
(112)	0.34	0.29	0.53	0.228
(111)	0.40	0.16	0.44	0.244
(012)	0.70	0.40	0.70 (1.41)	0.250

Krypton^(b)

Plane	$\Delta\phi$ (eV)	(1) μ (debye)	(2) μ (debye)	μ theory (debye)
(110)	1.97	1.93	1.93	0.298
(100)	0.83	0.38	0.55	0.325
(112)	0.58	0.44	0.77	0.335
(111)	0.83	0.50	1.24	0.349
(012)	0.95	0.43	0.69 (1.38)	0.354

(a) There are no experimental data for adsorption on single planes. The experimental value was obtained from ref. 10. The theoretical value was calculated using $Q = 0.48$ (i.e. $N = 5$) and assuming a maximum coverage of 7.9×10^{14} adsorbed atoms/cm². The theoretical value in parenthesis corresponds to a density of 6.2×10^{14} adsorbed atoms/cm².

(b) The prescription for calculating μ (1) and μ (2) from the experimental data is given in the text.

TABLE 3

Experimental¹¹ and theoretical binding energies in (eV/atom) of Ne, Ar and Kr on tungsten.

Adsorbed atom	$-\Delta E^{(a)}$ (experiment)	$-\Delta E^{(b)}$ (theory)
Ne		0.104
Ar	0.087 - 0.119	0.127 (0.073)
Kr	0.253 - 0.374	0.247 (0.162)

(a) For Ne, there are no experimental data. For Ar and Kr the values given represent lower and upper bounds obtained from ref. 11 in the manner described in the text.

(b) For Ar and Kr the calculated values in parenthesis correspond to a metal-atom separation such that $Z_a = (a_0 + 0.2)\text{\AA}$.

2. THE MODEL

The metal-vacuum interface is taken at $z=0$, with the positive z -direction pointing outwards from the metal. Outside the metal ($z>0$) the potential is given by

$$U = v_a(|\underline{r}-\underline{R}_a|) \quad \text{for } |\underline{r}-\underline{R}_a| < a_0 \quad (2a)$$

$$= 0 \quad \text{for } |\underline{r}-\underline{R}_a| > a_0, z > 0$$

Inside the metal the potential is replaced by a constant, i.e.,

$$U = V_0 \quad \text{for } z < 0 \quad (2b)$$

$v_a(|\underline{r}-\underline{R}_a|)$ represents the potential one electron sees within the adsorbed atom. Because the inert atoms interact weakly with the metal, we can replace this potential by the one the electron sees in the free atom. We used the self-consistent potentials of the free atoms as calculated by Schwarz¹⁵ using the Xa method. The radius of the atom sphere a_0 in (2a) was taken equal to the corresponding atomic radius, i.e. $a_0 = 1.577\text{\AA}$, 1.876\AA , 2.011\AA , for Ne, Ar, and Kr respectively. We note that truncating the atomic potential of Schwarz at $r = a_0$ produced a negligible shift in the «eigenvalues» of the «electronic states» of the atom as defined in the Xa method. We emphasize that these «eigenvalues» are not to be confused with the Hartree-Fock eigenvalues and hence with the ionization energies of the atom¹⁶. The nucleus of the adsorbed atom is situated at $\underline{R}_a = (0,0,Z_a)$ and we have assumed that at equilibrium $Z_a = a_0$. In all our calculations we have taken $V_0 = -13$ eV. Replacing the metal potential by a constant (jellium model) might be a good approximation for some metals but it is not a good approximation for transition metals. In the present calculation, we shall take into account the effect of the crystal potential only approximately and on a semi-empirical basis. We proceed as follows.

3. THE LOCAL DENSITY OF THE STATES AND POLARIZATION

The Local Density of States, $\rho_M(E, \underline{r})$, for the unperturbed semi-infinite metal [$v_a(|\underline{r}-\underline{R}_a|) = 0$ in (2.2a)] is given by

$$\rho_M(E, \underline{r}) = \frac{V}{4\pi^3} \int \int_{|\underline{k}_{11}| < k_{11, \max}} d^2 k_{11} \left(\frac{\partial E}{\partial k_{z; k_{11}}} \right)^{-1} |\psi_0(\underline{r})|^2, \quad E > V_0 \quad (3)$$

where the integration extends over those values of K_{11} such that

$$|\underline{k}_{11}| < k_{11, \max} = \left[\frac{2m}{\hbar^2} (E - V_0) \right]^{\frac{1}{2}}, \quad \text{and}$$

$$\psi_0(\underline{r}) = \frac{1}{\sqrt{2}} \exp(i\underline{k}_{k_{11}}^+ \cdot \underline{r}) + \frac{1}{\sqrt{2}} R^{LL}(k_{11}) \exp(i\underline{k}_{k_{11}}^- \cdot \underline{r}), \quad z < 0$$

$$\psi_0(\underline{r}) = \frac{1}{\sqrt{2}} T^{LR}(k_{11}) \exp(i\underline{q}_{k_{11}}^+ \cdot \underline{r}), \quad z > 0 \quad (4b)$$

$$\underline{k}_{k_{11}}^{\pm} \equiv (\underline{k}_{11}, \pm k_{z; k_{11}}) = (\underline{k}_{11}, \pm \left[\frac{2m}{\hbar^2} (E - V_0) - k_{11}^2 \right]^{\frac{1}{2}}) \quad (5)$$

$$\underline{q}_{k_{11}}^{\pm} \equiv (\underline{k}_{11}, \pm q_{z; k_{11}}) = (\underline{k}_{11}, \pm i \left[\frac{2m}{\hbar^2} (E) + k_{11}^2 \right]^{\frac{1}{2}}) \quad (6)$$

$$\left(\frac{\partial E}{\partial k_{z; k_{11}}} \right)^{-1} = \frac{m}{\hbar^2} \frac{1}{k_{z; k_{11}}} \quad (7)$$

$$R^{LL}(k_{11}) = \frac{(k_{z;k_{11}} - q_{z;k_{11}})}{(k_{z;k_{11}} + q_{z;k_{11}})} \quad (8)$$

$$T^{LR}(k_{11}) = \frac{2 k_{z;k_{11}}}{(k_{z;k_{11}} + q_{z;k_{11}})} \quad (9)$$

In (3), V is volume of the metal and $\Psi_0(\underline{r})$, which is given by, (4) represents the extended electronic state of the unperturbed semi-infinite metal for the given energy E and wave vector \underline{k}_{11} . If we wish we can think of this state as being generated when the propagating plane wave $\frac{1}{V^{1/2}} \exp(i\underline{k}_{11}^+ \cdot \underline{r})$ with its source at $z = -\infty$ is incident on the surface barrier at $z = 0$ which does not incorporate the potential of the adsorbed atom. This incident wave will give rise to a «reflected» wave having amplitude $\frac{1}{V^{1/2}} R^{LL}(k_{11})$, and to a «transmitted» wave having amplitude $\frac{1}{V^{1/2}} T^{LR}(k_{11})$.

The reflected wave is represented by the second term in (4a) and $R^{LL}(k_{11})$ is given by (8). The transmitted wave determines the value of $\Psi_0(\underline{r})$ for $z > 0$ and it is given by the right hand side of (4b). $T^{LR}(k_{11})$ is given by (9).

The Local Density of States, $\rho(E, \underline{r})$, for the metal-atom system is given by the right hand side of (3) with $\Psi_0(\underline{r})$ replaced by $\Psi(\underline{r})$.

We have

$$\rho(E, \underline{r}) = \frac{V}{4\pi^3} \int \int_{|\underline{k}_{11}| < k_{11, \max}} d^2 k_{11} \left(\frac{\partial E}{\partial k_{z;k_{11}}} \right)^{-1} |\Psi(\underline{r})|^2, \quad E > V_0 \quad (10)$$

where $\Psi(\underline{r})$ is the wave function representing the electronic state of the metal-atom system which derives from the clean metal wave function $\Psi_0(\underline{r})$. In ref. 7 we gave the prescription of how one can construct $\Psi(\underline{r})$ starting from $\Psi_0(\underline{r})$. After some lengthy but straightforward algebra we obtain the following explicit expressions for $\Psi(\underline{r})$. We have

$$\Psi(\underline{r}) = \frac{1}{V^{1/2}} \exp(i\underline{k}_{11}^+ \cdot \underline{r}) + \frac{1}{V^{1/2}} R^{LL}(k_{11}) \exp(i\underline{k}_{11}^- \cdot \underline{r}) + \frac{1}{V^{1/2}} \int \int_{-\infty}^{-\infty} d^2 k'_{11} C_L^{EX}(\underline{k}_{11}, \underline{k}'_{11}) \exp(i\underline{k}'_{11}^- \cdot \underline{r}) \quad \text{for } z < 0. \quad (11a)$$

$$\Psi(\underline{r}) = \frac{1}{V^{1/2}} \exp(i\underline{q}_{11}^+ \cdot \underline{r}) + \frac{1}{V^{1/2}} \int \int_{-\infty}^{-\infty} d^2 k'_{11} B_L^{EX}(\underline{k}_{11}, \underline{k}'_{11}) \times \{ \exp(i\underline{q}'_{11}^- \cdot \underline{r}) + R^{RR}(k'_{11}) \exp(i\underline{q}'_{11}^+ \cdot \underline{r}) \} \quad (11b)$$

for $0 < z < Z_a$ and for $|\underline{r} - \underline{R}_a| > a_0$.

$$\Psi(\underline{r}) = \frac{1}{V^{1/2}} \exp(i\underline{q}_{11}^+ \cdot \underline{r}) + \frac{1}{V^{1/2}} \int \int_{-\infty}^{-\infty} d^2 k'_{11} \exp(i\underline{q}'_{11}^+ \cdot \underline{r}) \times \{ B_R^{EX}(\underline{k}_{11}, \underline{k}'_{11}) + B_L^{EX}(\underline{k}_{11}, \underline{k}'_{11}) R^{RR}(k'_{11}) \} \quad (11c)$$

for $z > Z_a$ and for $|\underline{r} - \underline{R}_a| > a_0$.

$$\psi(r) = \frac{1}{V^{\frac{1}{2}}} \sum_{\ell m} \sum_{\ell' m'} R_{\ell}(r_a) Y_{\ell m}(\hat{r}_a) \frac{[j_{\ell}(qa_0) + S_{\ell}^a(E) h_{\ell}^{(1)}(qa_0)]}{R_{\ell}(a_0)} \times \left[\frac{I}{\sim} - \frac{GS^a}{\sim} \right]_{\ell m; \ell' m'}^{-1} Q_{\ell' m'}(k_{11}) \quad (11d)$$

for $|r - R_a| < a_0$.

The coefficients $C_L^{Ex.}(k_{11}, k'_{11})$ appearing in (11a) are given by

$$C_L^{Ex.}(k_{11}, k'_{11}) = B_L^{Ex.}(k_{11}, k'_{11}) T^{RL}(k'_{11}) \quad (12)$$

where

$$B_L^{Ex.}(k_{11}, k'_{11}) = \frac{1}{2\pi q} \frac{1}{q_{z; k'_{11}}} \exp(iq_{z; k'_{11}} \cdot Z_a) \times \sum_{\ell m} \sum_{\ell' m'} (i)^{-\ell} Y_{\ell m}(\hat{q}_{k'_{11}}) S_{\ell}^a(E) \left[\frac{I}{\sim} - \frac{GS^a}{\sim} \right]_{\ell m; \ell' m'}^{-1} Q_{\ell' m'}(k_{11}) \quad (13)$$

$$T^{RL}(k'_{11}) = \frac{2q_{z; k'_{11}}}{(k_{z; k'_{11}} + q_{z; k'_{11}})} \quad (14)$$

$$q = \left(\frac{2m}{\hbar^2} E \right)^{\frac{1}{2}} \quad (15)$$

We note that in the present calculation we are concerned with negative energies; hence q in (15) is always imaginary. The matrix elements $Q_{\ell' m'}(k_{11})$ in (13) are given by

$$Q_{\ell' m'}(k_{11}) = 4\pi T^{LR}(k_{11}) \exp(iq_{z; k_{11}} \cdot Z_a) (i)^{\ell'} (-1)^{m'} Y_{\ell' -m'}(\hat{q}_{k_{11}}^+) \quad (16)$$

The quantity $R^{RR}(k_{11})$ under integral sign in (11b) and (11c) represents the amplitude of the wave «reflected» from the metal surface when a plane wave $\exp(iq_{z; k_{11}} \cdot r)$ incident on it from the right ($z > 0$). This is given by

$$R^{RR}(k_{11}) = \frac{(q_{z; k'_{11}} - k_{z; k'_{11}})}{(k_{z; k'_{11}} + q_{z; k'_{11}})} = -R^{LL}(k_{11}) \quad (17)$$

The amplitude $T^{RL}(k'_{11})$ of the corresponding wave which is transmitted inside the metal ($z < 0$) is given by (14). The coefficients $B_R^{Ex.}(k_{11}, k'_{11})$ in (11c) are given by

$$B_R^{Ex.}(k_{11}, k'_{11}) = \frac{1}{2\pi q} \frac{1}{q_{z; k'_{11}}} \exp(iq_{z; k'_{11}} \cdot Z_a) \times \sum_{\ell m} \sum_{\ell' m'} (i)^{-\ell} Y_{\ell m}(\hat{q}_{k'_{11}}^+) S_{\ell}^a(E) \left[\frac{I}{\sim} - \frac{GS^a}{\sim} \right]_{\ell m; \ell' m'}^{-1} Q_{\ell' m'}(k_{11}) \quad (18)$$

The matrix elements $S_{\ell}^a(E)$ are given by Eq. (7) in ref. 18. The matrix elements $G_{\ell m; \ell' m'}(E)$ are obtained from the following formula

$$G_{\ell m; \ell' m'}(E) = \frac{2(i)^{\ell-\ell'}}{q} \int_{-\infty}^{\infty} \int_{-\infty}^{\infty} d^2 k_{11} \{ Y_{\ell' m'}(\hat{q}_{k_{11}}^-) \exp(i 2 q_{z; k_{11}}' \cdot Z_a) \times \frac{1}{q_{z; k_{11}}} R^{RR}(k_{11}') (-1)^m Y_{\ell-m}(\hat{q}_{k_{11}}^+) \} \quad (19)$$

It is worth mentioning that matrix elements $G_{\ell m; \ell' m'}(E)$, given by (19), possess the following three properties

$$\begin{aligned} \text{(i)} \quad & G_{\ell m; \ell' m'}(E) = G_{\ell' m'; \ell m}(E) \\ \text{(ii)} \quad & G_{\ell m; \ell' m'}(E) = 0 \quad \text{for } m \neq m' \\ \text{(iii)} \quad & G_{\ell |m|; \ell' |m'|}(E) = G_{\ell' |m'|; \ell |m|}(E) \end{aligned} \quad (20)$$

We note that these properties reflect the cylindrical symmetry inherent in our model Hamiltonian as a direct consequence of using equation (2) to represent the potential field one electron sees in the metal adatom system. The importance of these properties in relation to some of our numerical results will become apparent at a later stage.

We calculated the LDS of the metal-adatom system $\rho(E, \underline{r})$, given by (10), within a sphere centered on the adsorbed atom and with radius approximately 3 times the radius a_0 of the adatom sphere. We verified that the total charge within this sphere is the same with the atom adsorbed on the surface as it is without the adatom. We found that outside this sphere the difference between $\rho(E, \underline{r})$, and the corresponding quantity $\rho_M(E, \underline{r})$ for the clean metal, given by (3), is negligibly small.

In the case of Ne highest occupied states (2p) of the isolated atom have energy $E_{2p} = -13.205$ eV and hence lie below the bottom of the conduction band of the metal ($V_0 = -13$ eV). In this case on adsorption the three-fold degenerate (apart from spin) atomic level splits into two levels. A non-degenerate (apart from spin) level at $E_0 = -13.214$ eV derives from the $(\ell, m) = (1, 0)$ atomic state, and a doubly degenerate (apart from spin) level at $E_{\pm 1} = -13.214$ eV derives from the $(\ell, m) = (1, \pm 1)$ atomic states. The wave function representing the electronic state of the metal-Neon system, which has energy E_0 and is characterized by the magnetic quantum number $m=0$, will be denoted by $\psi_0(\underline{r})$. Similar the wave functions describing the electronic states with energy $E_{\pm 1}$ are denoted by $\psi_{\pm 1}(\underline{r})$. The wave function $\psi_{+1}(\underline{r})$ describes the state which is characterized by the magnetic quantum number $m=+1$, and $\psi_{-1}(\underline{r})$ describes that state for which $m=-1$. We recall that in ref. 7 we derived the condition for the existence of localized states for the model potential field referred to here in. Furthermore we obtained there an expression for the wave function representing such a localized state for $|\underline{r}-\underline{R}_a| > a_0$ and $z > 0$. For the model potential field described by (2) we shall write down explicit expressions for $\psi_0(\underline{r})$ covering all regions of space as follows:

$$\psi_0(\underline{r}) = \int_{-\infty}^{+\infty} \int_{-\infty}^{+\infty} d^2 k_{11} C_L^{Loc.}(k_{11}', m=0) \exp(i \underline{k}_{k_{11}}^- \cdot \underline{r}) \quad \text{for } z < 0 \quad (21a)$$

$$\psi_0(\underline{r}) = \int_{-\infty}^{+\infty} \int_{-\infty}^{+\infty} d^2 k_{11} B_L^{Loc.}(k_{11}', m=0) \{ \exp(i \underline{q}_{k_{11}}^- \cdot \underline{r}) + R^{RR}(k_{11}') \exp(i \underline{q}_{k_{11}}^+ \cdot \underline{r}) \} \quad (21b)$$

for $0 < z < Z_a$ and for $|\underline{r}-\underline{R}_a| > a_0$.

$$\psi_0(\underline{r}) = \int_{-\infty}^{+\infty} \int_{-\infty}^{+\infty} d^2k_{11}' \exp(iq_{z;k_{11}'} \cdot \underline{r}) \{B_R^{Loc.}(k_{11}', m=0) + B_L^{Loc.}(k_{11}', m=0) R^{RR}(k_{11}')\} \quad (21c)$$

for $z > Z_a$ and for $|\underline{r}-\underline{R}_a| > a_0$.

$$\psi_0(\underline{r}) = \sum_{\ell m} R_\ell(r_a) Y_{\ell m}(\hat{r}_a) \left[\frac{1}{S_\ell^a(E)} j_\ell(qa_0) + h_\ell^{(1)}(qa_0) \right] \frac{A_{\ell m} \delta_{m0}}{R_\ell(a_0)} \quad (21d)$$

for $|\underline{r}-\underline{R}_a| < a_0$.

The coefficients $C_L^{Loc.}(k_{11}', m=0)$ appearing in (21a) are given by

$$C_L^{Loc.}(k_{11}', m=0) = B_L^{Loc.}(k_{11}', m=0) T^{RL}(k_{11}') \quad (22)$$

where

$$B_L^{Loc.}(k_{11}', m=0) = \frac{1}{2\pi q} \frac{1}{q_{z;k_{11}'}} \exp(iq_{z;k_{11}'} \cdot Z_a) \times \sum_{\ell m} (i)^{-\ell} Y_{\ell m}(\hat{q}_{k_{11}'}) A_{\ell m} \delta_{m0} \quad (23)$$

The coefficients $B_R^{Loc.}(k_{11}', m=0)$ in (21c) are given by

$$B_R^{Loc.}(k_{11}', m=0) = \frac{1}{2\pi q} \frac{1}{q_{z;k_{11}'}} \exp(-iq_{z;k_{11}'} \cdot Z_a) \sum_{\ell m} (i)^{-\ell} Y_{\ell m}(\hat{q}_{k_{11}'}) A_{\ell m} \delta_{m0} \quad (24)$$

The matrix elements $A_{\ell m} \delta_{m0} \equiv A_{\ell 0}$, which appear in (21d), (23) and (24), are obtained by solving the following system of equations

$$\begin{bmatrix} S^a & -G \\ \sim & \sim \end{bmatrix}_{\ell 0; \ell' 0} A_{\ell' 0} = 0, \quad \ell \geq 0 \quad (25)$$

For $E = E_0$, (25) has a non-trivial solution and thus we can evaluate $A_{\ell 0}$ subject to the condition

$$\int_{-\infty}^{+\infty} |\psi_0(\underline{r})|^2 d^3r = 1.$$

Once we have written down expressions for $\psi_0(\underline{r})$ it is not difficult to deduce expressions for $\psi_{+1}(\underline{r})$ and $\psi_{-1}(\underline{r})$. This can be done as follows:

(i) The wave functions $\psi_{\pm 1}(\underline{r})$ for $0 < z < Z_a$ and $|\underline{r}-\underline{R}_a| > a_0$ will be given by (21b) with the coefficients $B_L^{Loc.}(k_{11}', m=0)$ replaced by the new coefficients $B_L^{Loc.}(k_{11}', m = \pm 1)$. The latter coefficients

are given by (23) with $A_{\ell m} \delta_{m0}$ replaced by $A_{\ell m} \delta_{m, \pm 1}$. The matrix elements $A_{\ell m} \delta_{m, \pm 1} \equiv A_{\ell, \pm 1}$ are

obtained by solving the two independent systems of equations.

$$\begin{bmatrix} S^a & -G \\ \sim & \sim \end{bmatrix}_{\ell, \pm 1; \ell', \pm 1} A_{\ell', \pm 1} = 0, \quad \ell \geq 1 \quad (26)$$

which have a non-trivial solution for $E = E_{\pm 1}$. Furthermore the values of $A_{\ell, \pm 1}$ are subject to the condition

$$\int_{-\infty}^{+\infty} |\psi_{\pm 1}(\underline{r})|^2 d^3r = 1 \quad .$$

(ii) The wave functions $\psi_{\pm 1}(\underline{r})$ for $z < 0$, i.e. inside the metal, will be given by (21a) with the coefficients $C_L^{\text{Loc.}}(k_{11}, m=0)$ replaced by the new coefficients $C_L^{\text{Loc.}}(k'_{11}, m = \pm 1)$ where

$$C_L^{\text{Loc.}}(k'_{11}, m = \pm 1) = B_L^{\text{Loc.}}(k'_{11}, m = \pm 1) T^{\text{RL}}(k'_{11})$$

and $B_L^{\text{Loc.}}(k'_{11}, m = \pm 1)$ are determined as prescribed above.

(iii) $\psi_{\pm 1}(\underline{r})$ for $z > Z_a$ and for $|r - R_a| > a_0$ will be given by (21c) with $B_L^{\text{Loc.}}(k'_{11}, m=0)$ replaced by $B_L^{\text{Loc.}}(k'_{11}, m = \pm 1)$, and with $B_R^{\text{Loc.}}(k'_{11}, m=0)$ replaced by $B_R^{\text{Loc.}}(k'_{11}, m = \pm 1)$. The latter coefficients are given by (24) with $A_{\ell m} \delta_{m0}$ replaced by $A_{\ell m} \delta_{m, \pm 1} \equiv A_{\ell, \pm 1}$.

(iv) $\psi_{\pm 1}(\underline{r})$ for $|r - R_a| < a_0$, i.e. within the muffin-tin sphere of the adsorbed atom, will be given by (21d) with $A_{\ell m} \delta_{m0}$ replaced by $A_{\ell m} \delta_{m, \pm 1}$.

It is appropriate at this point to investigate why the energy level $E_{\pm 1}$ is degenerate. By virtue of (20), which describes the properties of the matrix elements $G_{\ell m; \ell' m'}(E)$, and because $S^a \equiv S_{\ell}^a(E) \delta_{\ell \ell'} \delta_{mm'}$ is a diagonal matrix we have

$$\left[S^a{}^{-1} - G \right]_{\ell, +1; \ell', +1} = \left[S^a{}^{-1} - G \right]_{\ell, -1; \ell', -1} \quad (27)$$

It is apparent now that, in view of (27), the two independent systems of equations, given by (26) will always have non-trivial solutions for the **same** energy. Hence the degeneracy of the $E_{\pm 1}$ energy level.

In Fig. 1 (a) we show contours of constant $|\psi_0(\underline{r})|^2$ in (any) plane normal to the metal surface containing the Neon nucleus. The corresponding «isometric projection» is shown in Fig. 1 (b). It is obvious from these figures that the wave function $\psi_0(\underline{r})$ remains highly localized on the Neon atom, although it is distorted giving rise to a small negative polarization (the electric dipole points away from the metal). Furthermore these figures clearly demonstrate that the $(l, m) = (1, 0)$ atomic state is the primary source of the localized state represented by $\psi_0(\underline{r})$.

In Fig. 2 (a) we show contours of constant $|\psi_{\pm 1}(\underline{r})|^2$ with the corresponding isometric projection being shown in Fig. 2 (b). We note that $|\psi_{+1}(\underline{r})|^2 = |\psi_{-1}(\underline{r})|^2$. The fact that $\psi_{+1}(\underline{r})$ and $\psi_{-1}(\underline{r})$ describe localized states which derive from the $(l, m) = (1, +1)$ and $(l, m) = (1, -1)$ atomic states respectively is clearly seen from Fig. 2. We also observe that $\psi_{\pm 1}(\underline{r})$ are highly localized on the Neon atom and slightly distorted, although this distortion is not so apparent from the contour plot in Fig. 2 (a). The resulting negative polarization for these states is practically negligible in comparison with the polarization associated with the wave function $\psi_0(\underline{r})$.

From Fig. 1 and Fig. 2 one can visualize why we found the energy level E_0 , which is associated with $\psi_0(\underline{r})$, to lie below the $E_{\pm 1}$ energy level which, in turn, is associated with the wave functions $\psi_{\pm 1}(\underline{r})$. This can be attributed to the fact that the electronic cloud associated with the $(1, 0)$ atomic state «sees» more of the clean metal potential field for $z < 0$. In contrast, this is not the case for the wave functions representing the $(1, \pm 1)$ atomic states which because of

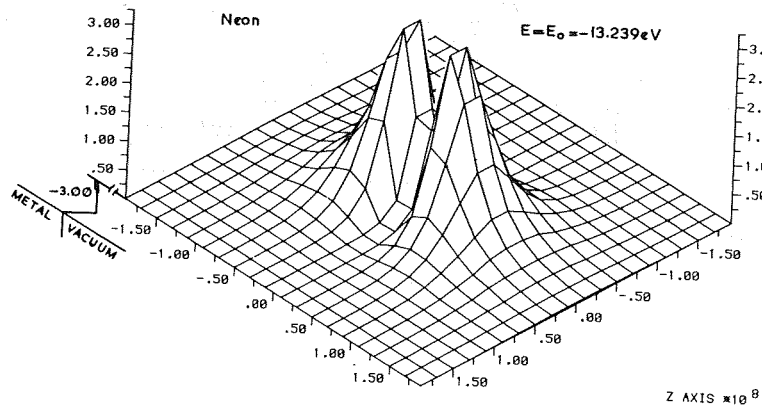


Fig. 1 : (b)
Isometric projection of $|\psi_0(r)|^2$ corresponding to the contour map in Fig. 2-1(a).

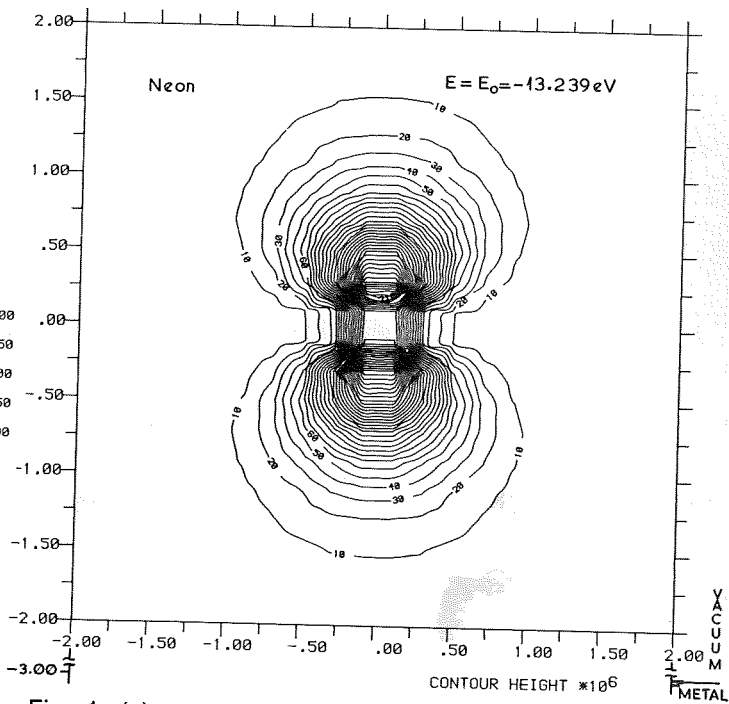


Fig. 1 : (a)

Contours of $|\psi_0(r)|^2$ for Ne on jellium substrate. $\psi_0(r)$ is the electronic wave function localized on the Ne adatom, defined by (21), which is characterized by the magnetic quantum number $m = 0$. Here

$$\int d^3r |\psi_0(r)|^2 \neq 1.$$

Because of the existing cylindrical symmetry we get identical contours on any plane normal to the metal surface (indicated by arrow) containing the Ne nucleus. Here the origin of coordinates has been shifted to coincide with the Ne nucleus. Distances are measured in a.u.

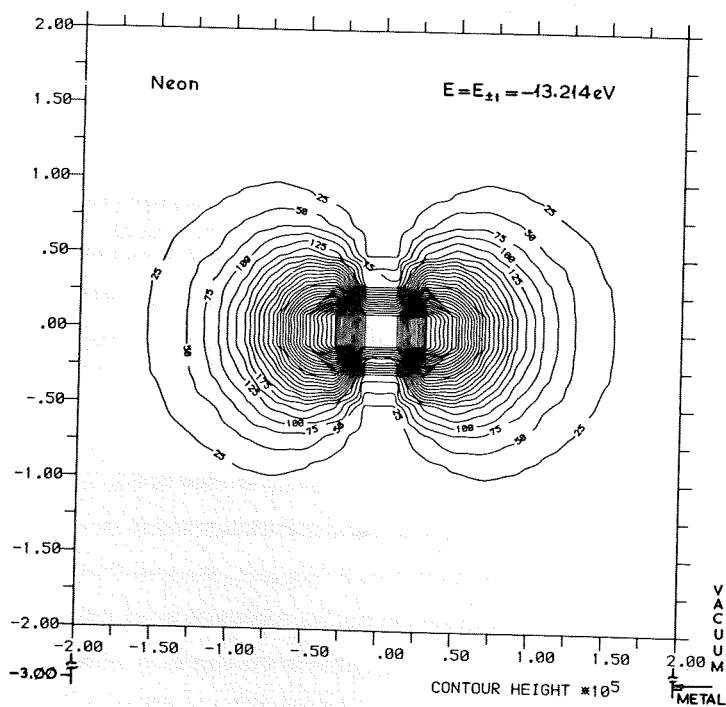


Fig. 2 : (a)

Contours of $|\psi_{+1}(r)|^2 = |\psi_{-1}(r)|^2$ for Ne on jellium substrate. [See caption of Fig. 1 (a) for details of such contours]. $\psi_{+1}(r)$ and $\psi_{-1}(r)$ are the electronic wave functions localized on the Ne adatom, which are characterized by the magnetic quantum number $m = +1$ and $m = -1$ respectively. They are obtained from (21) in the manner described in the text. Here $\int d^3r |\psi_{\pm 1}(r)|^2 \neq 1$.

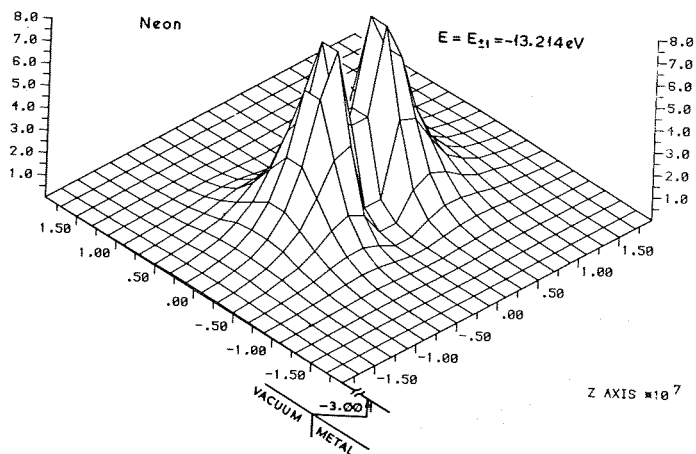


Fig. 2 : (b)

Isometric projection of $|\psi_{+1}(r)|^2 = |\psi_{-1}(r)|^2$ corresponding to the contour map in Fig. 2 (a).

the nature of their spatial distribution, hardly «see» this potential field. Hence one should be able by resolving to first-order perturbation theory to confirm the expectation of the result that $E_0 < E_{\pm 1}$.

In the case of Ar and Kr the valence atomic states have energies $E_{3p} = -9.791$ eV and $E_{4p} = -8.608$ eV respectively, and hence lie opposite the conduction band of the metal. When the atom approaches the metal these states turn into resonances of a definite width in energy. These resonances are clearly demonstrated in Fig. 3. The «Atomic Density of States», $\rho_{ADS}(E)$, shown in this figure is defined by

$$\rho_{ADS}(E) = \int_{|\underline{r}-\underline{R}_a| \leq a_0} \rho(E, \underline{r}) d^3r \quad (28)$$

where $\rho(E, \underline{r})$ is given by (10) with $\psi(\underline{r})$ in the same equation given by (11d), and the integration is over the volume of the muffin-tin sphere of the adsorbed atom. The quantity defined by (28) has all the essential features of an atomic resonance. A more explicit expression for $\rho_{ADS}(E)$ is derived in Appendix 1 where we show the close dependence of this quantity on the average density of states of the clean metal defined by (A1.6).

We note that $\rho_{ADS}(E)dE$ represents the number of electrons within the adatom sphere with energy between E and $E+dE$. We should point out that the resonances for Ar and Kr shown in Fig. 3 occur well below the Fermi level ($E_F \approx -4.5$ eV), and this explains why they have not been observed in Field-Emission Energy Distributions¹⁷.

The induced dipole moment per adsorbed atom is given by $\mu(E_F)$ where

$$\mu(E) = \mu_A + \mu_M(E) \quad (29)$$

where μ_A is given by

$$\mu_A = 2 \sum_{m=-1}^1 \int e |\psi_m(\underline{r})|^2 (z-Z_a) d^3r \quad (30a)$$

for Neon, and

$$\mu_A(E) = \int_{E_{res,peak}-\Gamma}^{E_{res,peak}+\Gamma} \theta(E-E') \rho(E') dE' \quad (30b)$$

for Argon and Krypton.

$$\theta(t) = 1 \text{ for } t > 0 \text{ and } \theta(t) = 0 \text{ for } t < 0.$$

$E_{res,peak}$ denotes the position of the resonance peak in $\rho_{ADS}(E)$, and Γ is determined by the requirement that

$$\int_{E_{res,peak}-\Gamma}^{E_{res,peak}+\Gamma} \rho_{ADS}(E) dE = \text{number of valence electrons in the free atom sphere.} \quad (31)$$

$\psi_m(\underline{r})$ in (30a) represents the electronic wave function localized on the Ne adatom, which is characterized by the magnetum quantum number m see e.g. (21) and comments thereafter, e is the electronic charge and the factor 2 accounts for spin degeneracy. The second term in (29) is given by

$$\mu_M(E) = \int_{V_0}^E \rho(E) dE \quad (32a)$$

for Ne, and

$$\mu_M(E) = \int_{V_0}^{E_{res,peak}-\Gamma} \theta(E-E') \rho(E') dE' + \int_{E_{res,peak}+\Gamma}^E \theta(E-E') \rho(E') dE' \quad (32b)$$

for Ar and Kr.

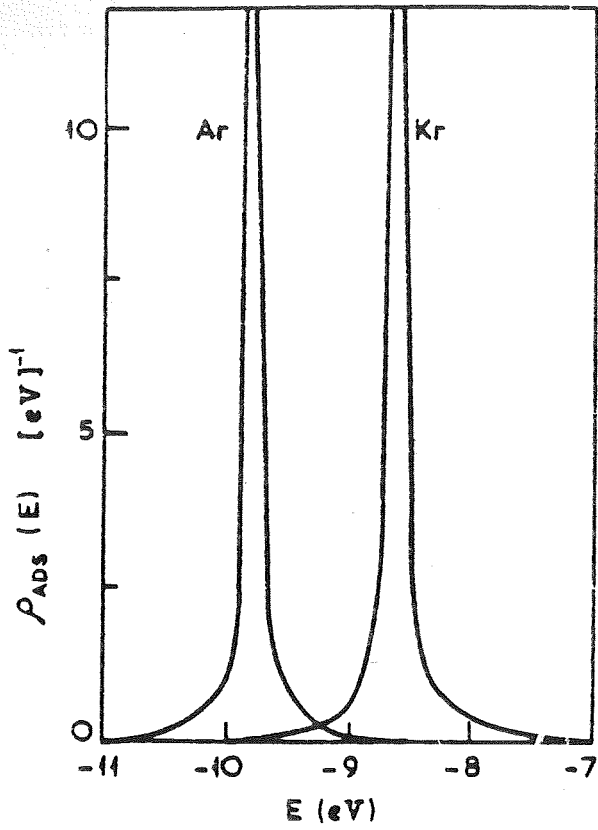


Fig. 3 : Atomic Density of States, $\rho_{\text{ADS}}(E)$, upon adsorption of Ar and Kr on jellium substrate.

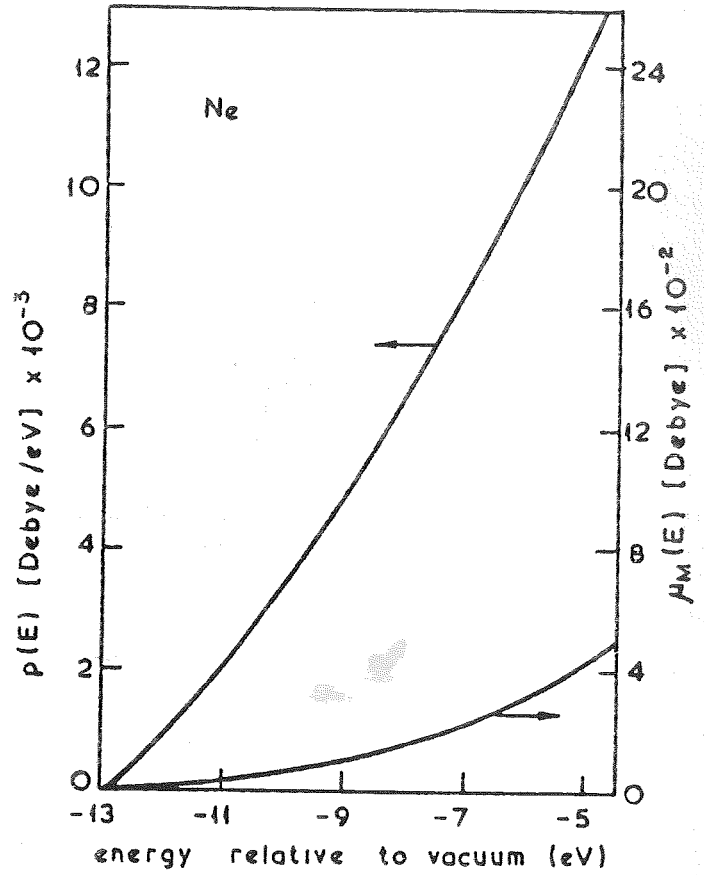


Fig. 4 : $\mu_M(E)$ and $p(E)$ as defined by Eqs. (32a) and (33) respectively for Ne on jellium substrate.

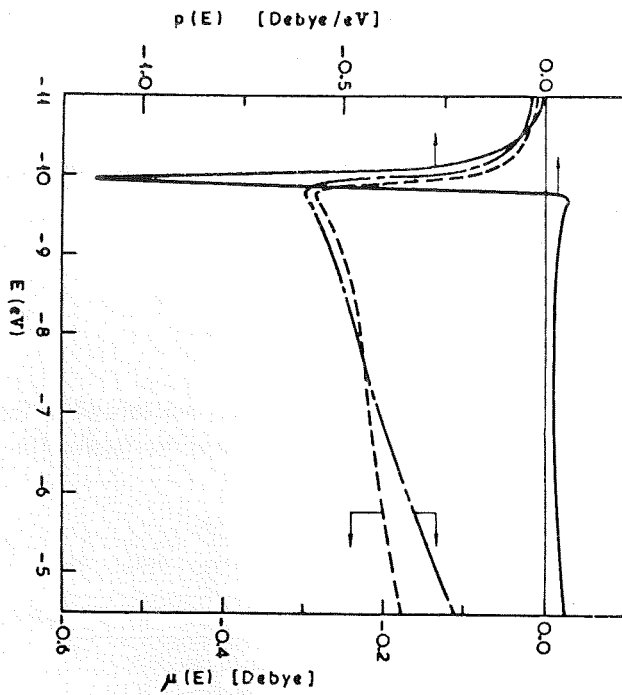


Fig. 5 :

Solid line: $\mu(E)$ and $p(E)$ as defined by Eqs. (29) and (33) respectively for Ar on jellium substrate. Broken curve: semi-empirical $\mu(E)$ for Ar on tungsten.

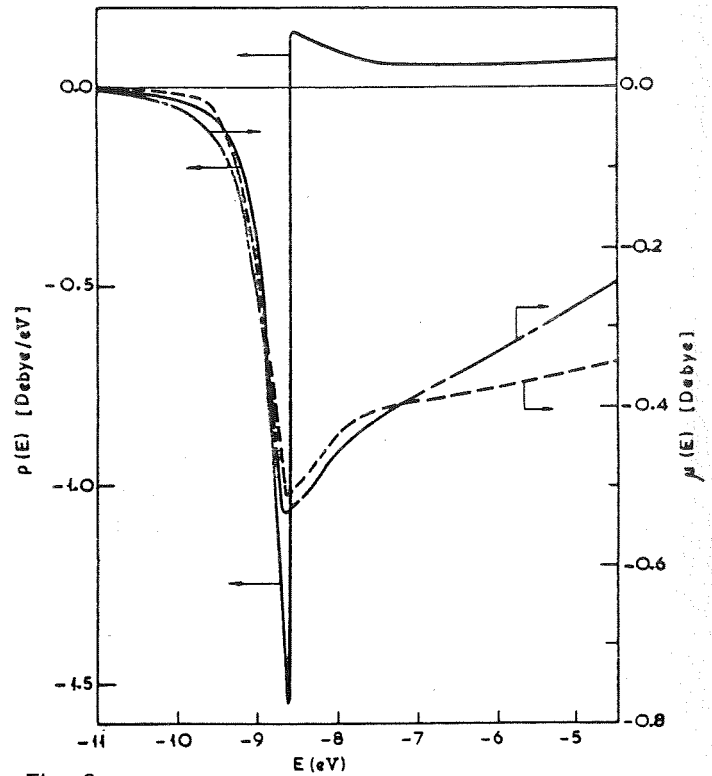


Fig. 6 :

Solid line: $\mu(E)$ and $p(E)$ as defined by Eqs. (29) and (33) respectively for Kr on jellium substrate. Broken curve: semi-empirical $\mu(E)$ for Kr on tungsten.

We note that the contribution to the induced dipole moment from the first term in (32b) is very small for both Ar and Kr. The polarization $p(E)$ is calculated numerically from the following formula:

$$p(E) = \int e(z-Z_a) [\rho(E, \underline{r}) - \rho_M(E, \underline{r})] d^3r \quad (33)$$

where $\rho(E, \underline{r})$ is given by (10) and $\rho_M(E, \underline{r})$ is obtained from (3). The calculated $p(E)$ and $\mu_M(E)$ for Ar and Kr are shown in Fig. 5 and Fig. 6 respectively. If we take the Fermi level $E_F = -4.5$ eV, we find the following values for the dipole moment (in Debyes) per adsorbed atom.

$$\text{Ne: } \mu(E_F) = -0.039, \quad \text{Ar: } \mu(E_F) = -0.105, \quad \text{Kr: } \mu(E_F) = -0.25 \quad (34)$$

Assuming a density of adsorbed atoms at monolayer coverage equal to one half of the maximum coverage estimated by Engel and Gomer¹¹ for adsorption on tungsten i.e. 3.95×10^{14} adsorbed atoms/cm² for Ne and Ar, and 3.6×10^{14} adsorbed atoms/cm² for Kr, we obtain a **reduction** of the work function at monolayer coverage as follows:

$$\text{Ne: } \Delta\phi = 0.058 \text{ eV}, \quad \text{Ar: } \Delta\phi = 0.155 \text{ eV}, \quad \text{Kr: } \Delta\phi = 0.338 \text{ eV} \quad (35)$$

Note that the calculated reduction in the work function increases from Ne to Kr in agreement with the experimental results⁹⁻¹¹, but the magnitude of this reduction is smaller than the one observed for tungsten (Table 2) and for the transition metals in Table 1. On the other hand the calculated values are comparable to the observed values of $\Delta\Phi$ in the case of Se, Zn, and Hg (shown in Table 1) for which a jellium model would seem more appropriate.

It is seen from Figs. 5 and 6 that the negative contribution to the dipole moment as defined by (29), (30b) and (32b) comes from the energies below $E_{\text{res.peak}}$ (the resonance peak, which in turn coincides with the unperturbed atomic level). At $E = E_{\text{res.peak}}$ the polarization changes sign. The contribution to the induced dipole moment denoted by μ_A is basically due to the polarization of the electronic charge associated with the p-states of the adsorbed atom. For the case of Ar this is exhibited in Figs. 7 to 9 where the contour plots and the corresponding isometric projections of $\rho(E, \underline{r})$ and $[\rho(E, \underline{r}) - \rho_M(E, \underline{r})]$ are shown for three values of E such that $E_{\text{res.peak}} - \Gamma < E < E_{\text{res.peak}} + \Gamma$

We note that we obtained similar plots for Kr. The modified distribution is mostly confined within the adatom sphere, hence we expect that it will not depend critically on the nature of the metal surface. On the other hand $p(E)$ for $E < E_{\text{res.peak}} - \Gamma$ and for $E > E_{\text{res.peak}} + \Gamma$, and hence $\mu_M(E)$, depends critically on the spread of electronic charge from the metal into the vacuum. The contour plots and the corresponding isometric projections of $\rho(E, \underline{r})$ and $[\rho(E, \underline{r}) - \rho_M(E, \underline{r})]$ for a value of $E < E_{\text{res.peak}} - \Gamma$, and for a value of $E > E_{\text{res.peak}} + \Gamma$ are shown in Figs. 10 and 11 respectively. One can show that for $E < E_{\text{res.peak}} - \Gamma$ and for $E > E_{\text{res.peak}} + \Gamma$ the electronic charge within the adatom sphere associated with energy E and hence $p(E)$ is strongly dependent on the average density of states

$\langle \rho_M(E, z=Z_a) \rangle$ of the unperturbed semi-infinite crystal defined by

$$\langle \rho_M(E, z=Z_a) \rangle \equiv \frac{1}{A} \int_A \rho_M(E, \underline{r}_{11}, z=Z_a) d^2r_{11} \quad (36)$$

where A denotes the area of a surface unit cell.

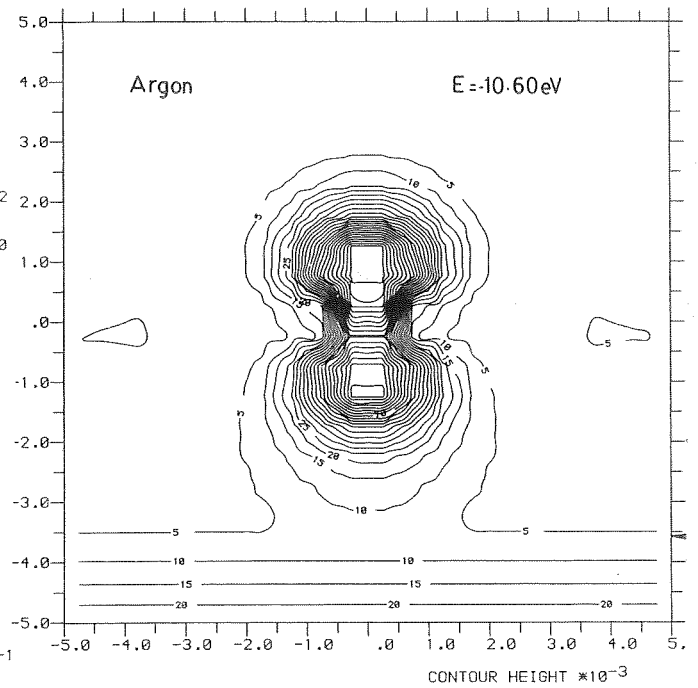
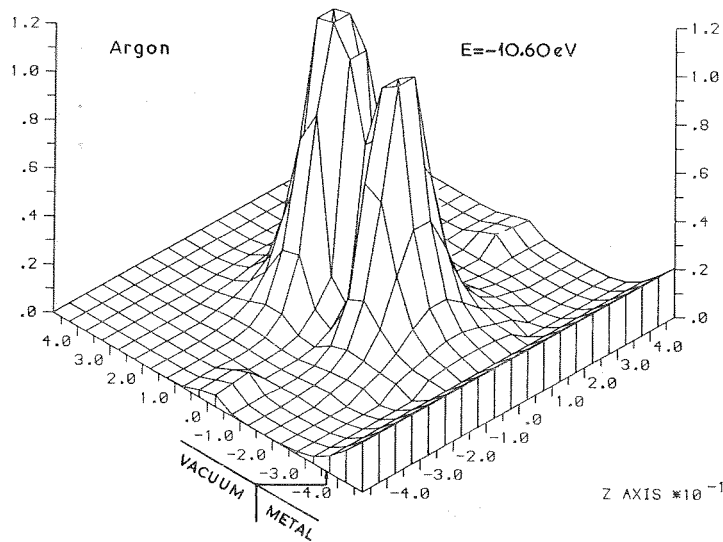


Fig. 7 : (a)

Fig. 7 : (b)

Isometric projection of $\rho(E, r)$ corresponding to the contour map in Fig. 7 (a).

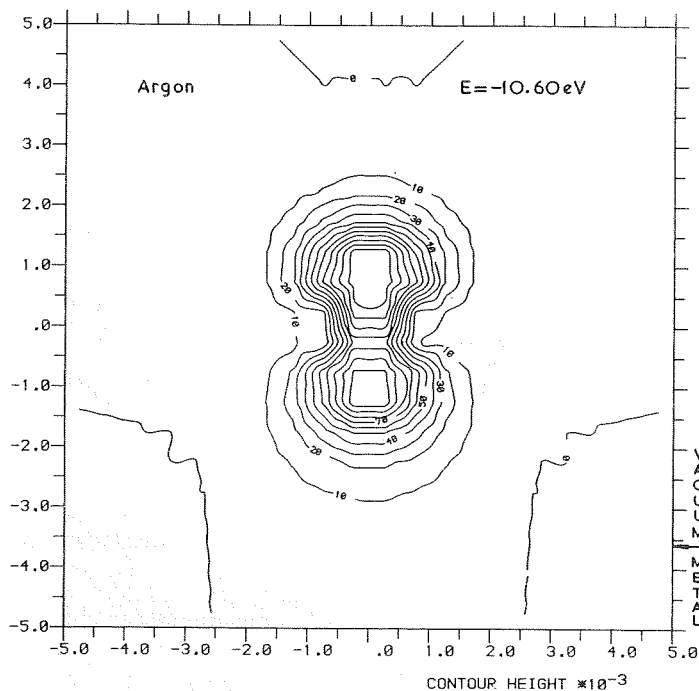


Fig. 7 : (c)

Contour plot of $[\rho(E, r) - \rho_M(E, r)]$ for an energy value **below** the resonance peak such that $E_{\text{res. peak}} - \Gamma < E < E_{\text{res. peak}}$. Because of the existing cylindrical symmetry we get identical contours on any plane normal to the metal surface (indicated by an arrow) containing the Ar nucleus. Here origin of coordinates has been shifted to coincide with the Ar nucleus. Distances are measured in a.u. and $[\rho(E, r) - \rho_M(E, r)]$ is given in (Hartrees)⁻¹

Contour plot of $\rho(E, r)$ for Ar on helium substrate for an energy value **below** the resonance peak such that $E_{\text{res. peak}} - \Gamma < E < E_{\text{res. peak}}$. Because of the existing cylindrical symmetry we get identical contours on any plane normal to the metal surface (indicated by an arrow containing the Ar nucleus. Here the origin of co-ordinates has been shifted to coincide with the Ar nucleus. Distances are measured in a.u. and $\rho(E, r)$ is given in (Hartrees)⁻¹.

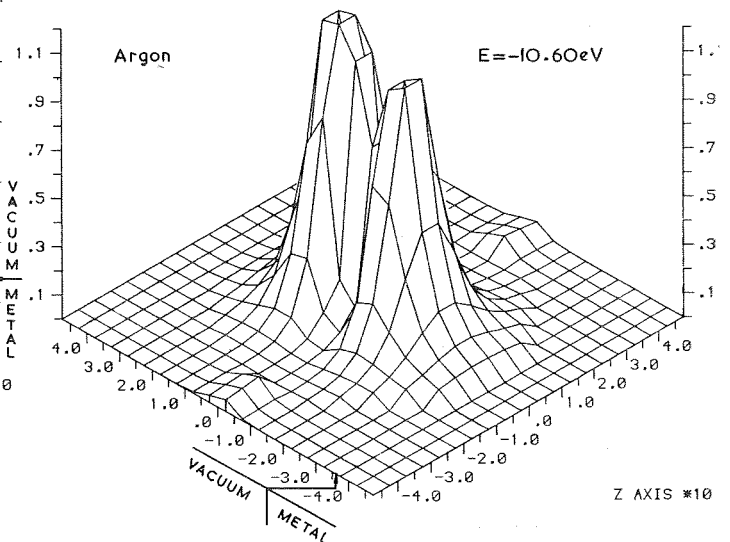


Fig. 7 (d)

Isometric projection of $[\rho(E, r) - \rho_M(E, r)]$ corresponding to the contour map in Fig. 7 (c).

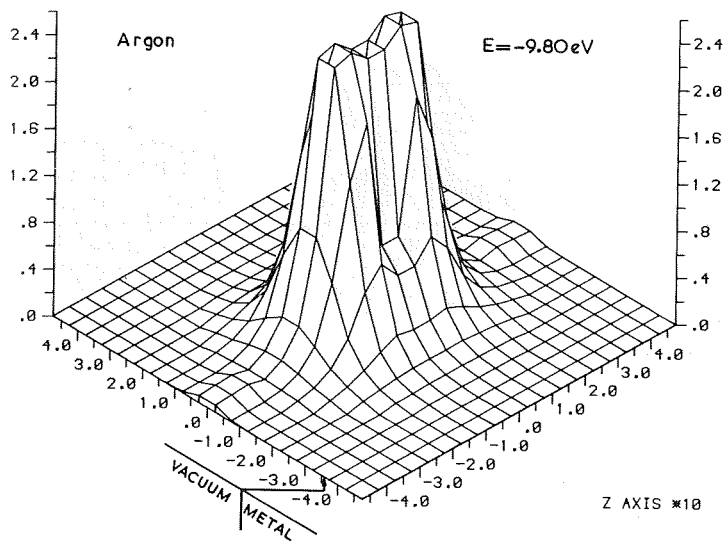


Fig. 8: (b)

Isometric projection of $q(E,r)$ corresponding to the contour map in Fig. 8(a).

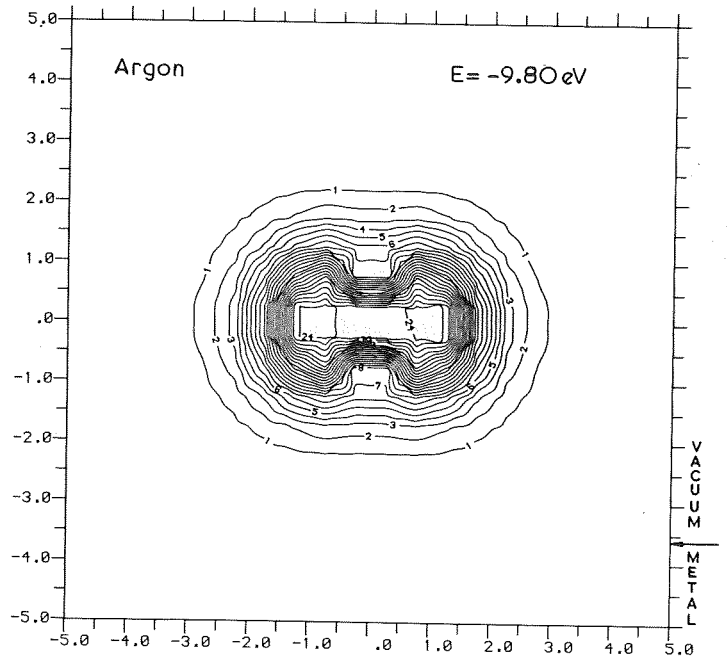


Fig. 8: (a)

Contour plot of $q(E,r)$ for Ar on jellium substrate for an energy value at the resonance peak, $E \approx E_{\text{res. peak}}$. [See caption of Fig. 7 (a) for details of such contours.]

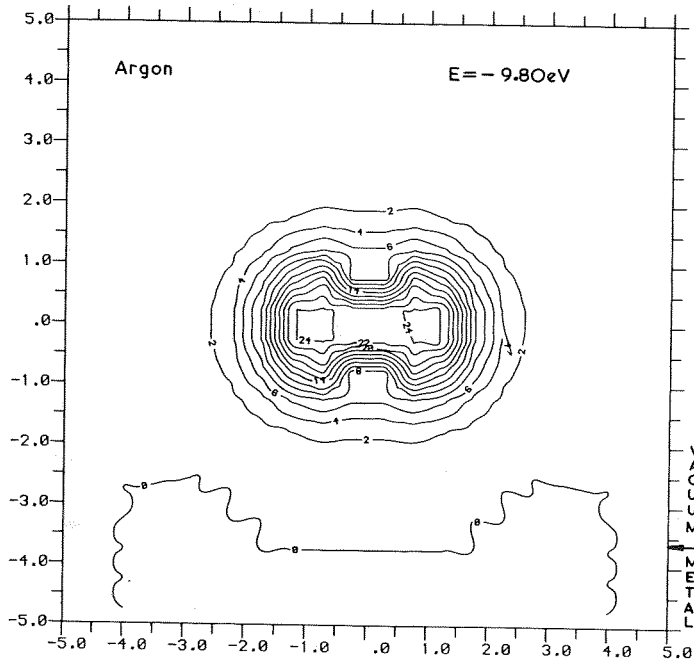


Fig. 8: (c)

Contour plot of $[q(E,r) - \rho_M(E,r)]$ for Ar on jellium substrate for an energy value at the resonance peak, $E \approx E_{\text{res. peak}}$. [See caption of Fig. 7 (c) for details of such contours.]

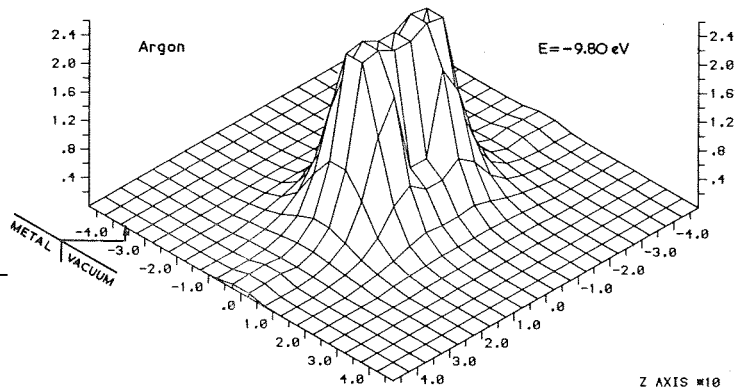


Fig 8:(d)

Isometric projection of $[q(E,r) - \rho_M(E,r)]$ corresponding to contour map in Fig. 8 (c).

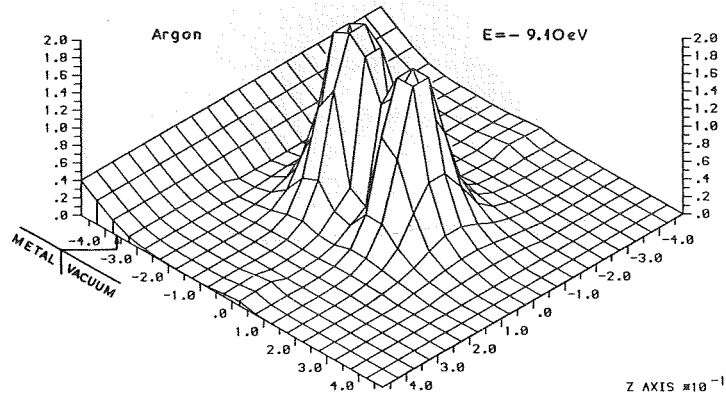


Fig. 9: (b)

Isometric projection of $\phi(E, r)$ corresponding to the contour map in Fig. 9 (a).

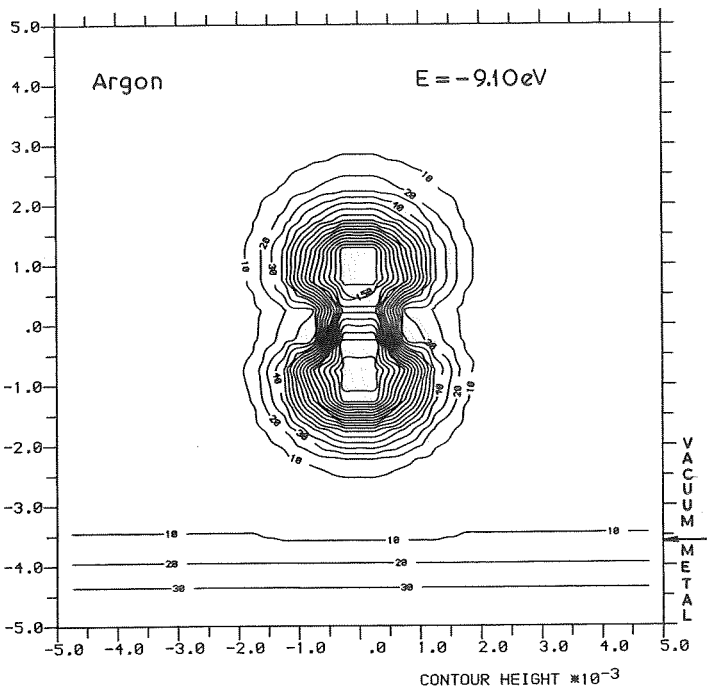


Fig. 9: (a)

Contour plot of $\phi(E, r)$ for Ar on jellium substrate for an energy value above the resonance peak such that $E_{\text{res. peak}} < E < E_{\text{res. peak}} + \Gamma$. See caption of Fig. 7 (a) for details of such contours.

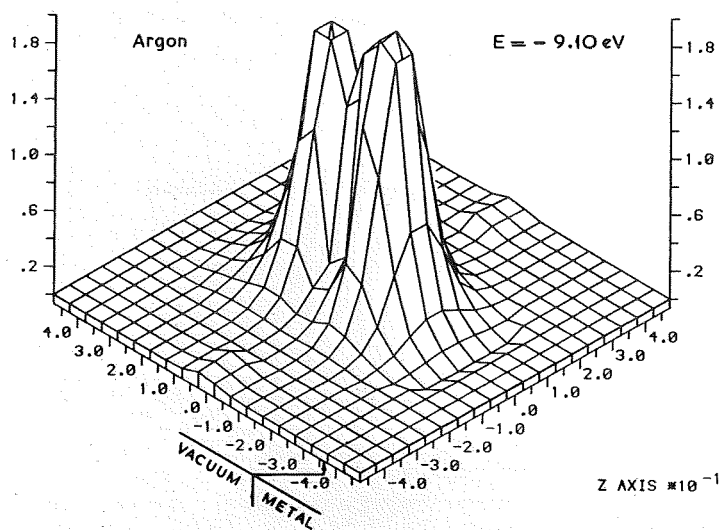


Fig. 9: (d)

Isometric projection of $[\phi(E, r) - \phi_M(E, r)]$ corresponding to the contour map in Fig. 9 (c).

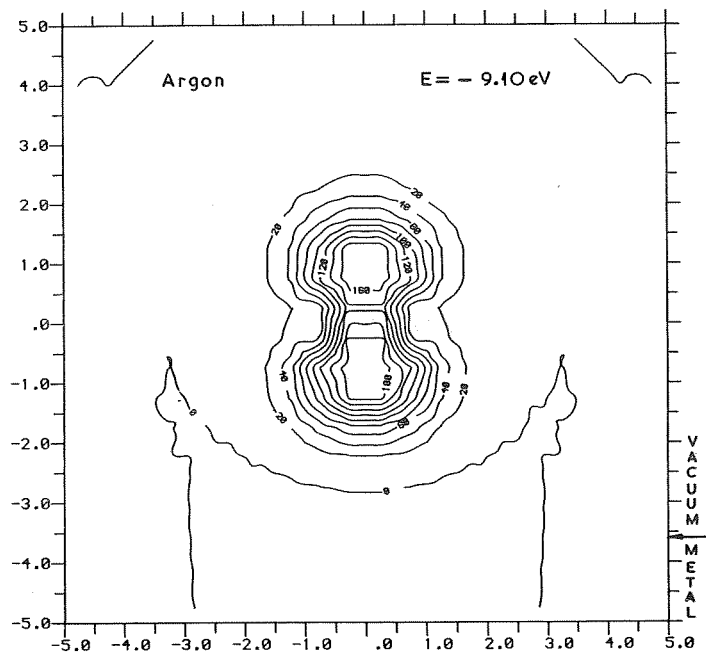


Fig. 9: (c)

Contour plot of $[\phi(E, r) - \phi_M(E, r)]$ for Ar on jellium substrate for an energy value above the resonance peak such that $E_{\text{res. peak}} < E < E_{\text{res. peak}} + \Gamma$. [See caption of Fig. 7 (c) for details of such contours.]

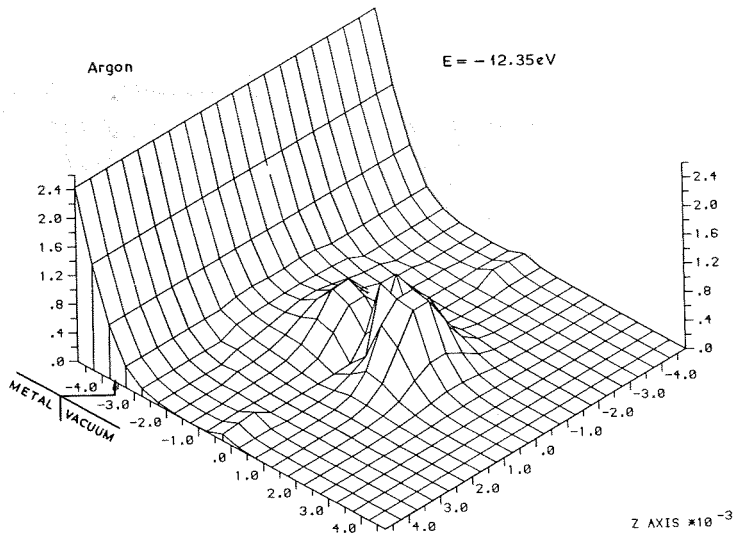


Fig. 10: (b)

Isometric projection of $\rho(E, \underline{r})$ corresponding to contour map in Fig. 10 (a).

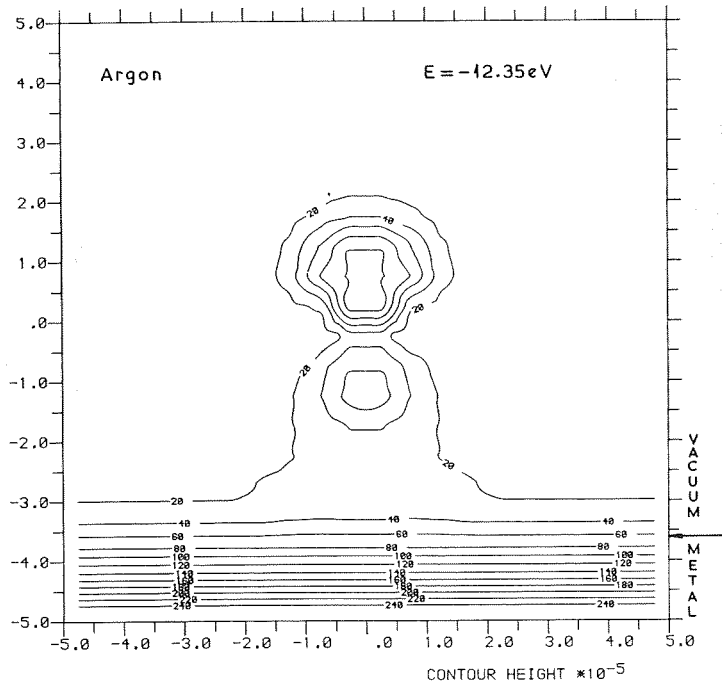


Fig. 10: (a)

Contour plot of $\rho(E, \underline{r})$ for Ar on jellium substrate for an energy value such that $E < E_{\text{ves. peak}} - \Gamma$. (See caption of Fig. 7 (a) for details of such contours.)

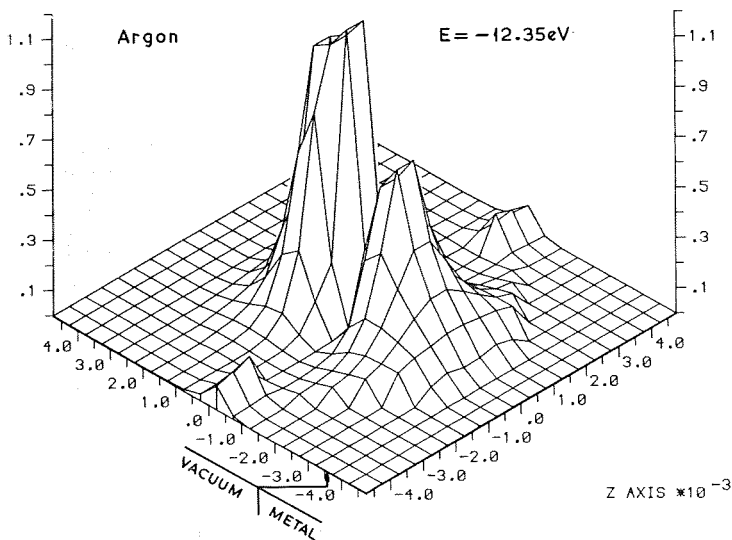


Fig. 10: (d)

Isometric projection of $[\rho(E, \underline{r}) - \rho_M(E, \underline{r})]$ corresponding to the contour map in Fig. 10 (c).

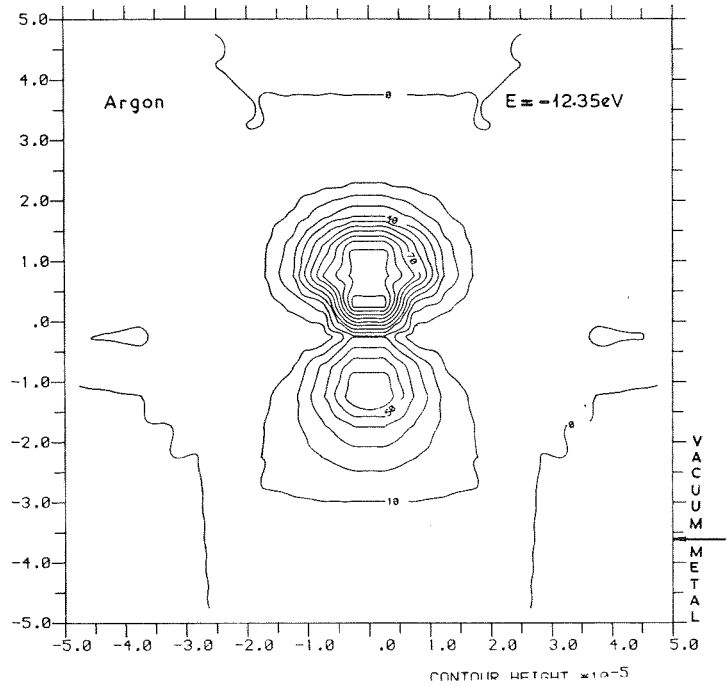


Fig. 10: (c)

Contour plot for $[\rho(E, \underline{r}) - \rho_M(E, \underline{r})]$ for Ar on jellium substrate for an energy value such that $E < E_{\text{ves. peak}} - \Gamma$. [See caption of Fig. 7 (c) for details of such contours.]

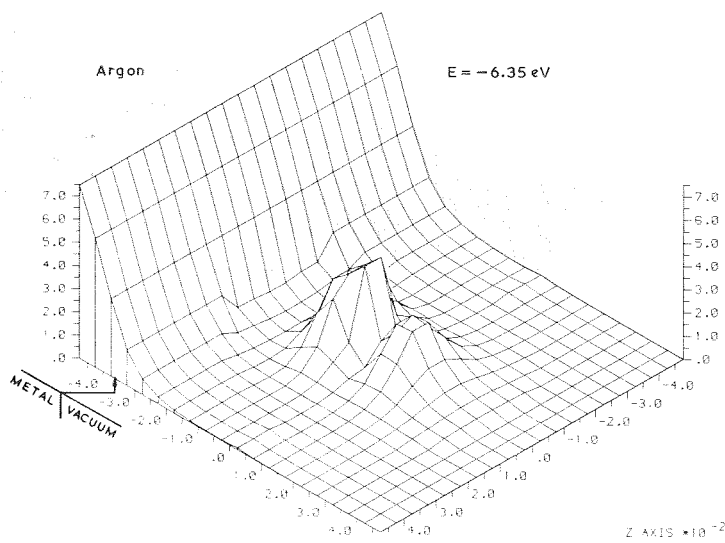


Fig. 11: (b)

Isometric projection of $\epsilon(E, r)$ corresponding to the contour map in Fig. 11(a).

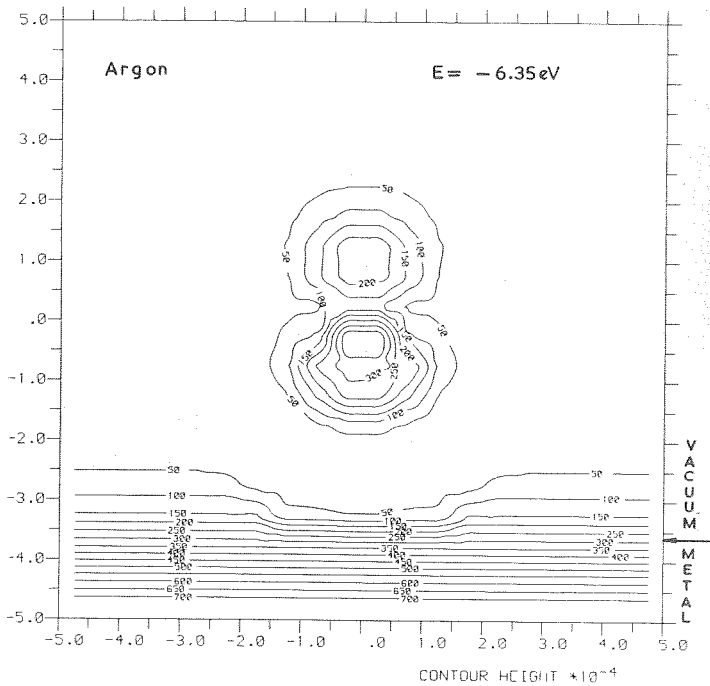


Fig. 11: (a)

Contour plot of $\epsilon(E, r)$ for Ar on jellium substrate for an energy value such that $E > E_{\text{ves.peak}} + \Gamma$. [See caption of Fig. 7 (a) for details of such contours.]

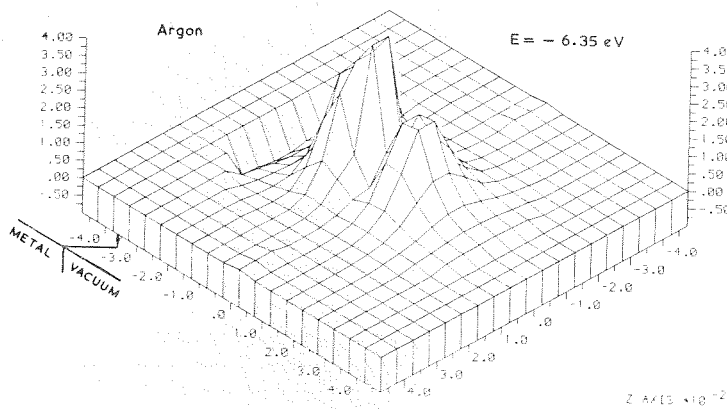


Fig. 11: (d)

Isometric projection of $[\epsilon(E, r) - \epsilon_M(E, r)]$ corresponding to the contour map in Fig. 11 (c).

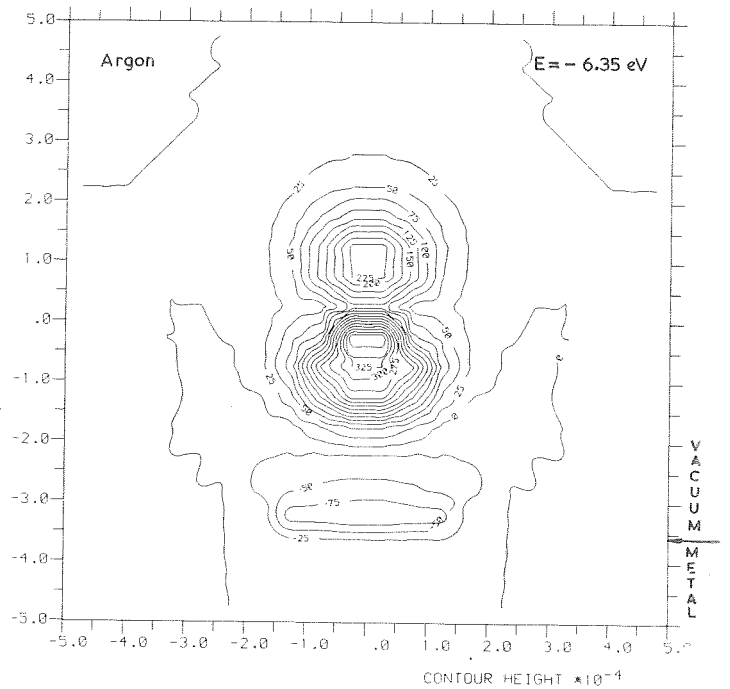


Fig. 11: (c)

Contour plot of $[\epsilon(E, r) - \epsilon_M(E, r)]$ for Ar jellium substrate for an energy value such that $E > E_{\text{ves.peak}} + \Gamma$. [See caption of Fig. 7 (c) for details of such contours.]

The wave function for the state $|L\rangle = |E^L, \underline{k}_{11}, k_{1,inc}\rangle$ of the semi-infinite crystal without the impurity can conveniently be written in the form

$$\psi^L = \frac{1}{V^{\frac{1}{2}}} \sum_{\underline{g}} B_L^0(\underline{k}_{11} + \underline{g}) \exp [i(\underline{k}_{11} + \underline{g}) \cdot \underline{r}_{11}] \exp \left\{ - \left[\frac{2m}{\hbar^2} (-E) + (\underline{k}_{11} + \underline{g})^2 \right]^{\frac{1}{2}} \cdot z \right\} \quad (37)$$

for $z > 0$. We recall that in (37) V is the volume of the crystal, \underline{k}_{11} is a reduced wave vector in the Surface Brillouin Zone (SBZ) surface under consideration, (\underline{g}) are the reciprocal vectors of the two-dimensional lattice for the same surface and $k_{1,inc}$ is the normal component of the wave vector of the corresponding state in the infinite crystal. One can show that by using (37) we have:

$$\langle \rho_M(E, Z_a) \rangle = \frac{1}{4\pi^3} \sum_{k_{1,inc}} \int \int_{SBZ} d^2 k_{11} \left(\left| \frac{\partial E^L}{\partial k_{1,inc}} \right|^{-1} \sum_{\underline{g}} |B_L^0(\underline{k}_{11} + \underline{g})|^2 \right)_{E^L=E} \times \exp \left\{ -2 \left[\frac{2m}{\hbar^2} (-E) + (\underline{k}_{11} + \underline{g})^2 \right]^{\frac{1}{2}} \cdot Z_a \right\} \quad (38)$$

Because of the exponential term in the above equation most of the contribution to $\langle \rho_M(E, Z_a) \rangle$, and hence to $p(E)$, and hence to $\mu_M(E)$, comes mostly from the term corresponding to $\underline{g} = 0$. It is well known that in transition metals a considerable number of terms corresponding to $\underline{g} \neq 0$ contribute significantly in (37), and that the number $N(\text{Imn})$ of \underline{g} vectors that contribute significantly in this equation depends on the crystallographic plane (Imn). In the case of tungsten one finds that, $N(110) = 5$, $N(100) = 9$, $N(112) = 13$, $N(111) = 33$, $N(012) = 68$. The situation for simple metals, for which a jellium model is a reasonable approximation, is different. In this case most of the contribution to the wave function Eq. (37) comes from the $\underline{g} = 0$ term.

Hence the individual wave function in a transition metal contributes approximately $N(\text{Imn})$ times less to $\langle \rho(E, Z_a) \rangle$ as compared to a jellium state, provided the coefficients $B_L^0(\underline{k}_{11} + \underline{g})$ in (37) are of comparable magnitude. In this respect, the jellium model used in our calculation, gives a value for $\langle \rho_M(E, Z_a) \rangle$, and hence for $\mu_M(E)$ which is roughly $N(\text{Imn})$ times larger than what we should expect for a transition metal surface of the basis of the above arguments. On the other hand the density of states in a transition metal, represented by $\left| \frac{\partial E^L}{\partial k_{1,inc}} \right|^{-1}$ in (38), is on average larger than that of a free-electron model by a factor:

$$\lambda = \frac{\langle \rho_W \rangle}{\rho_0} \quad (39)$$

where $\langle \rho_W \rangle$ denotes the volume average of the valence electronic density in the region of the unit cell outside the muffin-tin sphere. For tungsten¹⁹ $\langle \rho_W \rangle = 0.269 \text{ \AA}^{-3}$. The corresponding quantity for the jellium model is denoted by ρ_0 . In writing (39) we used the fact that in the present case $(E_F - V_0) = 8.5 \text{ eV}$, which is approximately equal to the width of the occupied section of the conduction band of tungsten as calculated by Mattheiss²³. With the

above choice of parameters $\rho_0 = 0.112 \text{ \AA}^{-3}$ and hence $\lambda = 2.4$. Hence we expect that $\mu_M(E_F)$ for the (Imn) plane of tungsten will be approximately $Q(\text{Imn}) = \lambda/N(\text{Imn})$ times the value calculated using the jellium model. The correct $\mu(E)$ for a value of $Q = \lambda/5$ is shown by the broken curves in Figs. 5 and 6. The corrected values for $\mu(E_F)$ per adsorbed atom for the different crystallographic planes obtained in the above manner are shown in column 5 of Table 2. We observe that these numbers do not order in the same way as those obtained by Engel and Gomer (column 3) assuming a uniform distribution of adsorbates at monolayer coverage ($7.9 \times 10^{14} \text{ atoms/cm}^2$ for Ar, $7.2 \times 10^{14} \text{ atoms/cm}^2$ for Kr). We emphasize, however, that the assumption of a constant adsorbate density for every plane, made by Engel and Gomer¹¹, may not be obtained from Engel and Gomer's data by assuming the following adsorbate densities at monolayer coverage.

The (110) plane is closely packed and for that reason one may assume that the inert atoms, which have a diameter considerably larger than that of the tungsten atom, do not «see» the geometry of the surface. Hence the maximum coverage postulated by Engel and Gomer is retained. For the (100), (111) and (112) planes the situation is different and a c(2x2) overlayer seems more justified on simple geometrical arguments (see also ref. 20). For the (012) plane not only a (1x1) overlayer but a c(2x2) overlayer for the (100), (112) and (111) planes. For the (012) plane we give in parenthesis the value appropriate for a c(2x2) overlayer. We see that with a plausible choice of adsorbate densities the induced dipole moments for different planes, order in the manner predicted by our semi-empirical theory. The case of Kr on the (110) plane is a notable exception. We note, however, that the calculated values for $\mu(E_F)$ are smaller than the values shown in column 4.

We emphasize that the semi-empirical values in Table 2 for the induced dipole moments on tungsten are larger than the corresponding values for simple metals as given by (29), and in qualitative agreement with the results of Table 1.

It seems to us that the present semi-empirical theory provides a satisfactory basis for the explanation of the experimental data on the physisorption of inert atoms, although improvements will certainly be required for a full quantitative analysis. The obvious next step in the development of the theory would be a calculation of the induced polarization using the full crystal potential for the metal substrata. Although such a calculation is bound to be lengthy, it is certainly possible on the basis of the theory presented in refs 7 and 18

4. BINDING ENERGY OF THE ADSORBED ATOM

The binding energy of the adatom is the difference between the sum of the total energies of the clean metal and the free inert atom, and the total energy of the metal-adatom system. In each case the total energy is given by²¹

$$E_{\text{total}} = \sum_i E_i n_i - \int d^3r U_{\text{eff}}[\rho(\underline{r}); \underline{r}] \rho(\underline{r}) + \int d^3r \epsilon_{\text{XC}}[\rho(\underline{r})] \rho(\underline{r}) + E_{\text{es}} \quad (40)$$

where E_i denotes the «pseudo eigenvalue» corresponding to the i^{th} electronic state as defined in the Kohn and Sham formalism or the Xa method¹⁶, and n_i is the occupation number of this state. U_{eff} denotes effective potential one electron sees. The third and fourth terms in (40) represent the exchange and the electrostatic contribution to the total energy.

In the case of physisorption there is no considerable re-distribution of the charge on adsorption, hence in calculating the binding energy the change in the second, third and fourth terms in (40) can be neglected in a first order approximation. The electronic states of the metal are very little affected by the physisorbed atom (with the exception of surface states that may exist on the surface), hence we can estimate the binding energy of the adsorbed atom from the shift in the energy level of the valence states of the atom following its adsorption. In the case of Ar and Kr, these states become resonances as shown in Fig. 3, and the change in energy on adsorption must be calculated from the following formula

$$\Delta E \approx \int_{E_{\text{res.peak}} - \Gamma}^{E_{\text{res.peak}} + \Gamma} (E - E_p) \rho_{\text{ADS}}(E) dE \quad (41)$$

where E_p is the valence energy level of the free atom.

We calculate the binding energy for equilibrium metal-adatom separation $Z_a^{(1)} = a_0$. From Table 3 we see that the values of the binding energy calculated in the above manner are in reasonably good agreement with the available experimental data^{9,11}. For Ar and Kr the calculated values in parenthesis correspond to a metal-adatom separation

$$Z_a^{(2)} = (a_0 + 0.2) \text{ \AA} \quad . \quad \text{It might be interesting to observe that the calculated binding energies for the two metal-}$$

adatom separations are approximately related through the expression

$$\Delta E(Z_a^{(2)}) \approx \Delta E(Z_a^{(1)}) \left(\frac{Z_a^{(1)}}{Z_a^{(2)}} \right)^3 \quad (42)$$

which suggests that the binding energy depends on the metal-adatom distance in the manner of (1). The experimental values for the binding of Ar and Kr shown in the table represent averages over different crystallographic planes¹¹. If we exclude the (110) plane the binding energies for individual planes¹¹ do not deviate by more than 5% from their average value,

which suggests that the details of the electronic properties of the metal surface are not as important in the determination of the binding energy as they seem to be in the determination of $\mu_M(E_F)$, and hence of the total induced dipole moment $\mu(E_F)$, as defined by (29). On the other hand, this observation is consistent with our assumption that the contribution to the dipole moment described by μ_A of (30) does not depend critically on the nature of the metal surface. We note that the uncertainty in the experimental values of the binding energy is due to the fact that the adsorbate density at full monolayer coverage is not known with sufficient accuracy¹¹. As a result of this uncertainty a more critical examination of the

present theory is not, at the moment, possible. It is obvious, however, that our estimate of the binding energy on the basis of (41) is quite reasonable. A more elaborate calculation, which takes into account the crystalline character of the metal is possible using the theory presented in refs 7 and 18, but such a calculation would be justified only if accurate experimental results for the absolute value of the binding energy of an individual atom were available.

ACKNOWLEDGMENTS

I wish to thank Dr. A. Modinos of Salford University, England, and Professor T. B. Grimley of Liverpool University, England, for useful discussion. I am indebted to Professor K. Schwart of Technical University of Vienna, Austria, for sending me his self-consistent potentials for Ne, Ar and Kr. The numerical calculations were carried out on the ICL 19045 computer of Salford University and the ICL 19065 computer of Liverpool University.

REFERENCES

1. T. B. Grimley, in: *Molecular processes on solid surfaces*, edited by E. Dranglis, R. D. Gretz and R. J. Tafee. McGraw-Hill, New York, NY. (1969).
2. F. Cyrot - Lackman, *J. Vac. Sci. Technol.* **9**, 1045 (1972).
3. J. P. Gaspard and F. Cyrot - Lackman, *J. Phys. C: Solid St. Phys.* **6**, 3077 (1973).
4. R. Haydock, V. Heine and M. J. Kelly, *J. Phys. C: Solid St. Phys.* **5**, 2845 (1972); *J. Phys. C: Solid St. Phys.* **8**, 2591 (1975).
5. V. M. Tapilin, S. L. Cunningham and W. H. Weinberg, *Phys. Rev.* **B18**, 2656 (1978).
6. T. B. Grimley and E. E. Mola, *J. Phys. C: Solid St. Phys.* **9**, 3437 (1976).
7. A. Modinos and G. Oxinos, *Can. J. Phys.* **56**, 1531 (1978).
8. J. C. P. Mignolet, *J. Chem. Phys.* **21**, 1298 (1953).
9. G. Ehrlich and F. G. Hudda, *J. Chem. Phys.* **30**, 493 (1959).
10. R. Gomer, *Australian J. Phys.* **13**, 391 (1960).
11. T. Engel and R. Gomer, *J. Chem. Phys.* **52**, 5572 (1970).
12. C. Mavroyannis, *Mol. Phys.* **6**, 593 (1963).
13. E. Ziarembe and W. Kohn, *Phys. Rev.* **B13**, 2270 (1976).
14. R. S. Mulliken, *J. Am. Chem. Soc.* **74**, 811 (1952).
15. K. Schwart, *Phys. Rev.* **B5**, 2466 (1972).
16. J. C. Slater, *Quantum Theory of Molecules and Solids*, Vol. 4 (McGraw-Hill 1974).
17. C. Lea and R. Gomer, *J. Chem. Phys.* **54**, 3349 (1971).
18. G. Oxinos and A. Modinos, *Can. J. Phys.* **58**, 1126 (1980).
19. R. M. Nieminen and C. H. Hodges, *J. Phys. F: Metal Phys.* **6**, 573 (1976).
20. N. Kar and P. Soven, *Solid State Commun.* **20**, 977 (1976).
21. N. D. Lang and W. Kohn, *Phys. Rev.* **B1**, 4555 (1970).
22. E. W. Plummer and R. D. Young, *Phys. Rev.* **B1**, 2088 (1970).
23. L. F. Mattheiss, *Phys. Rev.* **139**, A1893 (1965).

THE DEPENDENCE OF $\rho_{\text{ADS}}(E)$ ON $\langle \rho_{\text{M}}(E, z=Z_a) \rangle$
FOR SIMPLE METALS WITH A SURFACE IMPURITY.

The «Atomic Density of States», $\rho_{\text{ADS}}(E)$, for the metal-adsorbate system, described by the model Hamiltonian introduced in Sect. 2-2, is defined by

$$\rho_{\text{ADS}}(E) = \int_{|\vec{r}-\vec{R}_a| \leq a_0} \rho(E, \vec{r}) d^3r \quad (\text{A1.1})$$

where $\rho(E, \vec{r})$ is given by (10) with $\Psi(\vec{r})$ in the same equation given by (11d), and the integration is over the volume of the muffin-tin sphere of the adsorbed atom. We can obtain a more explicit expression for $\rho_{\text{ADS}}(E)$ as follows. We have

$$\rho_{\text{ADS}}(E) = \frac{V}{4\pi^3} \int \int_{|\vec{k}_{\parallel}| < k_{\parallel, \text{max}}} d^2k_{\parallel} \left(\frac{\partial E}{\partial k_{z; k_{\parallel}}} \right)^{-1} \langle |\Psi_0(\vec{r}_{\parallel}, z=Z_a)|^2 \rangle \times \sum_{\ell m} |\hat{\gamma}_{\ell m}(\vec{k}_{\parallel})|^2 I_{\ell}(E) \quad (\text{A1.2})$$

where $\langle |\Psi_0(\vec{r}_{\parallel}, z=Z_a)|^2 \rangle \equiv \frac{1}{A} \int \int |\Psi_0(\vec{r}_{\parallel}, z=Z_a)|^2 d^2r_{\parallel}$ (A1.3)

$$\hat{\gamma}_{\ell m}(\vec{k}_{\parallel}) = 4\pi \sum_{\ell' m'} \frac{[j_{\ell}^j(qa_0) + S_{\ell}^a(E) h_{\ell}^{(1)}(qa_0)]}{R_{\ell}(a_0)} \begin{bmatrix} \mathbb{I} & \mathbb{G} & \mathbb{S}^a \\ \sim & \sim & \sim \end{bmatrix}_{\ell m; \ell' m'}^{-1} \times (i)^{\ell'} (-1)^{m'} Y_{\ell' -m'}(\hat{q}_{\vec{k}_{\parallel}}^+) \quad (\text{A1.4})$$

$$I_{\ell}(E) \equiv \int_0^{a_0} [R_{\ell}(r)]^2 r^2 dr \quad (\text{A1.5})$$

We obtained (A1.2) by substituting into (A1.1) the expression for $\rho(E, \vec{r})$ as given by (10) with $\Psi(\vec{r})$ in the same equation given by (11d), and then performing the angular integration with respect to \hat{r}_a using the orthogonality properties of the spherical harmonics. The integration in (A1.3) is over an area A parallel to the metal-vacuum interface and $\Psi_0(\vec{r}_{\parallel}, z=Z_a)$ can be obtained from (4b). In what follows we endeavour to show that there exists a close connection between $\rho_{\text{ADS}}(E)$ and the average density of states $\langle \rho_{\text{M}}(E, z=Z_a) \rangle$ of the clean metal defined by

$$\langle \rho_{\text{M}}(E, z=Z_a) \rangle = \frac{1}{A} \int \int \rho_{\text{M}}(E, \vec{r}_{\parallel}, z=Z_a) d^2r_{\parallel} \quad (\text{A1.6})$$

where $\rho_{\text{M}}(E, \vec{r})$ is given by (3) with $\Psi_0(\vec{r})$ in the same equation given by (4b). The relationship between $\rho_{\text{ADS}}(E)$ and $\langle \rho_{\text{M}}(E, z=Z_a) \rangle$ will become self-evident if we obtain a more explicit expression for the latter quantity. We have

$$\langle \rho_{\text{M}}(E, z=Z_a) \rangle = \frac{V}{4\pi^3} \int \int_{|\vec{k}_{\parallel}| < k_{\parallel, \text{max}}} d^2k_{\parallel} \left(\frac{\partial E}{\partial k_{z; k_{\parallel}}} \right)^{-1} \langle |\Psi_0(\vec{r}_{\parallel}, z=Z_a)|^2 \rangle \quad (\text{A1.7})$$

where $\langle |\Psi_0(\vec{r}_{\parallel}, z=Z_a)|^2 \rangle$ is given by (A1.3), which in turn can be written in the explicit form

$$\langle |\Psi_0(\vec{r}_{\parallel}, z=Z_a) \rangle = \frac{1}{V} |T^{\text{LR}}(k_{\parallel})|^2 \exp\{-2 \left[\frac{2m}{\hbar^2} (-E) + k_{\parallel}^2 \right]^{\frac{1}{2}} \cdot Z_a \} \quad (\text{A1.8})$$

For given energy E integrals in (A1.7) and (A1.2) are dominated by the exponential term in (A1.8). We recall that we are concerned with negative energies ($E < 0$). Putting $k_{\parallel} = 0$ in all non-exponential terms in (A1.7) and (A1.2) (an approximation which is obviously justified), and using (A.8) we get an expression for $\rho_{ADS}(E)$ in terms of $\langle \rho_M(E, z=Z_a) \rangle$. We have

$$\rho_{ADS}(E) = \langle \rho_M(E, z=Z_a) \rangle \sum_{\ell m} \left| \hat{\gamma}_{\ell m}(k_{\parallel} = 0) \right|^2 I_{\ell}(E) \quad (A1,9)$$

where $\hat{\gamma}_{\ell m}(k_{\parallel} = 0)$ is given by (A1.4) with $k_{\parallel} = 0$, $I_{\ell}(E)$ is given by (A1.5) and $\langle \rho_M(E, z=Z_a) \rangle$ takes the simple form

$$\langle \rho_M(E, z=Z_a) \rangle = \frac{2^{\frac{1}{2}}}{\pi^2} \left(\frac{m}{\hbar^2} \right)^{\frac{1}{2}} \frac{(E - V_0)}{(-V_0)} I_A(E) \quad (A1,10)$$

where

$$I_A(E) = \int_0^{k_{\parallel, \max}} dk_{\parallel} k_{\parallel} \exp\left\{-2 \left[\frac{2m}{\hbar^2}(-E) + k_{\parallel}^2 \right]^{\frac{1}{2}} \cdot Z_a \right\} \quad (A1,11)$$

Note that the above integral can be performed analytically using the standard method of integration by parts.



HP-85 Hewlett-Packard's personal computer designed for professionals

The HP-85 offers the power and capabilities of a desktop computer at an attractive price. The result is a unique combination of price and performance that will appeal to professionals for use in technical, industrial and business applications.



A complete computer system in one small package



TELEREXA LTD 2H Aphrodite Street, Tel. 45628, NICOSIA



ELMASCO LTD

**ELMASCO LTD. &
ΓΕΑΡΟ ELECTRICAL SUPPLIES CO. LTD.**

ΕΙΣΑΓΩΓΕΙΣ ΥΛΙΚΩΝ ΗΛΕΚΤΡΙΚΩΝ ΕΓΚΑΤΑΣΤΑΣΕΩΝ

Όδος Μέδοντος αρ. 9
Τηλ. 66405 (3 γραμμάι)
Τέλεξ 3075
Λευκωσία

Διαθέτομεν τήν μαγαλυτέρα ποικιλία καί πληρεστέρα σειρά υλικών
διά ηλεκτρικά καί τηλεφωνικά εγκαταστάσεις όπως:

Καλώδια όλων των τύπων, πρίζες, φίσιες,
λαμπτήρες, φλορένσες, αυτόματους διακόπτες
κουδούνια, ασφάλειες, φωτιστικά, προβαλείς,
ηλεκτρικά σίδερα, ηλεκτρικά εξαρτήματα
κ.λ.π. κ.λ.π.

Μπορείτε να προμηθευθήτε από τα καταστήματά μας ότι χρειάζεται
διά την ηλεκτρικήν εγκατάσταση:

- Της οικίας σας
- Του ξενοδοχείου σας
- Του εργοστασίου σας
- Του εργαστηρίου σας.

Εξυπηρετούμε τους πελάτες μας, κάνουμε εύκολιες στην πληρωμή.
Πωλήσεις λειανικά καί χονδρικά.

ΚΑΤΑΣΤΗΜΑΤΑ

ΛΕΥΚΩΣΙΑΣ

Γωνία Στασάνδρου &
Αφριδίτης
Τηλ. 73354

ΠΑΦΟΥ

Νικολάου "Ελληνα 39
Τηλ. 33644

ΛΕΜΕΣΟΥ

Αγίας Ζώνης 30
Τηλ. 62916

ΛΑΡΝΑΚΟΣ

Κ. Καλογερά Α+Β
Τηλ. 57543

THREE - PHASE INDUCTION MACHINES UNDER CONDITIONS OF A SINGLE PHASE SUPPLY

G. Kladeftiras

Electrical Engineering Department (3E2) of H.T.I.

Abstract

We present a study of the behaviour of a 3 - phase star connected induction machine under conditions of a single phase supply. Under these conditions we show that the torque developed by the machine at standstill is zero and therefore the machine cannot start. At any other slip there is a net torque developed which however vanishes when the slip takes the values zero and two. If the machine is made to rotate at a speed very near to the Synchronous speed, we show that there exist at the terminals of the machine an almost 3 - phase balanced system of voltages. We also show that the machine can be made to be self starting by connecting an external impedance between the disconnected machine terminal and any other terminal. The above are consistent with experiments we have carried out in the machine's laboratory of the H.T.I.

Introduction.

If the voltages applied to the three stator terminals of a 3 - phase *star connected* induction machine constitute a 3 - phase balanced system of voltages, then the performance of the machine is said to be «normal» and one could predict the behaviour of the machine whether acting as a motor or as a generator by using standard established methods. However if the voltages applied to the terminals of the machine are unbalanced, the machine performance will be modified.

The most direct approach to the problem is by the analysis of the set of unbalanced voltages into two symmetrical sets of balanced voltages of positive and negative phase sequence respectively. Each set produces corresponding balanced currents, and the synthesis of the two sets of current vectors represents the actual current produced in the three stator phases by the original unbalanced voltages. The behaviour of the machine to the positive phase sequence voltages, is «normal». The negative phase sequence voltages, however set up a reverse rotating field so that if the motor slip is S with respect to the «normal» sequence, it will be $(2-S)$ to the negative sequence. The machine behaves as the addition of two separate machines, one running in one direction at a slip S , with a terminal voltage of V^+ per phase, and the other running in the other direction at a slip $(2-S)$, with a terminal voltage of V^- per phase.

Theory

Without external impedance connected

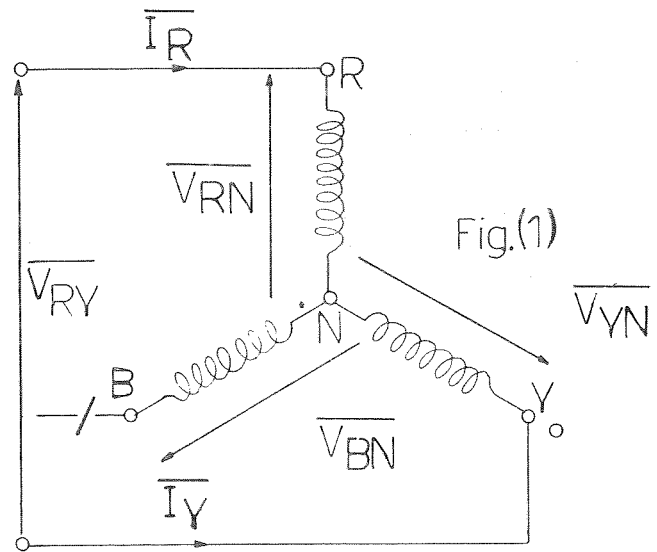
The analysis which follows is applicable for a three phase star connected induction machine, when the blue phase becomes disconnected, as shown in fig (1).

V_{RN} , V_{YN} and V_{BN} represent an unbalanced system of three phase voltages in vectorial form.

$$\text{Hence. } V_{RN} = V_{R+} + V_{R-} \quad (1)$$

$$V_{YN} = V_{Y+} + V_{Y-} \quad (2)$$

$$V_{BN} = V_{B+} + V_{B-} \quad (3)$$



$$V_{Y+} = a^2 V_{R+} \quad (4)$$

$$V_{B+} = a V_{R+} \quad (5)$$

$$V_{Y-} = a V_{R-} \quad (6)$$

$$V_{B-} = a^2 V_{R-} \quad (7)$$

a is an operator which turns a complexor through 120° in an anticlockwise direction and is given by

$$a = -0.5 + j\frac{\sqrt{3}}{2}$$

Similarly, I_{R+} , I_{Y+} and I_{B+} represent an unbalanced system of three phase Currents. in vectorial form.

Hence

$$I_R = I_{R+} + I_{R-} \quad (8)$$

$$I_Y = I_{Y+} + I_{Y-} \quad (9)$$

$$I_B = I_{B+} + I_{B-} \quad (10)$$

$$I_{Y+} = a^2 I_{R+} \quad (11)$$

$$I_{B+} = a I_{R+} \quad (12)$$

$$I_{Y-} = a I_{R-} \quad (13)$$

$$I_{B-} = a^2 I_{R-} \quad (14)$$

From fig (1) it is seen that

$$\begin{aligned} V_{RY} &= V_{RN} - V_{YN} \\ &= V_{R+} + V_{R-} - V_{Y+} - V_{Y-} \\ &= (1-a^2) V_{R+} + (1-a) V_{R-} \end{aligned} \quad (15)$$

Since the blue phase becomes disconnected, the current flowing through it is zero. Hence

$$I_R + I_Y = 0$$

$$I_{R+} + I_{R-} + I_{Y+} + I_{Y-} = 0$$

$$(1+a^2) I_{R+} + (1+a) I_{R-} = 0 \quad (16)$$

If the positive and negative sequence admittances per phase are Y_{R+} and Y_{R-} respectively, then

$$I_{R+} = V_{R+} \cdot Y_{R+} \quad (17)$$

$$I_{R-} = V_{R-} \cdot Y_{R-} \quad (18)$$

Substituting equations (17) and (18) in to equation (16) we get

$$V_{R+} \cdot Y_{R+} (1+a^2) + V_{R-} \cdot Y_{R-} \cdot (1+a) = 0 \quad (19)$$

From equation (15) we get

$$V_{R+} = \frac{V_{RY} - V_{R-} \cdot (1-a)}{(1-a^2)} \quad (20)$$

Substituting equation (20) into equation (19) and solving for V_{R-} we get

$$V_{R-} = \frac{V_{RY} \left(\frac{Y_{R+}}{Y_{R+} + Y_{R-}} \right)}{(1-a)} \quad (21)$$

Substituting equation (21) into equation (20) we get

$$V_{R+} = \frac{V_{RY} \left(\frac{Y_{R+}}{Y_{R+} + Y_{R-}} \right)}{(1-a^2)} \quad (22)$$

The positive phase - sequence equivalent circuit of the induction machine is shown in fig (2a). If the machine rotates at a given speed N , the synchronous speed of the machine due to the positive phase sequence components is N_s . The slip of the rotor due to the positive phase sequence components is S_f .

$$S_f = \frac{N_s - N}{N_s} \quad (23)$$

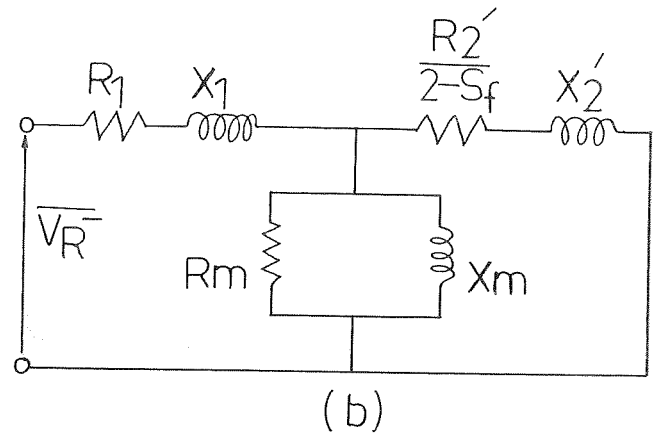
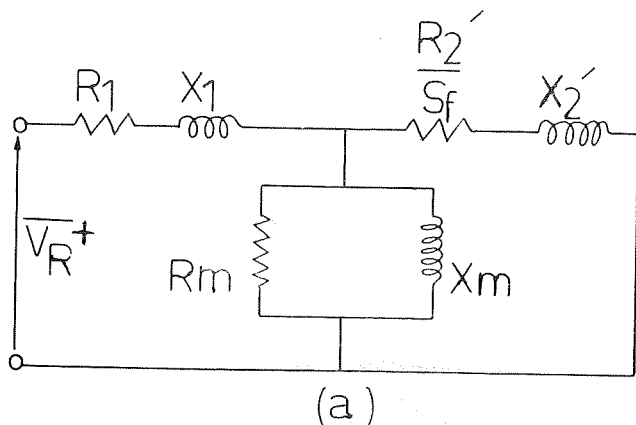


fig (2):- Phase - sequence networks of a three phase star connected induction machine
(a) Positive (b) Negative

R_1 is the stator resistance per phase
 X_1 is the stator leakage reactance per phase
 R_m is a resistance accounting for core losses per phase
 X_m is the magnetizing leakage reactance per phase
 R_2' is the rotor resistance per phase referred to the stator
 X_2' is the rotor leakage reactance at standstill per phase referred to the stator.

The negative phase - sequence equivalent circuit of the machine is shown in fig (2b). This is the equivalent circuit of the machine when a negative phase - sequence 3 - phase supply is applied to the stator and the rotor is driven in the opposite direction to the direction of rotation of the stator field. If the machine rotates at a given speed N , the synchronous speed of the machine due to the negative phase sequence components is $-N_s$. The slip due to the negative phase sequence components is S_b .

$$S_b = \frac{-N_s - N}{-N_s} = \frac{N_s + N_s - N_s + N}{N_s} = \frac{2N_s}{N_s} \left(\frac{N_s - N}{N_s} \right) \quad (24)$$

$$= 2 - S_f$$

The positive and negative sequence impedances per phase of the machine can be obtained from the phase - sequence networks of the machine shown in fig. (2). From the positive phase sequence network of the machine it can be shown that the positive sequence impedance per phase Z_{R+} is given by the following expression.

$$Z_{R+} = \frac{\left(\frac{R_2'}{S_f} + jX_2' \right) \cdot \left(\frac{R_m j X_m}{R_m + jX_m} \right)}{\left(\frac{R_2'}{S_f} + jX_2' \right) + \left(\frac{R_m j X_m}{R_m + jX_m} \right)} + (R_1 + jX_1) \quad (25)$$

Similarly, from the negative phase sequence network of the

machine it can be shown that the negative sequence Impedance per phase Z_{R-} is given by the following expression.

$$Z_{R-} = \frac{\left(\frac{R_2'}{(2-S_f)} + jX_2' \right) \left(\frac{R_{mj} X_m}{R_m + jX_m} \right)}{\left(\frac{R_2'}{(2-S_f)} + jX_2' \right) + \left(\frac{R_{mj} X_m}{R_m + jX_m} \right)} + (R_1 + jX_1) \quad (26)$$

If the machine is made to rotate at a speed very near to the synchronous speed, equation (23) shows that the slip approaches zero. Under this condition, if we substitute for S_f the value zero into equation (25), we see that the positive sequence impedance per phase Z_{R+} approaches infinity, so that the positive sequence admittance per phase Y_{R+} approaches zero. If we substitute for Y_{R+} the value zero, into equations (21) and (22) we see that the negative phase sequence voltages become zero and we have a three phase balanced system of voltages at the terminals of the machine, due to the positive phase sequence voltages only, as shown by the equations below.

$$V_{R+} = \frac{V_{RY}}{(1-a^2)} \quad V_{Y+} = a^2 \frac{V_{RY}}{(1-a^2)} \quad V_{B+} = a \frac{V_{RY}}{(1-a^2)}$$

The positive phase sequence currents give rise to a forward travelling mmf component wave and the negative phase sequence currents to a backward travelling mmf component wave, so that the positive phase sequence network may be used to calculate the forward torque, and the negative - sequence network to predict the backward torque.

It can be shown that the forward torque component per phase T_{R+} for a three phase induction machine is given by

$$T_{R+} = \frac{R_2'}{2\pi N_s S_f} \cdot \frac{|V_{R+}|^2}{\left[(R_1 + \frac{R_2'}{S_f} + (X_1 + X_2')^2) \right]} \quad (27)$$

It can also be shown that the backward component per phase T_{R-} for a three phase induction machine is given by

$$T_{R-} = \frac{R_2'}{2\pi N_s S_f} \cdot \frac{|V_{R-}|^2}{\left[\left(R_1 + \frac{R_2'}{(2-S_f)} \right)^2 + (X_1 + X_2')^2 \right]} \quad (28)$$

The resultant torque, due to the forward torque component and the backward torque component is given by

$$T_{RES} = T_{R+} - T_{R-} \quad (29)$$

where T_{R+} and T_{R-} are given by equations (27) and (28) respectively.

At standstill, the slip S_f due to the positive sequence components is unity. Substituting this value of S_f into equations (25) and (26) we see that the positive sequence impedance per phase is equal to the negative sequence impedance per phase. Consequently the positive sequence

admittance per phase is equal to the negative sequence admittance per phase, i.e.

$$Y_{R+} = Y_{R-} = Y_R \quad (30)$$

Substituting equation (30) into equations (21) and (22) we see that the absolute value of the positive phase sequence voltage is equal to the absolute value of the negative phase sequence voltage, i.e.

$$|V_{R+}| = |V_{R-}| \quad (31)$$

Substituting equation (31) into equations (27) and (28), and bearing in mind that S_f is unity, we see that the forward torque component is equal to the backward torque component, so that the resultant torque is zero and the machine cannot start. If the machine rotates at synchronous speed, it was shown that the positive sequence admittance per phase is zero, so that the negative phase sequence voltages are zero. Consequently the backward torque per phase is zero. If we substitute for S_f the value zero into equation (27), we see that the forward torque per phase is also zero. Therefore, if the machine rotates at synchronous speed, the net torque developed by the machine is zero.

If the machine rotates at a slip equal to two, the negative sequence admittance per phase is zero, so that the positive phase sequence voltages are zero. Consequently the forward torque per phase is zero. If we substitute for S_f the value two into equation (28) we see that the backward torque per phase is also zero. Therefore, if the machine rotates at a slip equal to two the net torque developed by the machine is zero.

With external impedance connected.

If an external admittance Y_x is connected between the red phase and the blue phase, as shown in fig(3), the machine can be made self starting.

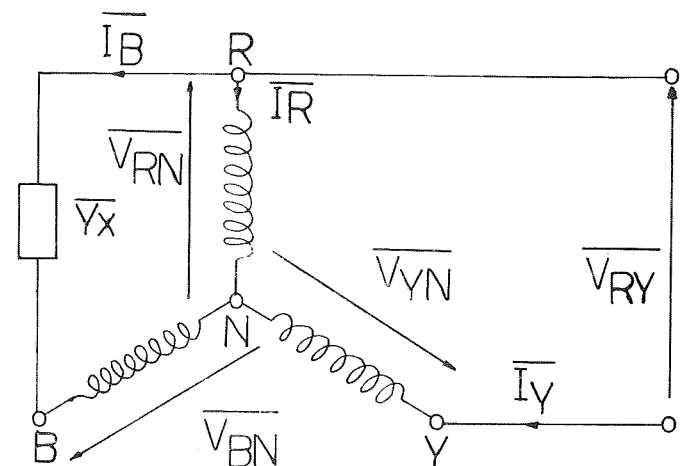


Fig.(3)

From fig.(3) it is seen that

$$\begin{aligned} V_{RY} &= V_{RN} - V_{YN} \\ &= V_{R+} + V_{R-} - V_{Y+} - V_{Y-} \\ &= (1-a^2) V_{R+} + (1-a) V_{R-} \end{aligned} \quad (15)$$

$$\begin{aligned}
V_{RB} &= V_{RN} - V_{BN} \\
&= V_{R^+} + V_{R^-} - V_{B^+} - V_{B^-} \\
&= (1-a) V_{R^+} + (1-a^2) V_{R^-} \quad (32)
\end{aligned}$$

$$\begin{aligned}
I_B &= V_{RB} \cdot Y_X \\
I_{B^+} + I_{B^-} &= V_{RB} \cdot Y_X \\
a I_{R^+} + a^2 I_{R^-} &= V_{RB} \cdot Y_X \quad (33)
\end{aligned}$$

Substituting the expression for V_{RB} as given by equation (32) into equation (33) we obtain

$$a I_{R^+} + a^2 I_{R^-} = \left[V_{R^+}(1-a) + V_{R^-}(1-a^2) \right] Y_X \quad (34)$$

Substituting equations (17) and (18) for I_{R^+} and I_{R^-} respectively into equation (34), we have

$$\begin{aligned}
a V_{R^+} \cdot Y_{R^+} + a^2 V_{R^-} \cdot Y_{R^-} &= Y_X \left[V_{R^+}(1-a) + V_{R^-}(1-a^2) \right] \\
V_{R^+} \cdot \left[a Y_{R^+} - (1-a) Y_X \right] &= V_{R^-} \cdot \left[(1-a^2) Y_X - a^2 Y_{R^-} \right] \quad (35)
\end{aligned}$$

From equation (15) we get

$$V_{R^-} = \frac{V_{RY} - V_{R^+} \cdot (1-a^2)}{(1-a)} \quad (36)$$

Substituting equation (36) into equation (35) for V_{R^-} we get

$$V_{R^+} = \frac{V_{RY} \left[(1-a^2) Y_X - a^2 Y_{R^-} \right]}{(a-a^2) \left[Y_{R^+} + Y_{R^-} + 3Y_X \right]} \quad (37)$$

Substituting equation (37) into equation (36) for V_{R^+} , we get

$$V_{R^-} = \frac{V_{RY}}{(1-a)} \left[1 - \frac{(1-a^2) \left[(1-a^2) Y_X - a^2 Y_{R^-} \right]}{(a-a^2) \left[Y_{R^+} + Y_{R^-} + 3Y_X \right]} \right] \quad (38)$$

At standstill the slip S_f due to the positive sequence components is unity, and it was shown that under this condition the positive sequence admittance per phase is equal to the negative sequence admittance per phase. i.e. $Y_{R^+} = Y_{R^-} = Y_R$. Careful examination of equations (37) and (38) shows that $|V_{R^+}| = |V_{R^-}|$ and therefore the forward and backward torques are different. Hence the machine is self starting by developing a net torque at standstill.

Conclusions.

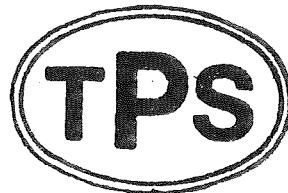
We have presented a study of the behaviour of a 3-phase star connected induction machine under conditions of a single phase supply. Under these conditions we have shown that the torque developed by the machine at standstill is zero and therefore the machine cannot start. At any other slip there is a net torque developed which however vanishes when the slip takes the values zero and two. If the machine is made to rotate at a speed very near to the synchronous speed, we have shown that there exist at the terminals of the machine an almost 3-phase balanced system of voltages. We have also shown that the machine can be made to be self starting by connecting an external impedance between the disconnected machine terminal and any other terminal. The above are consistent with experiments we have carried out in the Machine's Laboratory of the H.T.I.

Acknowledgements:

I wish to express my thanks to Dr G. Oxinos, lecturer of the H.T.I. in Electrical Engineering, for his close guidance and supervision under which this work was carried out. My thanks are extended to Mr J. Demetriou, Laboratory Instructor of the H.T.I., for his contribution in verifying the theoretical predictions experimentally.

WITH THE COMPLIMENTS
OF
TAKIS PARPAS & SONS LTD.

P.O.Box 3820
6, Them. Dervis Str.
Nicosia-Cyprus



TEL. 55148 — 45036
TELEX 3243 PARCO
Telegrams PARPAS

ELECTROMECHANICAL ENGINEERING AND
CONTRACTING COMPANY
LIGHTING FITTINGS SHOW ROOM

Engineering Installations at home

With more than 30 years experience on Electrical and Electromechanics and abroad.

DESIGN OF A VERTICAL AXIS AEROGENERATOR

By M. Pattichis, Lecturer, H.T.I.

1. INTRODUCTION

The idea of conversion of the kinetic energy of a moving mass of air (otherwise known as «a wind») into other forms of energy, e.g. mechanical or electrical, is increasingly proving one of the stronger candidates of the «alternative sources of energy » contest. The term «soft technology » is often used amongst those circles of people (broadly known as «environmentalists ») who are more concerned with the preservation of the environment than with the economic costs involved in achieving this, to distinguish between these alternative sources and the more traditional sources of energy e.g. coal, crude oil, gas and the more recent nuclear. The latter sources definitely do affect the environment adversely, either by depleting the irreplaceable natural resources, or by posing a continuous hazard of large scale catastrophes due to nuclear station accidents. However, the term «soft» is not synonymous with «cost-effective» and as the latter is the ruling parameter of our socio-economic system the «soft» systems must be - as a first step - as cost effective as the traditional systems.

There is no doubt that the enormous improvement in living standards, which most societies have experienced in this century, was brought about by the adoption of large scale industrialisation. Unavoidably, the scale of energy consumption also increased enormously and I would suggest that the **rate** of increase in demand was such that the available financial resources were largely absorbed by capital expenditure on new and improved traditional power stations. Funding on development of alternative sources of energy was kept at a minimum since the traditional sources were at least an order of magnitude more cost-effective. The dependence of the industrialised countries on crude oil gradually became absolute and it was no big surprise that the recent OPEC policy of cut-backs in production - so as to preserve their oil deposits - with the law of supply and demand in operation, brought about the much talked about international «energy crisis». A better term would be «financial crisis due to energy costs» because the ten fold increase in price of crude oil, through a chain reaction of economic events, has shaken the foundations of the international financial structure.

As a result of the energy crisis the «alternative sources» became fashionable almost overnight and a lot more resources have been diverted by the developed countries into the research and development of such sources. Energy extraction from the wind has received its fair share of funding, especially in the U.S. where the development of 2MW aerogenerators to lock into the national grid is well on its way. Also a new industry has sprung up in the supply of small aerogenerators for individual houses, with local authorities in some areas giving the incentive for investment in such systems by allowing the users to lock into the grid and even «turn the meter back» when the system is generating more power than the user requires.

Work on alternative sources and conservation of energy in Cyprus is mostly carried out by the Ministry of Industry

and staff of the Higher Technical Institute. An Energy Research Group (ERG) was set up at the H.T.I., with clearly defined objectives, and experimental work is now being conducted on solar and biomass energy systems. Work on wind energy was initiated by the author in the form of supervision of a final year project, which was undertaken by Mr S. Zachariades, and concentrated exclusively on a literature survey on wind energy systems abroad.

Following this excellent piece of work it was decided to push ahead with the design and construction of a small aerogenerator on a limited budget of £500. The aerodynamic/structural design presented below was developed by the author while the electrical/electronic design is currently being investigated by Mr G. Kourtellis and Mr S. Spyrou. The mechanical construction has been undertaken by a final year student, Mr S. Flouris. It is hoped that this pilot plant will form the basis of further work on aerogenerator systems that may have potential application here in Cyprus.

1. BASIC CONCEPTS OF WIND ENERGY

The maximum power that can be extracted from a wind of velocity V_{∞} and density ρ by an aerogenerator of frontal area A can be determined by looking at an idealised flow pattern system, fig.1. Here the aerogenerator is assumed to produce a uniform change of velocity and pressure through it and the flow is assumed incompressible, inviscid and irrotational. By Bernoulli it can be shown that the change of pressure caused by the aerogenerator is,

$$\Delta p = \frac{1}{2} \rho (V_{\infty}^2 - V_w^2)$$

The drag force, F_d experienced by the aerogenerator is $\Delta p \cdot A$,

$$F_d = \frac{1}{2} \rho A (V_{\infty}^2 - V_w^2) \quad (1)$$

But also from Newton's second law the drag force is given by mass flow rate times change of velocity,

$$F_d = \rho VA (V_{\infty} - V_w) \quad (2)$$

Equating (1) and (2) gives

$$V = \frac{1}{2} (V_{\infty} + V_w) \quad (3)$$

The power extracted from the wind, P , is

$$P = F_d V$$
$$P = \rho AV^2 (V_{\infty} - V_w)$$

and substituting for V_w from (3) gives

$$P = 2\rho AV^2 (V_{\infty} - V) \quad (4)$$

The maximum power is obtained by

$$\frac{\partial P}{\partial V} \Big|_{V_{\infty}, A} = 0$$

which yields,
$$V = \frac{2}{3} V_{\infty}$$

Substituting this into (4) we see that for a given A and V_{∞} the maximum power is

$$P_{\max} = \frac{8}{27} \rho A V_{\infty}^3 \quad (5)$$

As it is essential to work with dimensionless parameters, the «power coefficient», C_p , is defined as the ratio of ex-

tracted power, P, to power available, $\frac{1}{2} \rho A V_{\infty}^3$

$$C_p = \frac{P}{\frac{1}{2} \rho A V_{\infty}^3} \quad (6)$$

It can be seen that from (5) the maximum value that C_p can take for any aerogenerator is

$$C_{p\max} = \frac{(8/27) \rho A V_{\infty}^3}{\frac{1}{2} \rho A V_{\infty}^3} = 0.593 \quad (7)$$

This is the theoretical maximum. The assumption made in the theory above are in practice not strictly true - air is viscous and compressible - the degree to which they hold depending on Reynold's number and Mach number of a particular case. In practice then, the value of C_p is less than 0.593 depending on the design of a particular aerogenerator axis. The former rotate a horizontal shaft while the latter rotate a vertical shaft, fig. 2. Historically the vertical axis type is more recent, with the horizontal type originally used for water pumping in agricultural areas - most of us have at some time or other seen a multi-bladed, slow-running windmill. Modern horizontal axis aerogenerators use blades of airfoil section, similar to aircraft propellers and are fast-running, while the vertical axis family has two subgroups: The fast-running, airfoil - bladed group e.g. Darrieus and the slow-running, cup-bladed group e.g. Savonius.

The power coefficient, C_p , depends on the speed of rotation of an aerogenerator. A dimensionless speed parameter, known on the «tip speed ratio», X_{∞} , may be defined as the ratio of the velocity of the extreme tip of the aerogenerator to the velocity of the wind,

$$X_{\infty} = \frac{\omega R_{\max}}{V_{\infty}} \quad (8)$$

where ω is the speed of rotation and R_{\max} is tip radius from axis of rotation.

Plots of C_p versus X_{∞} are shown in fig. 3 for the various designs of aerogenerator. Although the $C_p - X_{\infty}$ for a given type, say a Darrieus, is close to that shown in fig. 3, certain parameters may shift the curve: the shape of the airfoil, the roughness of the blade surface, the number of

blades, the chord length and Reynold's number are the main parameters that may cause such a shift.

All aerogenerators transmit the aerodynamically generated torque through a shaft to an alternator. However, as alternators generally start generating (cut - in speed) around 1000 r.p.m. it can be seen that step-up of the aerogenerator shaft speed is required. As an example, consider a horizontal two-bladed aerogenerator which is to operate at maximum C_p at a tip speed ratio of 5 and which is designed to start producing electrical power when the wind speed is 4m/s. If the radius is 2.5m then the angular velocity will be 8 rad/s. However the cut-in speed of the alternator is roughly 100 rad/s which means a step-up ratio of about 12.5. Step-up can be effected by gearing or by belt/pulley arrangements.

3. AERODYNAMIC DESIGN OF A VERTICAL AXIS AEROGENERATOR

After careful consideration of the relative advantages and disadvantages of the vertical and horizontal axis groups, it was decided that the vertical type is much more attractive for the following reasons: (a) the need for wind orientation devices - tails - is eliminated, and (b) the alternator, and step-up arrangements need not be placed close to the axis of rotation i.e. at the top of a necessarily stronger tower.

The following is the aerodynamic analysis of a vertical axis aerogenerator of the «Giromill» type as shown in fig. 4a. Consider this system rotating at a constant angular velocity, ω , when the wind passing through the aerogenerator is V. Considering the velocity vector diagram, fig. 4b, it is clear that the blade, when at an angle from the wind direction, will experience a velocity U at an angle α to its chord line. The blade will therefore experience an aerodynamic lift force, L, and drag force D, as shown in fig. 4c. The torque, T, produced by each blade is

$$T = LR \sin \alpha - DR \cos \alpha \quad (9)$$

Introducing the lift coefficient

$$C_L = \frac{L}{\frac{1}{2} \rho U^2 ch},$$

and drag coefficient

$$C_d = \frac{D}{\frac{1}{2} \rho U^2 ch}, \text{ equation 9) becomes}$$

$$T = \frac{1}{2} \rho ch R \left\{ U^2 C_L \sin \alpha - U^2 C_d \cos \alpha \right\} \quad (10)$$

Now from wing theory the lift and drag coefficients are functions of α as,

$$C_L = K_L \sin \alpha, \quad C_d = C_{d0} + \zeta C_L^2 \quad (11)$$

where C_{d0} is a constant which depends on the Reynold's number, Re , of the flow ($Re = uc^2/\mu$, where μ is the viscosity of air) and for a smooth surface is of the order of 0.01 for Reynold's numbers greater than about 200,000. From fig. 5 the parameter K_L and ζ are seen to be slopes of the $C_L \sim \sin \alpha$ and $C_d \sim C^2$ curves within the working

range of α . Previous workers have taken K_L and ζ as constants but in this analysis the results of lifting line theory for K_L are used

$$K_L = 2\pi A_R / (2 + A_R), \quad \zeta = 1 / \pi A_R \quad (12)$$

where $A_R = h/c$ is the *Aspect Ratio* for a blade. Equations (12) apply to wings of A_R greater than 4, and of thickness/chord ratio less than 10%. Substituting (11) into (10) and noting from fig. 4b that

$$U \sin \alpha = V \cos \delta$$

$$v = U \cos \alpha + V \sin \delta$$

it is easily determined that the *mean* value of torque over a cycle ($0 \leq \theta < 2\pi$), T_m , for each blade is

$$T_m = \frac{1}{2} \rho c h R \left\{ v^2 K_L (1 - \zeta K_L) - 2 c_{d0} v^2 \left(1 + \frac{v^2}{V^2}\right) \right\} \quad (13)$$

The mean power produced by n blades then is

$$P = n T_m \omega = \frac{n}{4} \rho c h R \left\{ v^2 K_L (1 - \zeta K_L) - 2 c_{d0} v^2 \right\} \omega \quad (14)$$

where the term $(V/v)^2$ is ignored as it is much smaller than 1. The power coefficient is obtained by dividing (14) by $1/2 \rho 2R h v_{\infty}^3$ giving

$$C_p = \frac{1}{2} \left(\frac{n\sigma}{2R}\right) \left\{ \frac{v^2}{v_{\infty}^2} K_L (1 - \zeta K_L) - 2 c_{d0} \frac{v^2}{v_{\infty}^2} \right\} \omega R$$

This can be written as

$$C_p = \frac{1}{2} \sigma X_r (v/v_{\infty})^3 \left\{ K_L (1 - \zeta K_L) - 2 c_{d0} X_r^2 \right\} \quad (15)$$

where $\sigma = nc/2R$ is usually defined as the «*solidity ratio*» and $X_r = \omega R/V$ is the tip speed ratio based on the velocity V . In our case $n=2$ as two blades will be used. Now the drag force acting on the aerogenerator can be determined by resolution of L and D forces in the wind direction, fig. 4c. This gives the drag force for each blade as

$$F_d = \left\{ L \cos \alpha \cos \delta - D \cos \alpha \sin \delta \right\} + \left\{ L \sin \alpha \sin \delta + D \sin \alpha \cos \delta \right\}$$

Substituting for L and D from (11) and integrating over ($0 \leq \theta < 2\pi$) to find the mean value of F , it can be shown that for n blades,

$$F_d = (n/2) V \rho c h K_L \quad (16)$$

However from energy considerations F_d is also given by equation (4) as

$$F_d = 2 \rho A V (V_{\infty} - V) \quad (17)$$

Equating (16) and (17) gives,

$$V_{\infty}/V = 1 + \frac{\sigma}{8} K_L X_r \quad (18)$$

The parameter V_{∞}/V is from this point to be denoted by symbol z . Before we proceed to search for the optimum

design by making use of (15) and (18), at this point it is useful to state the constraints which the design is subjected to. Firstly, the tip speed ratio X_r must be around 4 so that the blades do not stall at any point in the cycle, fig. 4b. Secondly, the Reynold's number must be greater than about 200,000 so that the flow pattern over the blades results in the assumed value of $C_{d0} = 0.01$ and also the $C_L \sim \sin \alpha$ stall point is not at a low α . Other constraints are the centrifugal forces experienced by the blades and the stresses set up due to these forces. It can be shown that the centrifugal force, $m v^2/R$, when made dimensionless by dividing by $1/2 \rho A V_{\infty}^2$, it is proportional to σ^2/z^2 . The stress in the blades due to bending moments given by Engineer's Theory of Bending is proportional to Force xh/c^3 ; this can be made dimensionless by multiplying by $c^2/1/2 \rho A V_{\infty}^2$ and the dimensionless stress is thus proportional to $\sigma^2 A_R/z^2$. Also the mass of a blade which is proportional to $c^2 h$ can be made dimensionless by dividing by C_A i.e. the dimensionless mass is proportional to σ .

Optimum Design: From equation (15) it is clear that C_p is a function of four parameters, namely solidity ratio, tip speed ratio, aspect ratio and z . As a first step the σ and A_r are kept fixed so as to see the response of C_p to X_r . From (15),

$$\delta C_p = \left(\frac{\partial C_p}{\partial X_r} \right) \delta X_r + \left(\frac{\partial C_p}{\partial z} \right) \delta z$$

while from (18)

$$\delta z = \left(\frac{\partial z}{\partial X_r} \right) \delta X_r$$

Performing the differentiations it can be shown that

$$\frac{d C_p}{d X_r} = \frac{1}{2} \sigma (1/z)^3 \left\{ K_L (1 - \zeta K_L)^3 - 6 c_{d0} X_r^2 \right\} - \frac{3}{16} \sigma^2 K_L (1/z)^4 \left\{ K_L (1 - \zeta K_L) - 2 c_{d0} X_r^2 \right\} X_r \quad (19)$$

The maximum occurs when $dc_p/dX_r = 0$ which gives the condition

$$X_r = \frac{-\frac{\sigma}{8} K_L^2 (1 - \zeta K_L) + \sqrt{\frac{\sigma^2}{64} K_L^4 (1 - \zeta K_L)^2 + 6 c_{d0} K_L (1 - K_L)}}{6 c_{d0}} \quad (20)$$

Equation (20) gives the value of X_r , at a maximum C_p , for a given A_R and σ . Obviously such maxima are important as the aerogenerator is to be designed to operate close to the maximum C_p . A computer program was written to run on the H.T.I. PDP-11 system to produce results of C_p as a function of X_r , fig. 6 for various values of A_R and σ . Also for a given A_R and σ equation (20) was used to give the C_p and X_r values of the maximum C_p of that particular case, so that the first constraint stated above can be examined at a glance. In fig. 6 are shown the results for two values of A_R at several values of σ . Note that C_p values are higher for the higher values of σ .

The results from the above analysis, fig. 6, created some interesting questions which required further investigation. Instead of sifting through hundreds of curves to select a suitable one, some further degree of automatic selection was desirable. Further, these results do not really give any indication as to how the $C_p - X_r$ curves may depend on what is to be called here the «*shape factor*» ($= h/R$) which defines the shape of the Giromill, fig. 7. It is easily shown that

$$A_R \sigma = h/R \quad (21)$$

and consequently the results of fig. 6, can be replotted - with some small modification to the program - for given fixed values of h/R , varying from 0.5 to 5, as shown in fig. 8. The conclusions are that as h/R increases, the maximum values of C_p increase but also the values of X_r at which these maxima occur decrease.

As a final improvement to the selection the value of X_r was fixed at the required value of 4 and values of A_R and σ varied but at a fixed h/R so as to find that value of A_R and σ at which C_p is a maximum for the given h/R . Starting from (15),

$$\delta C_p = (\partial C_p / \partial A_R) \delta A_R + (\partial C_p / \partial \sigma) \delta \sigma + (\partial C_p / \partial z) \delta z$$

while from (18)

$$\delta z = (\partial z / \partial A_R) \delta A_R + (\partial z / \partial \sigma) \delta \sigma$$

From (21) we also have, since h/R is a constant,

$$d\sigma / dA_R = -\sigma / A_R$$

Performing the differentiations and putting $\delta C_p = 0$ for a maximum point, the following results:

$$\sigma = \frac{h/R}{A_R} = \frac{4}{X_r} \left\{ \frac{\left(\frac{K_L(1-\zeta K_L)^{-2} c_{d0} X_r^2}{K_L(1-\zeta K_L)^{-2} c_{d0} X_r^2} \right) - \frac{\zeta K_L^2}{2\pi} \left(1 + \frac{K_L}{2\pi} - 2\pi \zeta K_L \right)}{\left(\frac{K_L - \frac{3}{4\pi} \zeta K_L^2}{K_L - \frac{3}{4\pi} \zeta K_L^2} \right) + \frac{K_L}{4\pi} \zeta K_L^2 \left(1 + \frac{K_L}{2\pi} - 2\pi \zeta K_L \right)} \right\} \quad (22)$$

The program was further modified to use an iterative procedure whereby the shape factor h/R is kept fixed and A_R is varied until both sides of equation (22) are identical. The procedure was repeated for a range of values of h/R . In fig. 9 it is seen that for progressively higher values of h/R the value of A_R that satisfied (22), i.e. maximum C_p for $X_r=4$ at a given h/R , increases.

An interesting observation is that the solidity ratio remains almost constant.

A closer examination of the constraints as stated above, brought out the fact that the Reynold's number constraint becomes difficult to fulfill as the aerogenerator size decreases. So while for a large aerogenerator the Reynold's number given by (with $X_r=4$)

$$R_e = 2.6 \times 10^5 \frac{V_\infty C}{z} \quad (23)$$

is satisfied for low values of V_∞ clearly in our case the chord C would have to be given priority in being as large as possible so that the constraint $R_e > 2 \times 10^5$ is satisfied at low V_∞ - the parameter Z remaining around 1.4 for all of the promising results. The chord C is given by

$$C = \sqrt{\frac{A_C}{2A_R}} \quad (24)$$

so clearly a suitable result with high σ and low A_R is required for a small aerogenerator. A relatively high value of σ , however, means a relatively higher penalty on

structural design as a consequence of the centrifugal force, bending stress and mass constraints. Nevertheless, the R_e constraint outweighs all these as it is directly involved in the theoretical assumption of a high Reynold's number at the design point.

The final selection has the following values: $A = 13m^2$, $h/R = 1.5$, $A_R = 10$, $\sigma = 0.15$, $C_{p_{max}} = 0.45$ at $X_r = 4$, $z = 1.395$. The choice was a compromise between a high C_p and a high C . This means that $h = 3.12m$, $R = 2.08m$, $c = 0.312m$. From (23) the value of V_∞ for which the R_e constraint is satisfied is around 3.5 m/s which is satisfactory for our purposes as the aerogenerator will operate in a wind regime of annual mean wind velocities around 5m/s

Perhaps the only disadvantage of this type of aerogenerator is that it is not self starting so some external means is required to rotate it to such a speed that it starts producing positive torque. One method of starting is in the form of a Savonius rotor which has a high starting torque. After a careful consideration of the designs presented in Mr Zachariades' project it was decided to use a Split-Savonius design, fig. 10a. The C_p-X_∞ characteristic is shown in fig. 10b. The dimension R_{tip} was selected so that when the aerogenerator is operating at optimum C_p the Savonius would also operate at the optimum C_p at $X_\infty = 0.84$. This means that as the angular speed ω is the same

$$R_{tip} = \frac{0.84}{4} z R$$

or in our case $R_{tip} = 0.61m$. The finalised design of the aerogenerator currently being constructed at H.T.I. is as shown in fig. 11. Neglecting the power generated by the Savonius, the system should generate 28W at a wind speed of 2m/s, 225W at 4m/s, 690W at 6m/s, 1797W at 8m/s, 3510W at 10m/s and 11,740W at 15m/s.

4. STRUCTURAL CONSIDERATIONS

The two important structural problems are (a) the central shaft and (b) the aerogenerator blades. In fig. 12 are shown the loads which act on the shaft. The worst possible case for the drag force, F_d , occurs when $Z=2$ as can be shown by differentiation of equation (17), but the value of Z at which the aerogenerator will operate is 1.4. This gives a maximum bending stress of 120 MN/m² for a wind speed of 30 miles/hr, for a mild steel hollow shaft of 65 mm external and 41 mm internal diameter. The torque is estimated to be about 600 Nm which produces a maximum shear stress of 20 MN/m² for the same shaft. Also the estimated weight of the structure of about 100 kg produces only 1 MN/m² of stress due to the weight. The principal stresses are therefore primarily depended on the bending stresses and using the Tresca theory of failure the shaft has a safety factor of 1.8.

Now if the blades are to withstand centrifugal forces up wind speeds to 30 miles/hr, then with a mass of about 20 kg for each blade the centrifugal force is about 1400 kgf. distributed over the length of the blade. The maximum bending moment is 3500 Nm which can be resisted by a fiber-glass coating of 6 mm, fig. 13.

5. OTHER CONSIDERATIONS

The matching of the shaft torque characteristic curve to that of the alternator is currently under investigation while the other electrical/electronic parts of the system are being investigated by an electrical engineering team.

Evaluation of the performance of the complete system will be carried out at a later stage and will be reported in a future issue of this magazine.

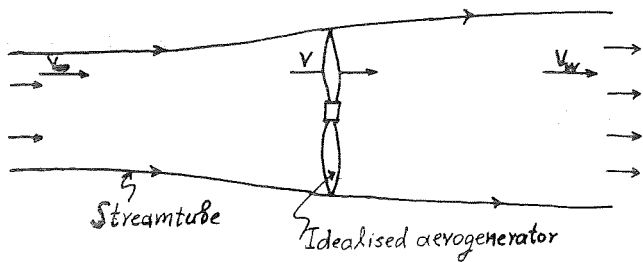


Fig.1: Idealised flow through an aerogenerator

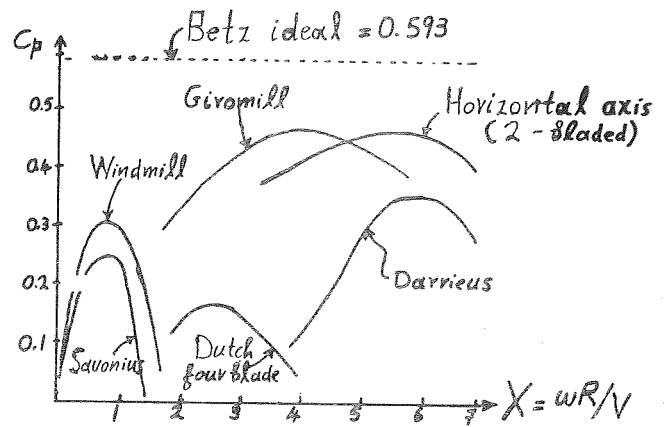


Fig.3: Power coefficient versus tip speed ratio

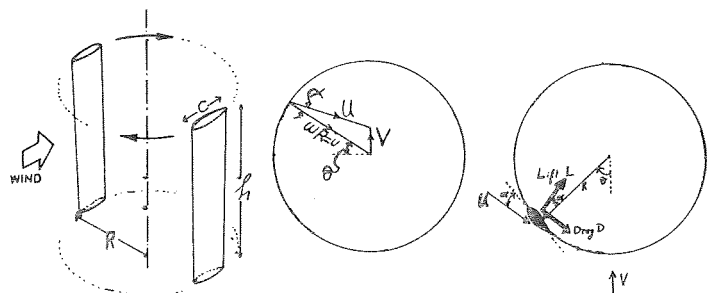
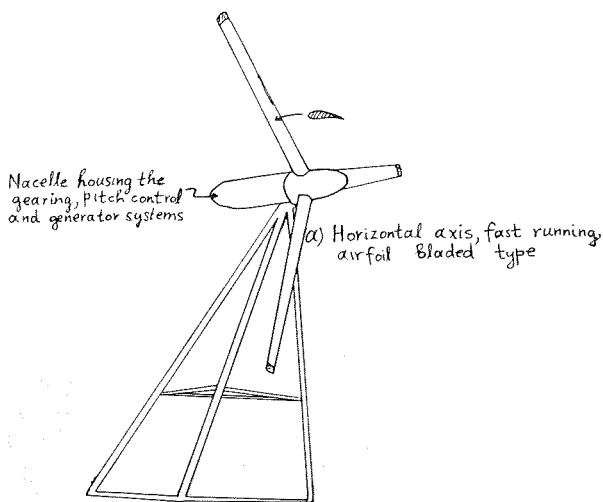
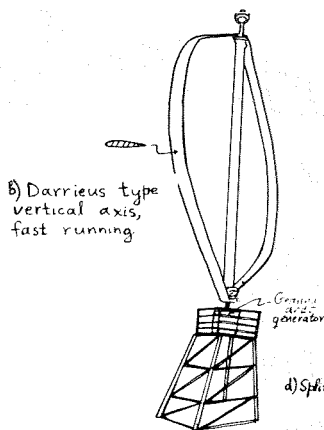


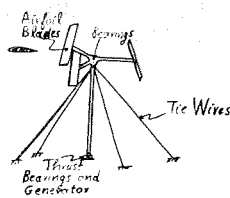
Fig.4: a) Givomill type aerogenerator; b) Velocity vector diagram, c) Lift and drag forces on blade



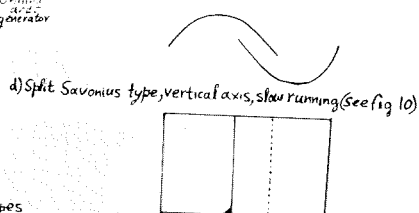
a) Horizontal axis, fast running, airfoil Bladed type



b) Darrius type vertical axis, fast running



c) 'Givomill' type, vertical axis, fast-running



d) Split Savonius type, vertical axis, slow running (See fig 10)

Fig.2 Modern Aerogenerator Types

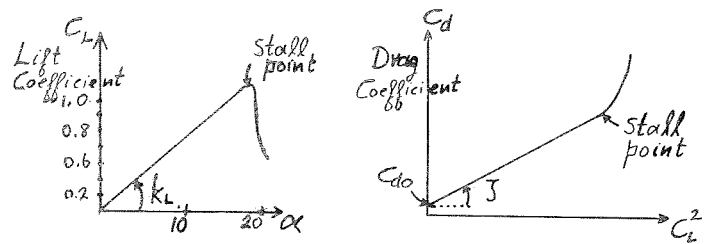


Fig.5. $C_L \propto \alpha$ and $C_D \propto C_L^2$ characteristic curves of symmetrical airfoil

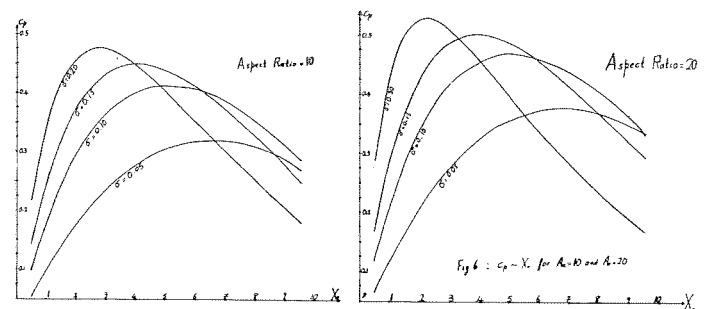


Fig. 6

Fig.6: $C_p - X$ for A=10 and A=20

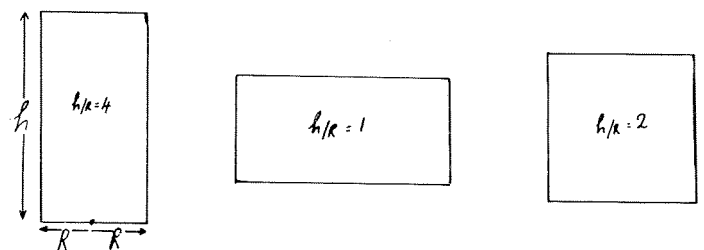
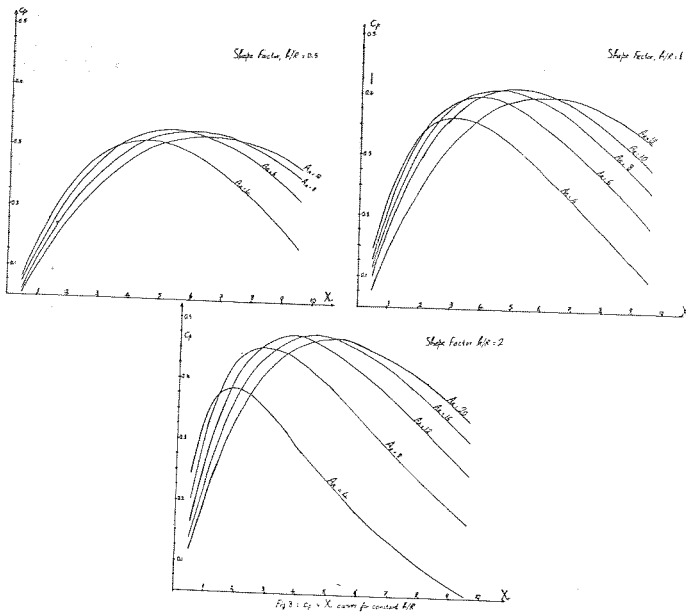


Fig.7. The effect of the shape factor, h/R , on the shape of the aerogenerator



- A: Airfoil blades (NACA 12 section)
- B: Supporting struts
- C: Shaft
- D: Savonius starting device.
- E: Bearings (alignment and thrust) casing
- F: Supporting legs, bolted to a concrete base
- G: Step up pulley system
- H: Bolt
- I: Generator

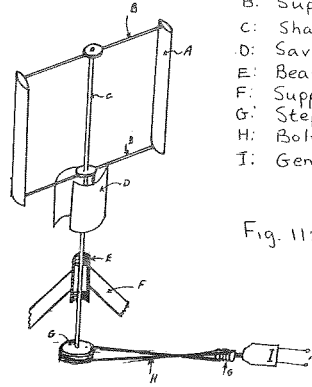
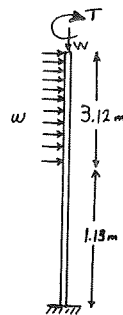
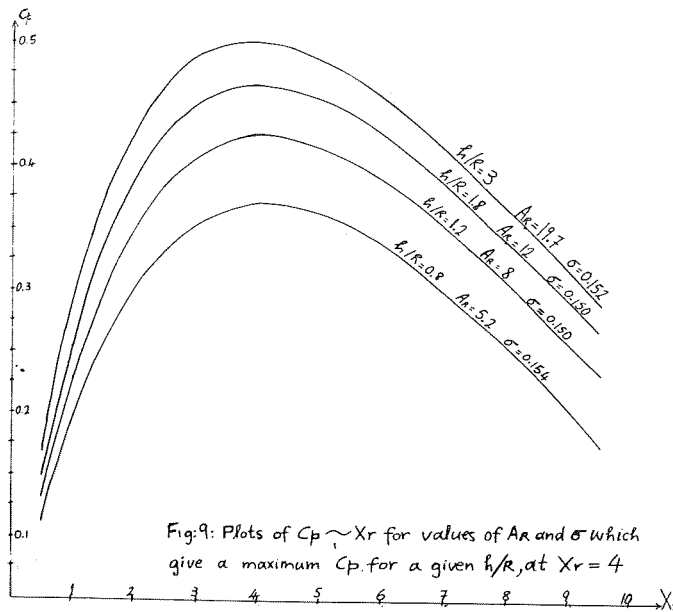


Fig. 11: Main features of Aerogenerator system



$W = Fd/3.12 \text{ N/m}$
 $W = \text{Dead Weight of structure}$
 $T = \text{Torque}$

Fig. 12: Loads acting on central shaft

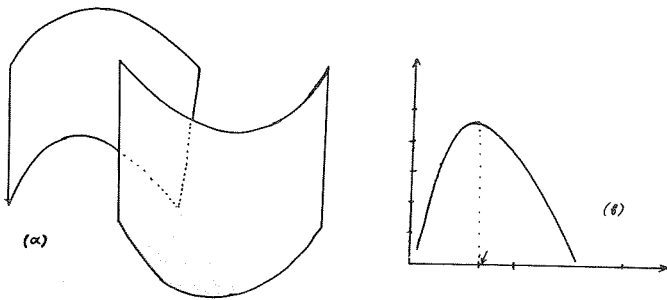


Fig 10 a) Split-Savonius with b) its $C_p \sim X_r$ Curve

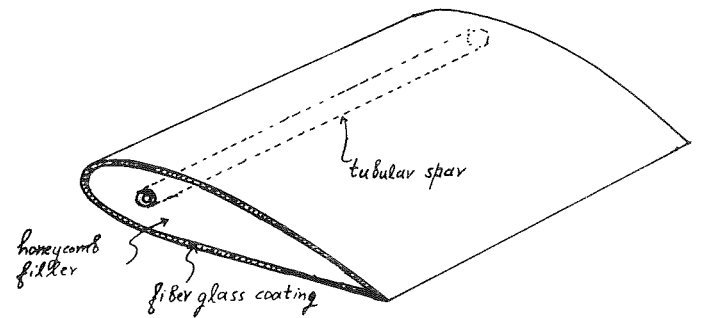
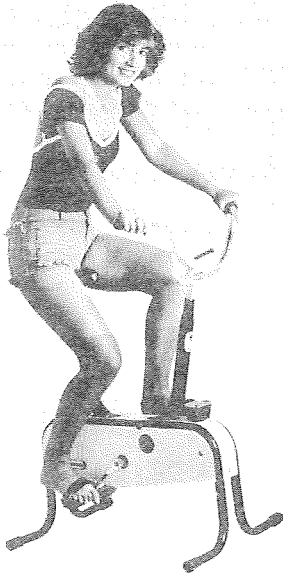


Fig. 13: Constructional details of Blades

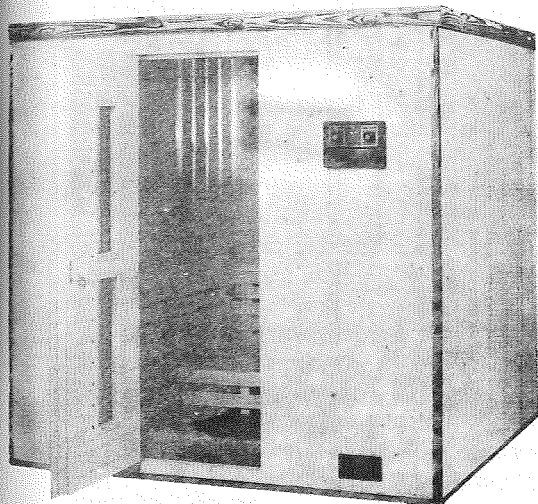
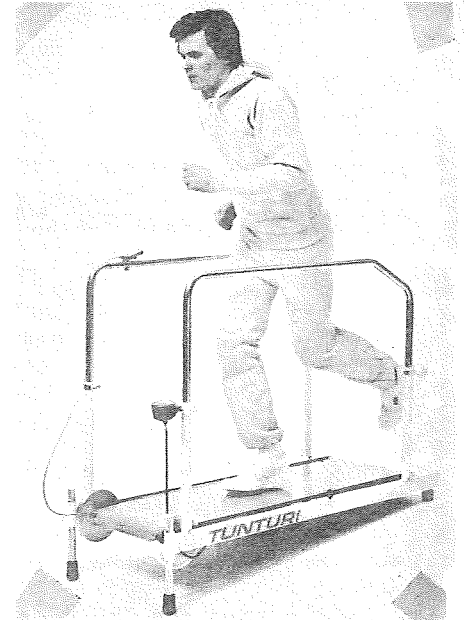
EXERCISE AT HOME

AT «IMPOPHAR» YOU CAN FIND A WIDE RANGE OF EXERCISE EQUIPMENT WHICH WILL HELP YOU TO START YOUR INDOORS EXERCISE AT HOME



OUR RANGE INCLUDES:-

- * EXERCISE CYCLES
- * RELAXATOR CYCLES
- * ROWING MACHINES
- * MASSAGE BELTS
- * HAND MASSAGE UNITS
- * ROLLERS
- * TREADMILLS



ALSO:-

- * FAMILY SAUNA
(ALL SIZES)

- * HOME SAUNA
(FOR ONE PERSON)



IMPOPHAR TRADING HOUSE LIMITED

3A IONA NICOLAOU STREET

PALOURIOTISSA
TEL: 31104

THE ORGANIZATION OF THE QUALITY CONTROL DEPARTMENT

S. Vassiliou, *Quality Control Officer*
 Ministry of Commerce and Industry

1. Introduction

In the past, it was normal for manufacturers to produce a small range of products, employing skilled workers. Such a situation did not require the use of inspection, as each worker was responsible for the quality of his work as well.

The development of technology and the introduction of automatic production machines had enabled the use of unskilled cheap labour in factories, who however were not capable of controlling the quality of production.

These developments in the production processes had led to the employment of specialist staff whose duties were to check and control the quality of production.

2. The contribution of the Quality Control Department

Any successful company, is naturally concerned with maintaining financial viability and hence making a profit. It follows then that in the long term, each department in the company must contribute in some way to the success of the company.

The quality control department contributes in the following ways.

- (1) In the short term, correct application of inspection and quality control techniques should minimise the amount of unsatisfactory products, and work in progress. Such reductions have a direct effect on the firm's profitability.
- (2) In the medium term, complaints from consumers are minimised, and the quality of the production is stabilised, helping the company to maintain its market position.
- (3) In the long term, correct inspection can help to optimise the company's product towards the most economical production. For example if the quality of a component can be made reliable, it is often possible to reduce its dimensions or use an alternative and cheaper material. In addition manufacturing requirement may be relaxed if the variability of production can be controlled.

Correct inspection also allows the company to standardise its materials and processes, thus minimising variation in production process, stock in hand etc.

3. The Functions of the Quality Control Department

The functions of the quality control department is to provide a company service in determining and thereby controlling the quality of the company's production.

To manage this the quality control department must have certain resources, inputs and outputs. Figure 1 is a simplified input/output model of the quality control department.

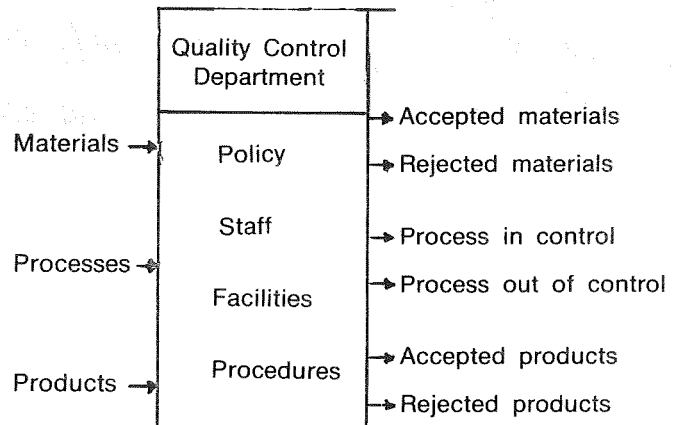


Fig. 1.

To perform its functions, the quality control department must relate to the company organization in some way, and the manner in which it does so is of some interest.

During the early years of the development of the quality control function, it was common for inspectors to report to the production manager, and even for production staff to inspect their own works. Whilst this was acceptable in some low technology/high skill areas, it rapidly became apparent that this relationship placed an intolerable conflict of interests upon the quality control function. Essentially this conflict arose because of the different motivations of production and quality control. The former is primarily concerned with throughput and production targets, whilst the latter is solely associated with conformance to specifications. Occasions must naturally arise when the two interests are opposed, and for this reason it is now considered preferable for the quality control function not to be responsible to the production function. A simple organizational structure is shown in figure 2.

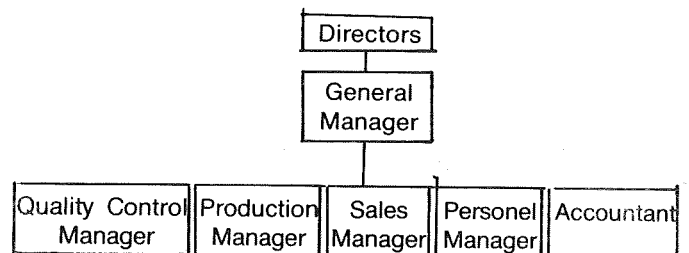


Fig. 2

However, such an arrangement is possible if the size of the company can support it, and it may well be that smaller companies may have to have the quality control function responsible to the Production Manager.

It is important to appreciate that the quality function of a company is not necessarily involved in determining the level of perfection of the product. Such matters are determined by uppermanagement, after taking into account the marketing situation, competition, production costs etc. The actual product is conceived and initially developed by the design and research and development departments, in consultation with the production department. Thereafter, the quality control department is concerned solely with the compliance of the materials, processes, etc. with the appropriate specifications.

4. Structure of the Quality Control Department

Referring to figure 1, it can be seen that the quality control department operates upon 3 distinct lines, namely:

- (1) Materials, i.e. those items which are Purchased by the firm for further processing.
- (2) Processes, i.e. the operations performed upon the materials in order to manufacture the product.
- (3) Products, i.e. the finished product of the Company.

In many respects, the techniques employed in each of these operations are different, and if the firm is large enough, the general structure of the department should be as shown in figure 3.

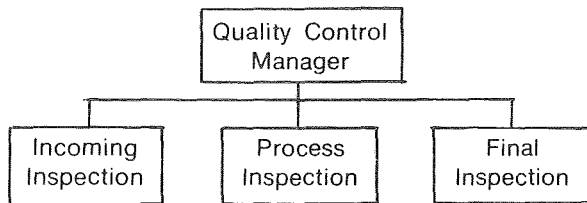


Fig. 3

The incoming inspection is related to the purchasing specification, which must be in sufficient detail to allow for such inspection. It is common practice for such inspection to be based on sampling upon the basis of which the delivery is either accepted or rejected. Where the company is involved in large purchases of materials, it is now common practice to employ a 'vendor rating' scheme, in which the purchaser and the vendor agree to a quality control system to be operated by the vendor, thus reducing the incoming inspection which is restricted to auditing the vendors production.

Process inspection is involved from the moment that materials are released from stores to the time that the product is presented for final inspection. In general, process inspection is conducted after each manufacturing stage prior to the subsequent operation. The objective is to ensure that valuable resources are not wasted in further processing of unsatisfactory materials. The nature

of the inspection, and rate of inspection is, of course, entirely dependent upon the material, process and subsequent use of the product. But inspection should always be conducted on the first production after any resetting of the process, or process stoppage.

Final inspection of products may in some cases be separated into the inspector of simple parameters by the inspections, and testing by the laboratory. Whatever the situation, the objective of product testing is to:

- (1) Protect the Company from consumer complaint
- (2) Ensure that the required level of quality is maintained

5. Inspection facilities

It is essential that the quality department control has adequate and appropriate facilities to perform its duties. The following are of importance.

- (1) Adequate space and furniture for the writing of reports, filing of documents etc.
- (2) Adequate facilities for performing the required operations.
- (3) Environmentally controlled areas where necessary.
- (4) Adequate glare free illumination of appropriate intensity.
- (5) Sufficient storage area for equipment.
- (6) Adequate materials handling facilities for the products in question.

6. Relationship with other departments

1. Production Department

A close and continuing relationship is essential to ensure the following:

- 1.1 Information regarding production program, machine loading, machine changes, new plant etc. to establish the inspection program.
- 1.2 Identification of material in process
- 1.3 Release of in process material for further processing
- 1.4 Feedback relating to quality problems and possible relaxations.

2. Design Department

The relationship with design is not as close as that with production, but is particularly important when new products, or modifications to existing products are contemplated. In this context a liaison with design department is essential to ensure that proposed design features can be adequately controlled.

3 | Purchasing Department

The purchasing of materials, and subsequent release for processing is dependent upon the ability of the inspection department to perform acceptance testing. It is essential that the Purchasing program is available to the quality control department for planning purposes. It should be noted that with regard to purchasing, inspection is related to the purchasing specification, and therefore to the quantity ordered.

4 | Upper Management

The quality control department is dependent upon upper management for its basic policy, and is required to provide regular management information regarding quality performance.

5 | Sales-Marketing

The relationship with sales marketing is normally restricted to assessment of consumer complaints.

The relationship of the quality control department with other departments is shown schematically in fig. 4

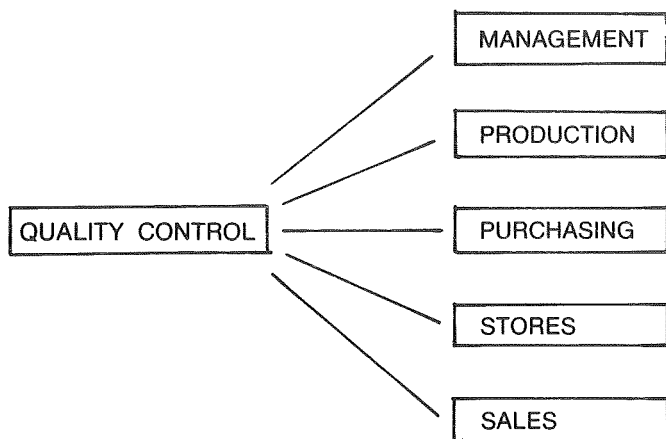


Fig. 4.

7. Who Inspects

When considering incoming inspection, and final inspection, there is little doubt that such inspections should be conducted by the quality control department. However, in the case of process inspection, it is often advantageous for simple inspections to be conducted by the process operator. Naturally such a situation can easily lead to abuse, which must be prevented by adequate operator training, and an auditing of operator performance by the quality control department. The actual costs of either system are similar, but the inspection by the operator prevents undue delays in the production process awaiting stage inspections and assist in operator motivation.

8. Responsibilities of the Quality Control Manager.

The Manager of the quality control department is seldom actually involved in inspection, but is responsible for the various management and administrative functions of his department, as follows:

- (1) Inspection planning, production of manuals and procedures.

- (2) Provision of product and process standards.
- (3) Budget and facilities, instruments etc.
- (4) Assignment of duties.
- (5) Liaison with other departments.
- (6) Review of examples of non conformity.
- (7) Prepare documentation.
- (8) Develop subordinates.
- (9) Keep abreast of developments.

9. What is to be inspected

It must be remembered that quality costs money, and it is often more costly and time consuming to thoroughly inspect a product than to produce it. The routine ongoing inspection of processes, materials and products should be kept to a minimum. It is often possible to restrict such inspection and testing to a series of cardinal parameters which themselves demonstrate compliance. In many cases, it is possible to resort to sample inspection and testing as a means of reducing such costs; in the case of destructive tests, sampling is absolutely necessary. Alternatively, in other cases, especially where personal safety is a factor, it is essential to inspect every item.

10. Quality Manual

It is now common practice for companies to produce a «Quality Manual» in which all the aspects of company quality policy and procedures are detailed. This document has several uses as follows:

- (1) It firmly commits the Company to a carefully considered policy.
- (2) It commits staff to a laid down series of objectives and operations.
- (3) Customers, especially large purchasers, can, and do, use the manual as a basis for their own vendor rating schemes.

11. Inspection Procedures

Each inspection operation, including materials, processes, and product inspection should be provided with a complete and detailed written procedure in which all the following are detailed:

- (1) Sampling procedure and identification of item and specification or drawing.
- (2) Inspection sequence.
- (3) Inspection and test procedure for each parameter, and the equipment to be used.
- (4) Criteria for acceptance and rejection.
- (5) Any retest procedure.
- (6) Procedure for the disposition of accepted or rejected items.

12. Inspection Planning

The Quality Control Manager is responsible for ensuring that the inspection function is performed efficiently, and does not delay production. To do this, inspectors and

test facilities must be programmed to be available when needed, in accordance with the purchasing and production schedules.

13. Inspection Reports

All inspections should be recorded giving at least the following information.

- (1) Date, time and location
- (2) Inspectors identity and procedure used
- (3) Identification of item by lot
- (4) Number of conforming and rejected items
- (5) Destination of accepted items and disposition of rejected items
- (6) Whether reworking is considered appropriate

It is essential that the data produced above is readily available for statistical analysis and in many cases special cards are employed to facilitate this.

14. Inspection Equipment

For obvious reasons, it is vital that equipment used for inspection is maintained in good condition and regularly calibrated. To ensure this an inventory should be maintained of all equipment. Equipment should be removed from service at regular predetermined intervals and subjected to routine maintenance and calibration. For each parameter to be measured, a factory standard should be maintained for calibration purposes e.g. test pressure gauges, standard resistance etc. all calibration

and maintenance should be recorded on the inspection equipment inventory card. Factory standards should also be calibrated at regular intervals, in which case it may be necessary to have such calibration conducted by an independent laboratory. All equipment should be stored in a separate area as free as Practicable from vibration and environmental changes, and released for specific purposes to nominated inspectors.

15. Materials Control

For the purpose of ensuring that in process materials are correctly inspected, each batch of material should be identified by such means as route cards, tags, stamps etc. Provision must be made either on the cards or in the inspection documentation to clear each lot for inspection purposes after each process has been completed. All non conforming items should be clearly identified as to prevent mixing with other material, and consigned as quickly as possible to a quarantine store set aside for that purpose.

16. Inspection Review

As with all other aspects of organisation, the continued use of any system can lead to abuse, short cuts, etc. In addition, the advent of new ideas technology etc. can lead to a situation where the system may be improved. For these reasons, a periodic review should be held to analyse the inspection system for possible improvements. The review period, procedure and results should be fully documented and recorded for future use.



TECON

78, Acropolis Avenue

P.O.Box 5094

TELEPHONE: 24791

TELEX 2962 TECON CY.

**ELECTRICAL
CONTRACTORS
AND AGENTS FOR:**

**MOORLITE
LINOLITE
MARLIN
CANDELL
HOLOPHANE
FURSE**

BRIDGEHOUSE

BOOKSHOP & STATIONERS

SOLON PAPACHRISTODOULOU

BRIDGEHOUSE BLDG., BYRON & GRIVAS DIGENIS AVE., TEL. 43297, P. O. Box 4527
NICOSIA - CYPRUS

International Collection of:

Newspapers & Magazines
School, Language & Literature Books
Technical, Science & Art
Cooking, Housekeeping & Decoration
M & E, Time-Life & Teach Yourself Books
Penguin, Pelican, Pan, Fontana, Gorgi e.t.c.
Chess, Tennis, Bridge & Other Hobbies
Stamps & Coin Collecting Books
Ladybird & Other Children Books
Dictionaries & Reference Books
Books & Model Answers for G.C.E.
Past Examination Papers for G.C.E. L.C.C. e.t.c.
Touring Maps & Guides
School Stationery, Handbags e.t.c.
Office Stationery & Account Books
Office Equipment & Filing Systems
Typing & Duplicating Materials
Envelopes of all Kinds & Sizes
Fountain & Ball Pens
Autographs & Address Books
Drawing & Art Instruments
Albums for Photos, Stamps & Coins
Educ. Toys & Handcraft works
Cards for All Occasions
Christmas Decorations & Candles
Gift Wrapping Papers & Decorations

**Books & items not in stock
can be ordered for you**

IT IS OUR PLEASURE TO SERVE YOU

ANALYSIS OF THE CYCLE OF THE SOLAR POWER STATION

Jerzy Konrad Nowakowski

*Institute of Thermal Engineering in Lodz, Poland
Consultant for the Ministry of Commerce & Industry, Cyprus
UNDP Adviser on Heat Pumps and Heating and Ventilation*

Here are described the results of the thermodynamic analysis of a heliothermic power plant in an open and a closed cycle with various working media, as well as the regulation and protection procedure and the method of designing an absorber of solar rays.

The actual design work concerning the utilization of solar energy in solar power stations moves in two main directions (1)(2):

1/A heliothermal power station, in which takes place the transformation of solar radiation into thermal energy, driving subsequently the heat engine.

2/A helioelectric power station, in which occurs direct transformation of solar radiation into electric energy.

A heliothermal power station may be made in the shape of a solar farm or of a system with a solar tower. In the system with the solar farm, designed for lower power, collectors are used in the shape of parabolic mirrors equipped with tubes absorbing solar radiation, the tubes being placed in exact focal lengths. Through the tubes flows the working medium, being heated to a temperature of 350° C. The system with the solar tower consists of mirrors, i.e., of heliostats concentrating solar radiation upon an absorber placed at the top of the tower. The heat of the working medium, with temperature $t = 800 : 900^{\circ}\text{C}$ is transferred either to a heat exchanger or to a steam generator. A heliothermal power station must be equipped with an additional source of heat in the form of a steam boiler fired with fossil fuel and set in operation for the production of electric energy in case of lack of direct solar radiation or in case of exhaustion of the heat storage battery.

The helioelectric power station transforms, by means of photoelectric cells, direct and diffused solar radiation into electric energy. This type of power station, merged with an electrochemical storage working in the nighttime, may be used in the Central European weather zone, prevailing in Poland. The costs of constructing a helioelectric power plant, are mainly on account of the high cost of photoelectric cells. None the less, it is expected that in the future, when electric cells become less expensive, the construction of a helioelectric station will be competitive in to respect the heliothermal power plant.

In the Institute of Fluid-Flow Machines in Hannover, several alternative designs of cycles of a heliothermal power plant were designed with a solar tower in an open and in a closed system, using air and helium as circulating media (3). In Fig. 1 are shown, in the T-S system cycle, diagrams of a solar power plant in an open and a closed

system, whereas on Fig. 2 are represented block diagrams of the installations constituting this power plant. The compressors (a) and (b) force air into the heat exchanger (g) and from it into the solar absorber (e). Air heated to the temperature of 800° C and at a pressure of about 4.4MPa (closed cycle) and 0.459 MPa (open cycle) is subsequently expanded in a turbine (i) driving the generator (k). After its expansion the hot medium transmits the outlet heat from the turbine to the inlet air in the heat exchanger (g). The operation of the sun not being constant in time, in order to stabilize the power. Both the heat storage battery (f) and the combustion chamber (h) are used for conventional fuel. The regulation of heat streams is performed by means of valves (o), (p), (p'), as well as (r) and (r').

The statement of the basic parameters of the cycle of the heliothermal power plant has been given on Table 1.

Designations	Units	Open	Closed	
		cycle air	helium	cycle air
1 Final power	MW	0.25	20	20
2 Temperature in the turbine inlet	°C	800	800	800
3 Number of interstage coolings	-	1	1	1
4 Pressure before turbine	MPa	0.459	3.09	4.40
5 Pressure ratio of expansion	-	4.5	2.20	3.00
6 Isentropic efficiency of turbine	%	88	90	90
7 Cooling coefficient	%	1	1	1
8 Temperature before compressor	°C	30	50	50
9 Isentropic efficiency of compressors	%	84/83	86/85	86/85
10 Difference of temperatures in heat exchanger	°C	40	22	30
11 Sum of relative loss of pressure	%	9.0	10.3	12.0
12 Cycle efficiency	%	34.1	37.1	38.3
13 Flow stream through turbine	kg/s	1.94	36.1	172.0
14 Mean heat stream in absorber	kW/m ²	40.7	151.0	82.0

As is to be seen in Figs. 1 and 2, the essential elements in the cycle of the heliothermal power plant are constituted, in contradiction to the classical cycle of the gas turbine, by the solar absorber (e), the heat storage battery (f) and the set of valves (o), (p), (r).

Table 1 shows, on the other hand, that it is distinctly worthwhile to use open cycle only in low power generating stations. The use of helium instead of air in a closed cycle reduces considerably the flow stream and the pressure before the turbine and simultaneously increases the load of the absorber, bringing about much smaller overall dimensions of the elements composing the power station of equal power.

As has already been said, the «heart» of a solar power station is constituted by the solar absorber, Fig. 3. From the proper functioning of this device depends in the main ex-

tent the correct operation of the power station and its overall efficiency $\eta_{el} = \eta_{ey} \cdot \eta_{abs}$

The absorber must have high efficiency, small heating surface and low weight. Establishing the output data resulting from the calculation of the cycle, such as the quantity of the heat stream to be transmitted to the working medium, the construction of an absorber is formed as a result stream along tube 1, 2/ relation of the spacing of tubes to the diameter t/d , 3/ tube diameter d , 4/ pressure p of the working medium, 5/ permissible relative pressure loss $\Delta p/p$, 6/ maximal temperature in tube walls t , 7/ permissible load in tubes, produced by internal of an absorber, as well as of other equipment being part of a heliothermal power station, develops as a result of the realization of analytical programs on computers.

The regulation of parameters and power station protection constitute an important problem. Regulation of the power produced is most frequently carried out by change of pressure in the circuit (different revolutions of compressors) at the same inlet temperature into the turbine. This does not create any distinct decrease in efficiency at partial loads in proportion to the power rating. Sudden changes of load are regulated by means of the by-pass valve («by») connecting the outlet channels of the compressor (b) of the heat exchanger (g) and of the absorber (e) with the turbine outlet. This valve constitutes now and then an equivalent element of regulation beside the normal change of pressure in the circuit at partial loads. The valves (l) and (m) protect the compressors from pumping during starting or stoppage of the power station. In extraordinary cases, e.g., when the danger arises of turbine overspeeding caused by excess of revolution by 10 p.c., defects in the oil circulating and the bearing systems, when excessive vibrations of the gyrating system appear the cutoff valve (n) should be completely opened. A rapid discharge of the system then takes place and the turbine set stops within a few seconds.

Various working media flowing through the absorber may be used: air, water-steam and even liquid sodium. The last one is foreseen for the design by General Electric of a heliothermal power plant, sodium being a better heat absorber than water, constituting also a good heat storage medium.

Literature

1. Brinkworth J., Brian J.: Energia słoneczna w człowieka (Solar Energy in the Service of Man). PWN Warsaw 1979.
2. Elektrownie słoneczne. Ciekły sod jako medium robocze dla elektrowni słonecznej o mocy 100 MW. Nowa technika w energetyce zagranicznej. (Solar Power Plants. Liquid Sodium as Working Medium for Solar Power Plant of a Power of 100 MW. (New Technology in Foreign Power Engineering). Biuletyn Techn. I. En. 188/1979.

3. Bammert K. Layout of Gas Cycles for Solar Power Generation, ISPRA-Course Italy 3-7 Sept. 1979.

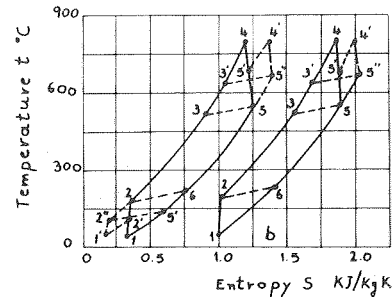


Fig. 1

Fig. 1 Cycle of a Heliothermal Power Plant on a t-s Diagram in a Closed /a/ and an Open /b/ System

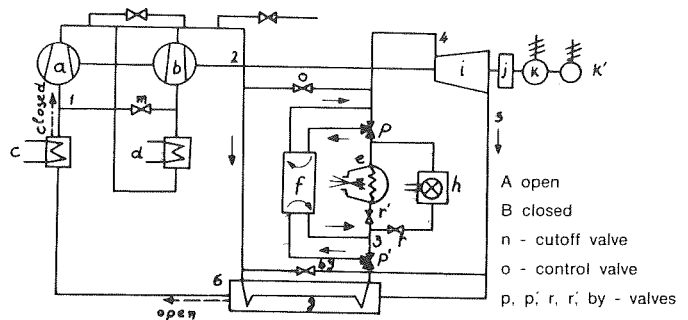


Fig. 2

Fig. 2. Block Diagram of the Cycle of a Heliothermal Power Plant /Open and Closed/ together with a Regulation and a Protection System a - 1st stage compressor, b - 2nd stage compressor, c, d - cooler, e - absorber, f - heat storage battery, h - combustion chamber, i - turbine, j - transmission, k - generator, k - starting motor, l, m - compressor by-pass valves

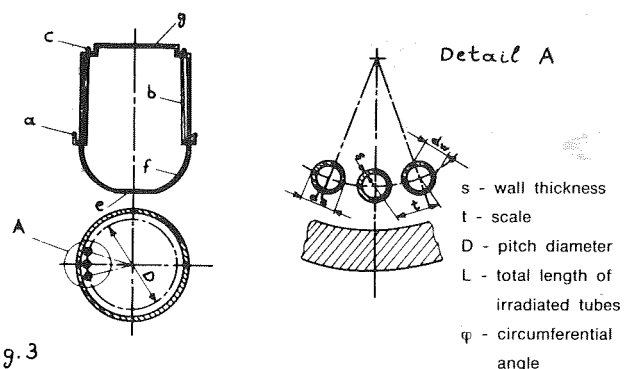


Fig. 3

a - inlet chamber, b - tubes, c - outlet chamber, d - tube diameter, e - hole, f - reflecting part of absorber, g - ceiling, l - length of tubes

Fig. 3 Absorber

H.T.I. CALENDAR OF EVENTS

Academic Year 1980-81

By Ms D. Charalambidou,
Lecturer, H.T.I.

September

The academic year 1980-81 was launched on September 8th. Four hundred and sixty-two (462) students were enrolled including sixteen (16) foreign students. The Electrical Part-time Course continues with seventeen (17) students on its fourth year running.

The Polyvalent course for Medical Technicians which is sponsored by the World Health Organization (W.H.O.) has twelve (12) foreign students from various Middle East countries and two (2) Cypriots.

The World Health Organization decided in co-operation with HTI to set-up two more short courses: The X-ray specialised course to begin in January with eight foreign students and three local ones and the Operating Theatre Course with eight foreign students to start in May.

The Director of HTI Mr G. Cristodoulides leaves for Belgrade to attend the 21st General Conference of Unesco.

October.

The third-year Marine officers return after a four-month training on board.

The Astronomy club organises its first lecture. Mr A. Achillides talks on «Contactees, the UFO Cult» at the H.T.I. Lecture Theatre.

The Lecturers' League announces a «get together» drink at the Sindbad Pub.

The film Committee shows a series of films on the History of the Motor-car at the H.T.I. Lecture Theatre.

A visiting professor from the Federal Republic of Germany, Dr Born, who is a specialist on Lasers, gave a Lecture on lasers at the H.T.I. Lecture Theatre. He was introduced by the Ag. Director General of the Ministry of Labour and Social Insurance Mr. Kallimachos.

The lecture was organised in co-operation with the Goethe Institute.

Miss Eleni Mavrou was elected President of the Students Union. She is the first female president of the Union.

November

This year UNESCO DAY was celebrated on 10th November at Khirokitia.

Students and staff left the H.T.I. premises early in the morning and arrived in Khirokitia about 10 a.m. There Mr M. Louloupis, Officer of the Department of Antiquities, briefed the students and staff on the historic background of the Khirokitia settlement. After Mr Louloupis talk some of the students and staff made their way through the pre-historic ruins of the bee-hive houses which are dated back to the sixth millenium B.C. to the hill from which one can have a very good view of the peaceful valley below. The pebbled ruins which served in the past as dwellings as well as burial places - the dead were buried in their floor with gifts in a contracted position — lay there gaping empty in the sun.

The students placed a litter basket at the entrance of the Khirokitia settlement.

The whole group left about 11.30a.m. and headed towards Governor's Beach for lunch.

There they scattered around making their arrangements for lunch. Eating and drinking accompanied with song and dance took up the whole afternoon.

At dusk the row of buses set off for Nicosia at a lazy pace.

The last week of November was Safety Week for H.T.I.. The safety Committee organised various activities including a lecture and film on Fire-Fighting, a lecture on Factory law and Regulations and a film on Safety.

DECEMBER

On second December there was a lecture at H.T.I. Lecture Theatre on «Technical Education in the Soviet Union» delivered by Dr. Vasilis Efremovich Anomarienko.

The «H.T.I. Bridge Club» makes its first appearance on December 5th. Its aim is to teach anyone interested to play bridge.

Cristmas time draws nearer. The H.T.I. joins in the festivities: the students held their annual Christmas Dance at Isadoras Night clup; On 17th December a joint Staff-Student party was held in the canteen of the Institute. Classes were suspended at 11.30 a.m. and students and staff had a drink together with some snacks.

The Association of the H.T.I. Graduates held their annual Christmas Dinner at the Philoxenia Hotel on December 20th.

JANUARY

The Astronomy Club and C.I.C.A.P. organised a Lecture at the H.T.I. Lecture Theatre. Mr A. Achillides talked on the exploration of outer space with unmanned space ships.

H.E the Minister of Labour and Social Insurance, Mr G. Stavrinakis, visited the H.T.I. on January 20th to award the shields, cups and medals to the participants and winners of the H.T.I. Volley, Basket and Football tournaments.

Afterwards the Minister inaugurated the H.T.I. Self-Study Center which was set up with the aid of the British Council. The British Council Representative, *Mr Marler* donated a number of programmes and publications.

Dr A. Mallouppas leaves on 10th January for Luton while Mr, Derek Curran is sent to Cyprus on a staff exchange visit. The second half of January is a hectic time because of the first semester exams.

FEBRUARY

The first semester exams are over. Lectures, seminars and tutorial are resumed again.

The H.T.I. Film Society gives a cocktail for all H.T.I. foreign Students at the P.I.O. premises and shows them two films on Cyprus: «The Island that No one Ever Forgets» and «Cyprus wedding». The Director honors the cocktail with his presence and has an opportunity to mingle with and chatters to the H.T.I. foreign students.

MARCH

On the 19th March the students decided to go on a strike demanding some rights.

The strike ended on May 4th.

APRIL

April found the students abstainig from classes.

Dr. D. H. W. Hykin and Dr. J. A. Douek from the Polytechnic of South Bank gave two Lectures on the concept of workshop on Tuesday 14th April.

MAY

The students ended their strike on May 3rd.

Students and staff decided to do their utmost to make up for lost time due to the students strike.

JUNE

Professor D. R. Wilson, Head of Engineering of the Polytechnic of Central London, gave a lecture at the H.T.I. Lecture theatre on June 11th, on current UK and U.S.A. practises in Engineering Education.

Exams are postponed till 17th of June. Staff and students show symptoms of exam fever which is aggravated by hot weather.

The Graduation ceremony will be held on the 10th of July.

SKF The largest manufacturer of ball and roller bearings

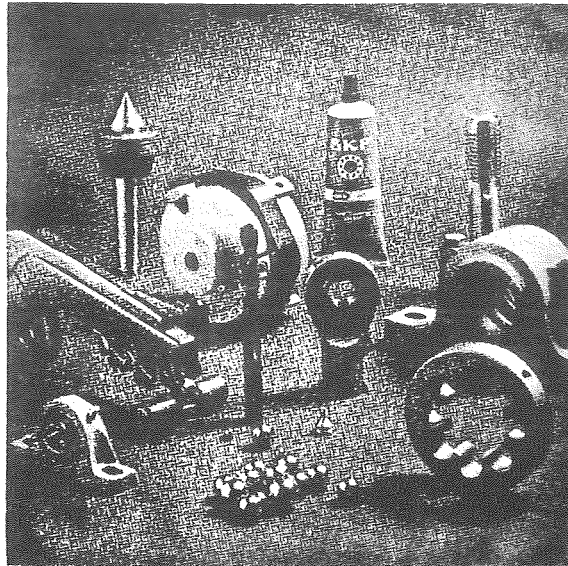
SKF is an international group with factories in twenty countries, an international sales network, and its own service organisation spread around the world.

SKF bearings are made in 8,000 basic types and sizes and many thousands of variants ranging from 3mm to several metres in outside diameter and from a weight of 0.036 grammes to more than 6,000 Kg. There are SKF bearings which can run at a speed of 400,000 r.p.m. and others which at low speed can carry loads of more than 2,000 tons.

SKF research efforts stretch from theory right through applied mathematics by computer to manufacturing process and product development. To illustrate the degree of accuracy required we may cite the example of any one medium sized bearing where ball diameters must not deviate more than 0.00002in., and where errors in sphericity in one particular ball must not exceed 0.00001in.

MUCH MORE THAN BEARINGS

BALL BEARINGS
ROLLER BEARINGS
CASTINGS
MACHINE TOOLS
TOOLS



TEXTILE MACHINERY
COMPONENTS
PLANETARY ROLLER
SCREWS
FLUIDICS

SKF

SKF Best possible service to customers

Research and development in the SKF group is applied in three directions. The first is the development of production technology the second is the development of new products and the third is a continuous process of developing the traditional product ranges to changing market requirements.

SKF faces strong competition in all the most important industrial countries. It is, however, true to say that SKF is foremost in the field of roller bearing engineering, in addition to being the most important exporter of ball and roller bearings.

SKF has attained this pre-eminent position for several reasons. One of them being that SKF was the first bearing firm to undertake systematic theoretical and experimental research in ball and roller bearing engineering.

SOLE AGENTS:

SWEDISH LEVANT TRADING (CYPRUS) LTD.

P. O. Box 1252 — Tel. 43833 — NICOSIA - CYPRUS

ΠΡΩΤΟ

Το SENIOR SERVICE EXTRA MILD πρώτο στο είδος του τσιγάρου στην Κύπρο και επίτευγμα της μεγαλύτερης εταιρίας καπνικών προϊόντων στον κόσμο, είναι πια καθιερωμένο ως το ελαφρότερο τσιγάρο με τις μεγαλύτερες πωλήσεις.

Και ιδού γιατί:

- Πρωτοπόρησε στο ΔΙΠΛΟ ΦΙΛΤΡΟ, που υπήρξε το αποτέλεσμα έντακτης έρευνας και τέλειας, σύγχρονης τεχνολογίας.
- Προσφέρει γνήσιο χαρμάνι από εξαιρετικής ποιότητας καπνά Βιρτζίνια.
- Ο συνδυασμός αυτός φίλτρου και καπνού δημιουργεί την απόλυτη ισορροπία που ζητεί ο καπνιστής μεταξύ απολαυστικού και ελαφρού καπνίσματος.
- Κι ακόμη τα SENIOR SERVICE EXTRA MILD έχουν την πιο μοντέρνα και νεανική συσκευασία σε χρώματα και σχήματα.

SENIOR SERVICE

EXTRA MILD

*το ελαφρότερο τσιγάρο
με τις μεγαλύτερες πωλήσεις*

